Magnetic skyrmions and spin spirals in ultrathin films and canted magnetic fields

Dissertation with the aim of achieving a doctoral degree
at the Faculty of Mathematics, Informatics and
Natural Sciences Department of Physics

of Universität Hamburg

submitted by
Dipl.-Phys. Lorenz Schmidt
Hamburg, 2017

Gutachter der Dissertation:

Herr Prof. Dr. R. Wiesendanger
Herr PD Dr. G. Meier

Gutachter der Disputation:

Frau Prof. Dr. D. Pfannkuche
Herr Prof. Dr. U. Merkt
Herr Prof. Dr. M. A. Rübhausen

Datum der Disputation:

14.07.2017

Vorsitzender des Promotionsausschusses:

Herr Prof. Dr. W. Hansen

Dekan der MIN-Fakultät:

Herr Prof. Dr. H. Graener

Zusammenfassung

Das Zusammenspiel von Austausch- und Dzyaloshinskii-Moriya-Wechselwirkung, sowie magnetischer Anisotropie und externer magnetischer Felder, führt zu verschiedenen nicht-kollinearen magnetischen Zuständen wie Spinspiralen, chiralen 360°-Domänenwänden und Skyrmionen. Außer durch akademisches Interesse, wird die Forschung an 360°-Domänenwänden und Skyrmionen durch mögliche Anwendungen in der Spintronik angetrieben. Um maßgeschneiderte Systeme herstellen zu können, ist es notwendig zu verstehen, wie die chemische Zusammensetzung sowie die Nanostruktur den Magnetismus bestimmen. Daher untersuche ich mit einem Rastertunnelmikroskop (RTM) nicht-kollineare magnetische Strukturen bei tiefen Temperaturen in ultradünnen Filmen, welche aus wenigen atomaren Lagen von Eisen, Palladium und Waserstoff auf Ir(111) Einkristallen bestehen. Im Gegensatz zu vorherigen Untersuchungen mit RTM nutze ich ein magnetisches Vektorfeld, das die vollständige Abbildung der magnetischen Struktur erlaubt. Damit ist auch der Magnetisierungsdrehsinn bestimmt, der von der Ausrichtung des Dzyaloshinskii-Moriya-Vektors abhängt.
Ich bestimme den Magnetisierungsdrehsinn im rekonstruierten Teil der zweiten Eisenlage, in der Einzellinienstruktur der dritten Eisenlage und in der Palladium-Eisen Bilage durch die Verwendung von geneigten Magnetfeldern. Dazu nutze ich bekannte Vorgehensweisen, wie spinpolarisierte RTM mit Feld-unabhängigen und -abhängigen Spitzen, aber auch RTM mit Hilfe eines neuen magnetoresistiven Effekts, dem nicht-kollinearen Magnetowiderstand.
Für den anisotropen Magnetismus der Einzellinienstruktur in der dritten Eisenlage stelle ich ein isotropes, mikromagnetisches Modell als Näherung vor. Aus der Form der 360° Domänenwände in Feldern senkrecht zur Probenebene und der Abschätzung einer Sättigungsmagnetisierung ergibt sich ein voller Satz mikromagnetischer Werte.
In der Palladium-Eisen Bilage zeige ich wie die Ausbreitungsrichtung der Spinspirale im Grundzustand an den Filmrand gekoppelt ist. Eine Neuausrichtung der Ausbreitungsrichtung ist möglich durch in der Probenebene liegende magnetische Felder, die bereits beim Einkühlen der Probe anlagen.
Zuletzt stelle ich die Ergebnisse der Bedampfung der zweiten bis zur fünften Eisenlage mit Palladium vor. Dabei entsteht eine durch Wasserstoff verursachte Struktur in der zweiten Eisenlage. Die vierte und fünfte Eisenlage sowie das Palladium darauf verhalten sich ferromagnetisch. Sowohl Wasserstoff als auch Palladium erhöhen die Periodenlängen der Spinspiralen in der dritten Eisenlage. Wasserstoff führt in der zweiten Eisenlage zu einer isotropen Struktur, deren magnetischer Grundzustand eine Spinspirale ist und durch magnetische Felder senkrecht zur Probe in Skyrmionen übergeht.

Abstract

The competition of exchange interaction, Dzyaloshinskii-Moriya interaction (DMI), magnetic anisotropy and external magnetic fields leads to the emergence of non-collinear magnetic structures like spin spirals, chiral 360°-domain walls and skyrmions. Besides scientific interest, the possible applications in spintronics motivate the research on domain walls and skyrmions. In order to tailor systems for application it is necessary to understand how the properties of such systems depend on their chemical composition and nanostructure. Therefore, I investigate different ultra-thin films consisting of few atomic layers of iron, palladium and hydrogen on Ir(111) single crystals that exhibit non-collinear magnetic structures at low temperatures via scanning tunneling microscopy (STM) and spin-polarized scanning tunneling microscopy (SP-STM). Contrary to previous STM investigations, the use of a magnetic vector field makes it possible to resolve the complete three-dimensional magnetic structure. This reveals the sense of magnetization rotation, which is determined by the orientation of the DM vector.
I determine the sense of magnetization rotation in the reconstructed areas of the second atomic layer of iron, in the single line areas of the third layer of iron and in the palladium-iron bilayer by application of canted fields. For this purpose, I employ well-known methods like SP-STM with field-dependent and field-independent STM tips but also non-spin-polarized STM involving a novel magnetoresistive effect, non-collinear magnetoresistance (NCMR).
In case of the single line areas in the third layer of iron, I propose an isotropic micromagnetic model as an approximation for the observed anisotropic magnetism. Fits to single 360°-domain walls in a magnetic out-of-plane field yield a full set of micromagnetic parameters after estimating the saturation magnetization.
For the palladium-iron bilayer, the influence of the film's edge on the propagation direction of the spin spiral is investigated. Moreover, the propagation direction can be reoriented by field-cooling in magnetic in-plane fields.
In addition, I deposited palladium on iron between the second and the fifth layer on Ir(111). A hydrogen superstructure was observed for the second iron layer. The fourth and fifth layer of iron with palladium islands on top behave like ferromagnets. Both hydrogen and palladium lead to an increase of the spin spiral period in the third atomic layer of iron. Hydrogen forms an isotropic superstructure in the second iron layer, which exhibits spin spirals as a ground state and skyrmions in magnetic out-of-plane fields.

Contents

List of Figures

Acronyms

DMI Dzyaloshinskii-Moriya interaction

STM scanning tunneling microscopy

SP-STM spin-polarized scanning tunneling microscopy

MBE molecular beam epitaxy

ML monolayer

DL double layer

TL triple layer

FM ferromagnetism or ferromagnetic

DOS density of states

LDOS local density of states

TMR tunneling magnetoresistance

UHV ultra-high vacuum

FFT fast Fourier transformation

LEED low energy electron diffraction

AES Auger electron spectroscopy

NEG non-evaporable getter

SOC spin-orbit coupling

NCMR non-collinear magnetoresistance

TAMR tunneling anisotropic magnetoresistance

Chapter 1

1 Introduction

The first recorded phenomenon of magnetism was the orientation of a magnetic object in a magnetic field known since ancient times. Its first documented application as a compass made from naturally magnetized magnetite for orientation dates back to the Han dynasty between 200 to 300 B. C. [1]. With the beginning of the renaissance in Europe the knowledge of magnetism and its phenomena increased continuously culminating in the formulation of the well-known Maxwell equations that describe the relation of electric and magnetic fields to electrical charges. In combination with the Lorentz force, which deflects charged particles that move in a magnetic field, this led to the understanding of almost all magnetic phenomena known at that time. In the 19th century the application of magnetism gained significance starting with the use of electromagnets in telegraphs, which enabled communication with unprecedented speed. However, it was still not understood how an object could be magnetic at room temperature without any external currents involved. An explanation followed in the 1920s with quantum mechanics and the discovery of the spin that is the intrinsic orbital momentum of every elementary particle. The spin and the movement of the charged particle determine its magnetic moment. The magnetic moment of atoms is dominated by the electrons. In some materials the spins of the electrons do not orient arbitrarily but point collectively in the same direction leading to a net magnetic moment. Since then, the understanding of magnetism and spin structures has increased rapidly resulting in a wide field of applications ranging from mundane permanent magnets on the fridge door to magnetic resonance tomography used for medical diagnosis. One of those applications is magnetic data storage for non-volatile mass data storage in information technology. Most common is the hard disk which stores data in form of ferromagnetic domains that correspond to large groups of parallel pointing magnetic moments. Serial arrangements of differently oriented domains are used in combination with a mechanically moving read-and-write head to store binary data. While there is still room to increase its storage capacity with new technologies like heat- or microwave-assisted magnetic recording, its intrinsic drawbacks which are high access latency, serial data processing and limits to miniaturization due to moving mechanical parts have not been solved until today. Instead, several new schemes for data storage were proposed that lack mechanically moving parts – among them is the racetrack memory [2–4]. Racetrack memory uses a stationary read-and-write head that lies on top of a stripe of magnetic material. The previously immobile domains are pushed through the magnetic stripes via electrical current. However, the necessary current densities of $10^{12}\,\mathrm{A/m^2}$ [4] are too large for use in today's electronics. A novel non-collinear spin structure – skyrmions – were suggested to substitute the domains and thus reduce the necessary current densities [5].

Magnetic skyrmions are localized and stable whirls of magnetic moments with particle-like characteristics. They exist surrounded by collinear oriented spins either in a lattice phase or as single meta-stable skyrmions within a ferromagnetic surrounding [6–8]. Skyrmions were predicted to emerge in magnetic systems that exhibit Dzyaloshinskii-Moriya interaction (DMI) [9, 10]. The DMI prefers a perpendicular orientation of neighboring spins with a unique sense of magnetization rotation and thus prevents the skyrmions from unwinding into a collinear structure. However, DMI occurs only in materials that lack inversion symmetry which means that skyrmions can only exist in few systems. These are made either of an intrinsically non-centrosymmetric material like B20-compounds [11, 12] or lack the inversion symmetry due to an interface between different materials [13, 14].

Skyrmions correspond to inversion of magnetization in a continuous medium. Therefore they can be used for the storage of binary data in the same way as domains [15]. They are proposed for application in the racetrack memory because their threshold current density for moving was found to be smaller by about five orders of magnitude than for domains [16]. Since then, the concept of a skyrmion-based racetrack memory has been developed in more detail [17, 18] and even further possible applications in spintronics like logic [19] or microwave devices [20, 21] were proposed. Moreover, the experimental realization of a skyrmionic system that is viable for application has made significant progress. It was proven that skyrmions can be deleted and written by currents [22] and electric fields [23]. Systems that exhibit skyrmions at room temperature were found [24–26] and even movement speeds in the range of 100 m/s were reported [25]. However, a system that fulfills all requirements for application remains unknown.

Despite the shift of the community's focus towards skyrmionic systems at room temperature there are still fundamental properties than can be investigated at low temperatures with spin-polarized scanning tunneling microscopy (SP-STM) [27]. The investigation of system property changes due to the use of other materials or more layers in ultra-thin films can offer insights that help to tailor systems for application. It would be intriguing to find a layer-dependent reversal or otherwise large change of DMI as it plays a key role not only for the size [28–30] but also for the movement of skyrmions within confined structures like stripes [17, 18, 29, 31].

In this thesis I investigate several effectively two-dimensional magnetic systems that exhibit spin spirals and skyrmions in canted and in-plane magnetic fields via scanning tunneling microscopy (STM) and SP-STM. In contrast to three-dimensional bulk systems the interfacial magnetic anisotropy in ultra-thin films can lead to a strongly preferred magnetization orientation relative to the crystal. As a consequence, the magnetic structures distort rather than reorient in external magnetic fields. Hence, ultra-thin films allow me to investigate distortions of spin spirals and skyrmions by canted magnetic fields. The distortions yield the orientation of the DMI vector via the sense of magnetization rotation and spin spiral or skyrmion shape. SP-STM can also probe the sense of magnetization rotation in systems with a negligible distortion in magnetic fields by resolving the various components of the magnetization directly [32, 33]. The sense of magnetization rotation can also be probed with other experimental techniques like Kerr microscopy [34], spin-polarized low-energy electron microscopy

[35] and Lorentz transmission electron microscopy [36]. However, these other techniques are usually used for studies on structures of considerable larger size. In my experiments I grew ultra-thin films of magnetic metals of iron (Fe) and palladium (Pd) on the heavy metal substrate iridium (Ir) via molecular beam epitaxy (MBE). Then, I investigated the magnetic structure that results from deposition of palladium and hydrogen by MBE on different layers of iron on iridium. This revealed a spin spiral and skyrmion phase in the hydrogenated double layer (DL) of iron. My interest in these experiments lies in finding skyrmionic systems in thicker magnetic films which were shown to exhibit magnetic long-range order at elevated temperatures [37–39]. As a consequence, these thicker films might exhibit skyrmions at higher temperatures than the corresponding thinner films. Understanding how film thickness influences skyrmionic systems will help to develop systems that exhibit skyrmions at room-temperature.

1.1 Thesis overview

Chapter 2 presents a brief overview of all necessary fundamental knowledge concerning magnetism in ultra-thin films and the resulting non-collinear magnetic structures. In this chapter I also discuss the working principle of SP-STM including the *modus operandi* in this thesis. This is followed by an introduction to the used low-temperature STM within a three-axis superconducting magnet and its setup in **Chapter 3**. Then, I explain how I prepared STM tips and samples for my studies. For the purpose of brevity only the non-standard parts and procedures will be listed and explained in detail. Since science is an inherently iterative process I use **Chapter 4** to discuss the previous studies concerning the double and triple atomic layer of iron as well as the bilayer of palladium and iron (Pd/Fe) on an Ir(111) single crystal. Moreover, I introduce a magnetoresistive effect that has so far only been documented for the Pd/Fe bilayer system. The descriptions and results of my experiments are covered in **Chapter 5**. Beginning with the iron double and triple layer I determine their sense of magnetization rotation via application of several differently oriented magnetic fields by SP-STM. For the iron triple layer (TL) I present a model for the magnetization and extract the corresponding parameters derived from fits to 360° domain walls. This follows a study of the Pd/Fe bilayer's response to magnetic in-plane and canted fields, which is broader in scope. Within this study I demonstrate the reorientation of the spin spiral propagation direction by magnetic in-plane fields. I determine the cycloidal nature of the spin structures and the sense of magnetization rotation via STM. In a new study, I show the resulting magnetic structures from a palladium and hydrogen deposition by MBE on the second to the fifth layer of iron on Ir(111). Thereby, the focus lies on the Fe-DL as it exhibits spin spirals and skyrmions in restructured areas. Finally, I present evidence that these restructured areas are not related to palladium. In **Chapter 6** I summarize my findings and mention possible future studies based on the outcome of this thesis.

Chapter 2

2 Fundamentals

This chapter covers the fundamentals concerning magnetism in ultra-thin films and some of their resulting non-collinear structures. Then I present the principle of STM, SP-STM and their mode of operation in this thesis.

2.1 Magnetism in ultra-thin films

2.1.1 Zeeman energy

The Zeeman energy is the potential energy of all magnetic moments $\mathbf{m}_i$ in an external field $\mathbf{B}$:

$$\mathrm{H_{Ze}} = -\sum_i \mathbf{B}\mathbf{m}_i$$

Thus, the energy states depend on their alignment with the external field resulting in an energetic preference of the magnetic moments to orient parallel to the external field. A consequence of the Zeeman energy and the magnetic field produced by the magnetic moment is the dipolar coupling between magnetic moments, which means that a magnetic moment orients in the field of the surrounding magnetic moments and *vice versa*.

2.1.2 Direct exchange

Magnetic long-range order at temperatures above few Kelvin is stabilized by exchange interaction. The latter describes how the magnetism of many-body systems is intimately coupled to its charge distribution. Exchange interaction is a consequence of the Pauli exclusion principle and the competition between kinetic and Coulomb energy of electrons in a many-body system [40]. In the simplest case of interatomic exchange, which considers two atoms that each contain one electron at all times, the Pauli exclusion principle forces the total wave function of the electrons to be antisymmetric. This means that either their spatial distribution is symmetric and their spin state must be antisymmetric or *vice versa*. Hence, for a parallel orientation of both electrons' spins their Coulomb energy is reduced due to different spatial probability density distributions. On the other hand, for an antiparallel orientation of the spins the electrons can share the same space resulting in a reduction of their kinetic energy. The

outcome of this interplay depends on the electronic configuration of the involved atoms and determines whether the spins prefer to orient parallel or antiparallel. Phenomenologically, the direct exchange can be expressed as the following spin-spin coupling:

$$\mathrm{H}_{\mathrm{ex}} = \sum_{ij} J_{ij} S_i S_j$$

where S_i (S_j) is the spin of atom i (j) and J_{ij} the exchange integral, which will prefer an antiparallel (parallel) orientation for $J_{ij} > 0$ ($J_{ij} < 0$). Since the exchange integrals between neighbors of different distances can vary, the spins exhibit frustration and hence the resulting spin texture is in general a spin spiral. Moreover, direct exchange coupling is symmetric and isotropic as the energy of the system depends only on the angles between the spins but not on their absolute orientation. The direct exchange is only the lowest-order term within the Hubbard model for a crystal. Higher-order terms like biquadratic exchange can play a role in some systems.
In solid state physics the classical Heisenberg model is usually employed, which uses real vectors of constant length instead of spin operators. Additionally, the interaction between neighboring atoms is assumed to be identical and thus a single value for $J_{ij} = J$ is sufficient. The discreteness of the atomic lattice can be ignored and a continuum model used, if the angles between the magnetic moments of neighboring atoms are small. This results in the following energy contribution:

$$E_{\mathrm{ex}} = A \int_V \left(\boldsymbol{\nabla} \boldsymbol{m}(\boldsymbol{r})\right)^2 \mathrm{d}V$$

where A is the exchange stiffness and $\boldsymbol{m}(\boldsymbol{r})$ the reduced magnetic moment vector at position $\boldsymbol{r}$.

2.1.3 Magnetic anisotropy

Magnetic anisotropy is an overarching term for several interactions that contribute to the same phenomena. The following expression for the first-order uniaxial anisotropy energy is sufficient for isotropic, ultra-thin films on single crystals:

$$E_{\mathrm{ani}} = \sum_i K_{\mathrm{eff}} \sin^2 \phi_i$$

where K_{eff} is the effective anisotropy coefficient and ϕ_i the angle of the ith magnetic moment with the surface normal. For $K_{\mathrm{eff}} > 0$ ($K_{\mathrm{eff}} < 0$) the axis is called easy (hard) axis since the magnetic moments will prefer to orient collinear (perpendicular) to it in order to reduce the anisotropy energy. In infinite thin films and in the absence of stress the effective anisotropy coefficient K_{eff} can be described by three terms [41, 42]:

$$K_{\mathrm{eff}} = K_{\mathrm{d}} + K_{\mathrm{V}} + \frac{K_{\mathrm{s}}}{t}$$

with the thickness t of the magnetic film. The first term is the shape anisotropy K_d which results from the Zeeman energy of the magnetic moments in their own magnetic field. It corresponds to the demagnetization energy in infinite films where surface charges can be neglected. The shape anisotropy prefers an in-plane orientation of the magnetic moments. Volume magnetocrystalline anisotropy K_V results from the interplay between the electron currents in a single ion and the electromagnetic field supplied by the surrounding ions,i. e. the crystal-field. The electric currents within the single ion are determined by the spin-orbit coupling. Electrons in 3d-orbitals have a high probability density further away from the nucleus than the other atom's electrons resulting in a strong interaction with the crystal-field. For this reason, the anisotropy of atoms with partially filled 3d-orbitals is dominated by the crystal's symmetry. In contrast, electrons in the 4f-orbital have a high probability density close to the nucleus. These electrons are shielded from the crystal field by the other atom's electrons. As a consequence, the anisotropy of atoms with a partially filled 4f-orbital is determined by the charge distribution within the atom. Typical anisotropy energy densities are 0.05 MJ/m^3 (0.5 MJ/m^3) for bcc Fe (hcp Co) which are governed by 3d-orbital electrons. Rare earth magnets that are dominated by 4f electrons reach values of about 10 MJ/m^3 [43]. The last term is the surface and interface anisotropy K_s that results from the change in magnetocrystalline anisotropy at the surface or interfaces. The surface atoms lack neighboring crystal atoms on one side which leads to the change in magnetocrystalline anisotropy. In the same way, the atoms at interfaces experience different neighbors resulting in a modified magnetocrystalline anisotropy. Additionally, magnetoelastic effects at interfaces due to the lattice mismatch between the different materials can have an impact on the interface anisotropy. Consequently, the influence of the surface and interface anisotropy decreases with the thickness t of the magnetic film.
For a representation in the continuum model the following expression with the anisotropy energy density K and the angle of the magnetic moment $\phi(\boldsymbol{r})$ at position $\boldsymbol{r}$ can be used:

$$E_\mathrm{ani} = \int_V K \sin^2 \phi(\boldsymbol{r})$$

2.1.4 Antisymmetric exchange

The antisymmetric part of the exchange interaction between neighboring magnetic moments is also called DMI. It was first phenomenologically described by Dzyaloshinskii [9] and later the driving mechanism, which is spin-orbit coupling, was identified by Moriya [10]. DMI can be phenomenologically described by the following Hamiltonian:

$$\mathrm{H}_\mathrm{DMI} = -\sum_{i,j} \boldsymbol{D}_{ij} \left(\mathbf{M}_i \times \mathbf{M}_j \right)$$

with the sum over all magnetic moments $\mathbf{M}_i$ and $\mathbf{M}_j$ of a discrete system and the DMI vector $\boldsymbol{D}_{ij}$. The coupling of the magnetic moments with a vector product explains why it is called antisymmetric

exchange and makes a canting of neighboring magnetic moments by $\frac{\pi}{2}$ energetically favorable. The DMI will vanish if the system is centrosymmetric, since the Hamiltonian has to be invariant under all symmetry operations of the system. In the same way the orientation of $\boldsymbol{D}_{ij}$ is governed by the symmetry of the system [7, 44]. Furthermore, DMI is anisotropic as not only the relative angle between neighboring moments but also their orientation relative to $\boldsymbol{D}_{ij}$ and thus their absolute orientation in space makes a difference in energy. An expression for the continuum model with the DMI energy density vector $\boldsymbol{D}$ and the reduced magnetic moment vector $\boldsymbol{m}(\boldsymbol{r})$ at position $\boldsymbol{r}$ is:

$$E_{\mathrm{DMI}} = \boldsymbol{D} \int_V \boldsymbol{m}(\boldsymbol{r}) \left(\nabla \times \boldsymbol{m}(\boldsymbol{r}) \right) \mathrm{d}V$$

While B20 compounds [11] can exhibit DMI due to their intrinsically non-centrosymmetric structure, it is also possible to engineer non-centrosymmetric systems via defects [45] or by placing non-magnetic atoms with large spin-orbit coupling next to magnetic atoms. The latter has been realized via heavy impurity atoms in spin glasses [13, 46] and by interfaces between ultra-thin magnetic films and heavy atom layers providing strong spin-orbit coupling [32, 41, 47]. In these kind of systems the DMI is explained by considering two magnetic atoms and their indirect interaction mediated by the spin-orbit coupling from a third non-magnetic atom.

2.2 Non-collinear magnetic structures

2.2.1 Spin spirals

The general ground state of the classical Heisenberg model is a non-collinear state – a homogeneous spin spiral. Collinear states like FM order are only special cases of spin spirals. For a discrete lattice of spins $\mathbf{S}_i$ the general solution can be described with the spin magnitude S, two spatial unit vectors $\hat{\boldsymbol{a}}, \hat{\boldsymbol{b}}$, a wavevector $\boldsymbol{k}_{\mathrm{SS}}$ and the position $\boldsymbol{r}_i$ as follows:

$$\mathbf{S}_i = S \left(\hat{\boldsymbol{a}} \cos\left(\boldsymbol{k}_{\mathrm{SS}} \boldsymbol{r}_i \right) - \hat{\boldsymbol{b}} \sin\left(\boldsymbol{k}_{\mathrm{SS}} \boldsymbol{r}_i \right) \right)$$

While the period is determined by the exchange integral J through $\boldsymbol{k}_{\mathrm{SS}}$, the rotation of the spins relative to $\boldsymbol{k}_{\mathrm{SS}}$ is degenerate as the only constriction for the spatial unit vectors is $\hat{\boldsymbol{a}}\hat{\boldsymbol{b}} = 0$. This means that the spins only have to rotate within a plane which can lead to a helical (spin plane is orthogonal to $\boldsymbol{k}_{\mathrm{SS}}$) or cycloidal ($\boldsymbol{k}_{\mathrm{SS}}$ is within spin plane) spiral, see figures 2.1 a and b. Moreover, the sense of magnetization rotation is not fixed. An anisotropic interaction like DMI, see section 2.1.4, breaks this degeneracy by preferring an orientation of the spin plane perpendicular to $\boldsymbol{D}$ and a unique sense of magnetization rotation [32, 47]. Therefore, the shape of the spin spiral reveals the orientation of $\boldsymbol{D}$. Additional anisotropic terms like an external magnetic field or magnetic anisotropy can introduce inhomogeneity in the spin spiral which complicates the mathematical treatment of spin spirals [7, 48]

and can distort the spin plane into conical shapes [49, 50], see figures 2.1 c and d. In the context of spin spirals inhomogeneity means that the nearest-neighbor angle between spins θ_{nn} is not constant anymore but periodically oscillates. The special cases of $\boldsymbol{k}_{\mathrm{SS}} = 0$ corresponds to FM order and if $\boldsymbol{k}_{\mathrm{SS}}$ equals the Bravais lattice constant an antiferromagnetic order emerges.

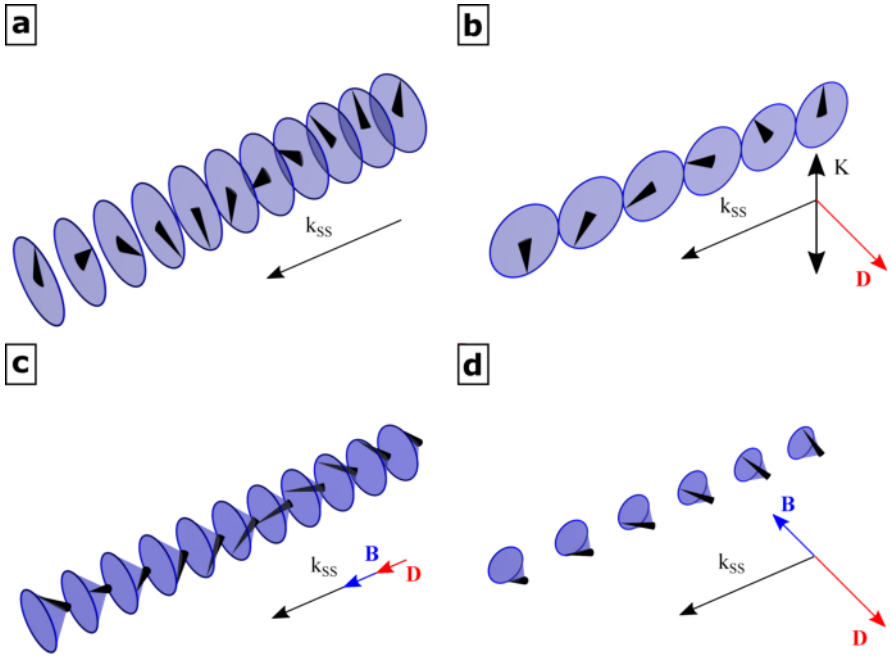

Figure 2.1: Sketch of (a,c) helical and (b,d) cycloidal spin spirals where the spin spirals in (c,d) are distorted by an external magnetic field into (c) a longitudinal conical phase and (d) a transversal conical phase. The cones correspond to spins and blue discs in (a,b) or blue cones in (c,d) symbolize the plane of spin rotation. Additionally the corresponding direction of the spin spiral wave vector $\boldsymbol{k}_{\mathrm{SS}}$, the DMI vector D, the direction of the uniaxial anisotropy K and an external field vector $\boldsymbol{B}$ are drawn. For (b) the inhomogeneity that results from the magnetic anisotropy is not taken into account, the illustration shows a homogeneous spin spiral.

As mentioned previously, the situation changes drastically if the system exhibits, in addition to Heisenberg exchange, magnetic anisotropy and DMI. Hence, I will briefly discuss the consequences for the ground state of the system for the case of $\boldsymbol{D}$ being orthogonal to $\boldsymbol{k}_{\mathrm{SS}}$ and the uniaxial axis being perpendicular to both $\boldsymbol{k}_{\mathrm{SS}}$ and $\boldsymbol{D}$ as drawn in figure 2.1 b. I focus on this case as it is the most relevant case for the thesis. Furthermore, it allows the simplification of the energy functional to one dimension [51].

$$E(\phi) = \int_{-\infty}^{\infty} \mathrm{d}x \left(A \left(\frac{\partial \phi}{\partial x} \right)^2 + D \frac{\partial \phi}{\partial x} + K \sin^2(\phi) \right)$$

Here, $\phi(x)$ is the angle of the magnetization for the lateral displacement x, A is the exchange stiffness,

D the DMI energy density and K the uniaxial anisotropy energy density. While for $K = 0$ the ground state will always be a spin spiral, for $K \neq 0$ the system will prefer a spin spiral over a FM order only if the inhomogeneity parameter κ takes a value between 0 and 1 [51]:

$$\kappa = \frac{16AK}{\pi^2 D^2} \tag{2.1}$$

For larger K a collinear orientation is energetically preferred. The additional application of a magnetic field can lead to various distortions, ranging from inhomogeneity to collective canting of the magnetic moments as illustrated in figures 2.1 c and d. Inhomogeneity means here that one orientation of the spins within the spin spiral is preferred over the others leading to an increase in period length.

2.2.2 Domain walls

Macroscopic FM systems split up into domains of different orientations to reduce their demagnetizing field energy. The interface between those domains is called a domain wall and corresponds to a localized 180° rotation of the magnetic moments in the previous model. Its shape is defined by the competition between Heisenberg exchange and uniaxial anisotropy and can be described within the previously used one-dimensional model as follows [51]:

$$\phi(x) = \arccos\left(\tanh\left(\pm\sqrt{\frac{A}{K}}x\right)\right)$$

where $\phi(-\infty) = \pi$ and $\phi(\infty) = 0$ correspond to the boundaries of the domain walls. DMI only plays a role for the domain wall energy by reducing or increasing the energy depending on the sense of magnetization rotation [51]:

$$E = 4\sqrt{AK} \pm \pi \left|D\right|$$

Therefore, a system that exhibits DMI will have domain walls with a unique sense of rotation [33, 52]. If $E < 0$ of the domain wall, the introduction of spin windings becomes energetically beneficial. This leads to the condition for a spin spiral as a ground state, see equation 2.1.
The application of an external magnetic field along the anisotropy axis lifts the degeneracy concerning the two anisotropy minima. As a consequence, one of the domain types shrinks until both domain walls meet and form a so-called 360° domain wall or twisted domain wall pair [53, 54]. An untwisted domain wall pair, i. e., two domain walls with an opposite sense of magnetization rotation can be observed but is energetically unfavorable in systems with DMI [55]. The 360° domain wall is the one-dimensional counterpart of the magnetic skyrmion which is discussed in the following section.

2.2.3 Skyrmions

In general, skyrmions refer to soliton-type solutions of non-linear partial differential equations with a spherical topology that can be associated with a topological quantum number [56]. They were first introduced to physics by Tony Skyrme in form of hypothetical particles in nuclear physics [57]. Nonetheless, this concept can be applied to other fields of physics including magnetism since the concept bases solely on topological arguments. Topology divides structures into groups that cannot be continuously deformed into each other which imposes several prerequisites to corresponding models in physics. Moreover, topology requires continuous media which means that its implications are only strictly true in magnetism within the continuum approximation. The system must inhibit discontinuous deformations which is fulfilled by the exchange interactions in magnetism. In addition, the vectors at the boundaries of the system must have a fixed orientation so that structures of different topology can be created within the system. Magnetic anisotropy leads to such a boundary condition.

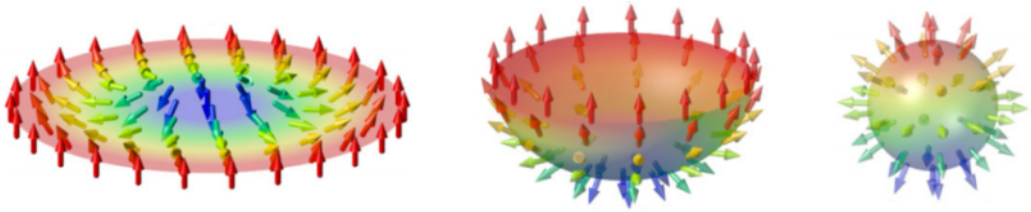

Figure 2.2: Illustration of a skyrmion in a two-dimensional system and its mapping to a two-dimensional unit sphere. The arrows correspond to unit vectors of the local magnetization and are color coded depending on their absolute orientation. Reprinted from [58], with the permission of AIP Publishing.

In magnetism skyrmions are localized whirls of magnetic moments with particle-like characteristics [8]. They can be classified by a winding number of $N \geq 1$ which corresponds to the number of times the spin sphere (see figure 2.2) can be covered [59]. The FM order corresponds to the topologically trivial state $N = 0$. I will deal only with skyrmions in two-dimensional systems as they are the only relevant species for this thesis. Their winding number can be calculated from the orientation of their magnetic moments $\boldsymbol{n}(x, y) = \frac{\boldsymbol{m}(x,y)}{|\boldsymbol{m}(x,y)|}$:

$$N = \frac{1}{4\pi} \int_A \boldsymbol{n} \left(\frac{\partial \boldsymbol{n}}{\partial x} \times \frac{\partial \boldsymbol{n}}{\partial y} \right) \mathrm{d}x\mathrm{d}y$$

Their emergence due to the competition of Heisenberg exchange, DMI and magnetic anisotropy or external magnetic field has been predicted [6, 7, 60] as a stable lattice phase and as meta-stable single states surrounded by FM order. Here, the DMI stops the skyrmion from unwinding to the trivial state. Moreover, DMI has the same consequences for the shape of the skyrmions than for the spin spiral which means they have a unique sense of magnetization rotation and they can be divided into helical (Bloch-

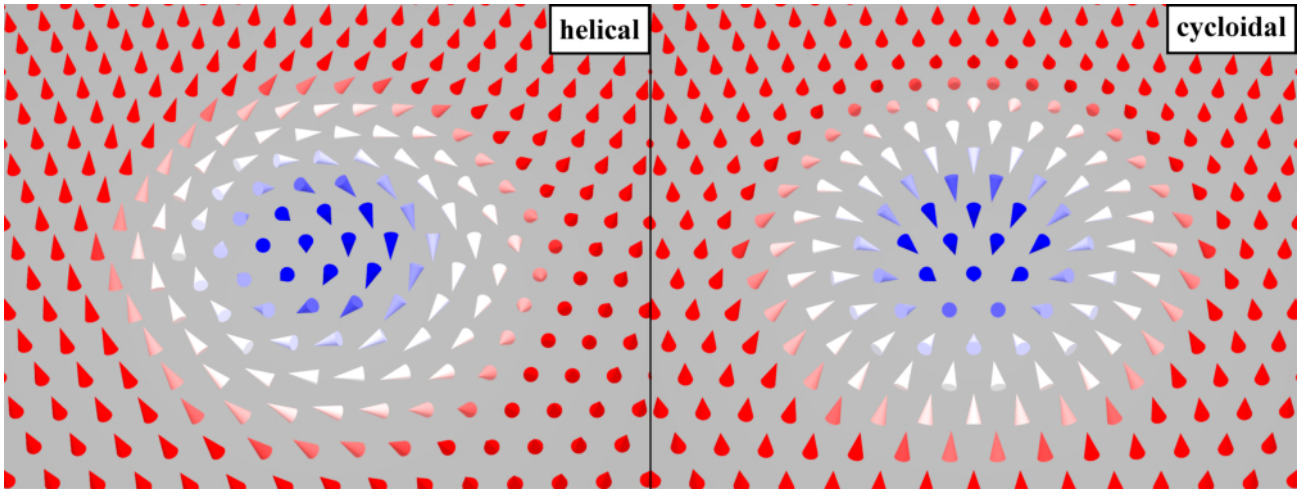

Figure 2.3: Illustration of a helical (Bloch-like) and a cycloidal (Néel-like) skyrmion in a two-dimensional system with the cones corresponding to the local orientation of the magnetic moments. If the DMI vector $\boldsymbol{D}$ is collinear (perpendicular) to the connecting line between magnetic moments the helical (cycloidal) arrangement is preferred.

type) or cycloidal (Néel-type) skyrmions, see figure 2.3. Since 2009 several different systems have been found that exhibit a skyrmionic phase due to non-negligible strength of DMI. In these, the DMI either results from the intrinsically non-centrosymmetric material [12, 61–68] or from the symmetry breaking at interfaces [14, 22–24, 26]. Most of these systems show a spin spiral as their ground state and the application of an external field is necessary to reach the skyrmion lattice or a mixed state that exhibits meta-stable skyrmions within a FM order. For a strong enough anisotropy the meta-stable state can exist without an external field [7]. For increasing external magnetic fields the size of single skyrmions and the skyrmions in lattices decreases [69]. However, the change of interaction coefficients shows an opposite trend for the size of single skyrmions or those in the lattice. The size of the lattice skyrmions behaves very much like the spin spiral period which means they shrink for an increase in DMI and grow for an increase in exchange stiffness and anisotropy. Contrary, it is the opposite trend for single meta-stable skyrmions [28–30].

2.3 Scanning tunneling microscopy

The exploitation of electron tunneling in a scanning probe method for surface investigations was first published in 1982 [70]. Until then tunneling junctions were realized by two electrodes that were fixed and separated from each other by a thin insulating film through which the electrons tunneled. In STM one of the electrodes is held few Å above the other electrode separated only by vacuum. The distance and the lateral location of the electrodes are tuned by piezo elements and the resulting changes can be measured which opened new possibilities for surface investigations down to atomic resolution. Today

STM is a well-known tool and hence extensive literature already exists [71–73].
In this section I will give a brief introduction to quantum-mechanical tunneling focused on the relevance for STM theory and SP-STM, which is the extension towards the field of magnetism. Finally, I explain the common mode of operation and its typical application.

2.3.1 Quantum-mechanical tunneling

Tunneling of electrons through insurmountable barriers is forbidden in classical physics, only the particle-wave dualism established in quantum mechanics can explain the experimental facts of quantum tunneling. This phenomenon is the basis of STM and leads to the measured tunneling current. The following sections will give a short explanation beginning with a model for planar junctions.

Bardeen model

Bardeen gave an expression for the current between two electrodes separated by an insulator [74]. He viewed the tunneling as single electron events between the two electrodes which result in a net current. He gave the following expression for the net current I between two electrodes, i. e., tip and sample:

$$I = \frac{2\pi e}{\hbar} \sum_{\nu,\mu} \Big[f(E_\nu - E_{\mathrm{F,t}}) - f(E_\mu - E_{\mathrm{F,s}}) \Big] \left| M_{\nu\mu} \right|^2 \delta(E_\nu - E_\mu) \tag{2.2}$$

where $f(E)$ is the Fermi-Dirac distribution and $E_{\mathrm{F,t/s}}$ the Fermi energy of tip or sample. The tunneling current is governed by energy conservation, the electron distribution within tip and sample, and the tunneling likelihood expressed by the tunneling matrix element $M_{\nu\mu}$:

$$M = -\frac{\hbar^2}{2m} \int_{\partial A} \left(\Psi_\nu{}^* \nabla \Psi_\mu - \Psi_\mu{}^* \nabla \Psi_\nu \right) \mathrm{d}A$$

as a surface integral over ∂A which are the surfaces within the tunneling barrier. The determination of $M_{\nu\mu}$ is the most challenging part of the current formula. $M_{\nu\mu}$ depends on the wave functions for the sample Ψ_μ and the tip Ψ_ν, which is influenced by the unknown shape of the tip. Therefore, an approximation for Ψ_ν is necessary for exact calculations.

Tersoff and Hamann theory

The first approximation for the tip wave function has been suggested by Tersoff and Hamann [75]. They used Bardeen's formula and treated Ψ_ν as a radially symmetric wave function with the decay coefficient k that has to fulfill the Schrödinger equation in vacuum:

$$\Psi_{\mathrm{t}} \propto \frac{\mathrm{e}^{-kr}}{r}$$

with the distance r between sample and tip center $\vec{r}_0$, see figure 2.4. For further simplification the limit of low temperatures ($T \to 0$) is assumed which allows them to approximate the Fermi-Dirac distribution by step functions. With the introduction of density of states (DOS) for tip and sample the expression for the current reduces to:

$$I \propto \rho_{\mathrm{t}}\left(E_{\mathrm{F,t}}\right) \int_0^{eV} \rho_{\mathrm{s}}\left(\vec{r_0}, E_{\mathrm{F,s}} + E\right) \mathrm{d}E$$

The current varies with the integral of the sample's DOS from the Fermi energy to an applied voltage. In the limit of low applied voltages V the tunneling current simplifies to a more instructive expression:

$$I \propto V \rho_{\mathrm{t}}\left(E_{\mathrm{F,t}}\right) \rho_{\mathrm{s}}^{local}\left(\vec{r_0}, E_{\mathrm{F,s}}\right)$$

where $\rho_{\mathrm{s}}^{local}\left(\vec{r_0}, E_{\mathrm{F,s}}\right)$ is the local density of states (LDOS) of the sample at the tip center position. Local means that the DOS is space-resolved. Moreover, it is important that the current depends on the sample's LDOS at the tip's center position. The LDOS depends on the sample's wave function which in turn decays exponentially towards the tip resulting in the exponential distance dependence of the tunneling current:

$$\rho_{\mathrm{s}}^{local}\left(\vec{r_0}, E_{\mathrm{F,s}}\right) \propto \left|\Psi_\mu\left(\vec{r_0}\right)\right|^2 \propto \mathrm{e}^{-2kr}$$

In this simplified model the differential tunneling conductance dI/dV depends on the LDOS of tip and sample and with high sensitivity on the distance between sample and tip. Thus, in STM the dI/dV signal is measured which opens up the possibility to investigate conducting samples' LDOS on an atomic scale.

In general the situation is more complex because the tip and sample wave functions correspond to p- or d-wave like functions. In this case M is determined by the spatial derivatives of the wave function at the tip center [76]. This can lead to atomic corrugations that are several orders of magnitude higher than for the s-wave-like wavefunction model and are necessary to understand the observed atomic resolution [77].

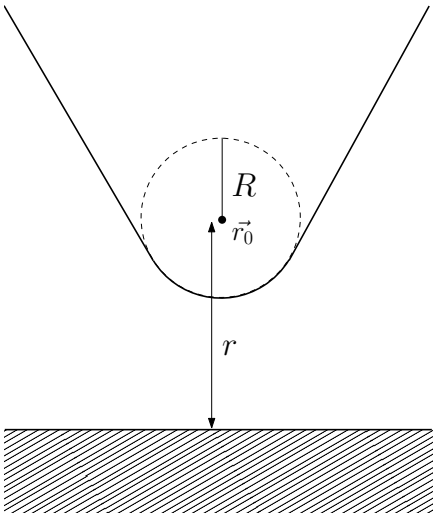

Figure 2.4: Sketch of the radially symmetric STM tip with apex radius R

2.3.2 Spin polarization

As electronic properties and magnetism are intertwined the tunneling current also depends on the magnetic state of tip and sample which was neglected until now. A summary of spin polarization in STM can be found in [78, 79].

For a planar tunnel junction consisting of two insulator-separated FM electrodes the tunneling current usually decreases for an antiparallel orientation of the electrodes' magnetization [80]. This behavior is caused by the splitting of the DOS in majority $\rho_\uparrow$ and minority $\rho_\downarrow$ spin direction. The difference of these DOS determines the FM's magnetization which is often expressed as a polarization $P(E_F)$ as follows:

$$P\left(E_F\right) = \frac{\rho_\uparrow\left(E_F\right) - \rho_\downarrow\left(E_F\right)}{\rho_\uparrow\left(E_F\right) + \rho_\downarrow\left(E_F\right)}$$

If the tunneling is completely elastic, the electrons cannot change their spin state and are only allowed to tunnel into the DOS of the same spin direction. Consequently, the electron from a majority state of one electrode has only the minority states of the other electrode available if the magnetization directions are aligned anti-parallel, as illustrated in 2.5 b. Hence, the current reduces which means the resistance increases because of the relative misalignment between the electrodes' magnetization. This phenomenon is called tunneling magnetoresistance (TMR). In the limit of vanishing applied voltage the conductance G of a planar tunneling junction of two FM electrodes with the spin polarizations P_t and P_s can be expressed by [81]:

$$G = G_0\left(1 + P_t P_s \cos\left(\theta\right)\right) \tag{2.3}$$

where G_0 is the conductance in absence of any magnetization and θ the angle between the magnetizations. The conductance and likewise the tunneling current consists of an electronic part G_0 and a magnetic component that scales with the scalar product of both magnetizations. If one of the electrodes is non-magnetic, corresponding to zero polarization, the magnetic contribution to the tunneling current vanishes.

This expression for the conductance also holds for an STM with a magnetic tip and sample. The only differences to the planar junction are the shape of the tip and the tunneling barrier being vacuum instead of an insulating material. Concerning TMR the tip magnetization is determined by the closest atom due to the exponential distance dependence of the tunneling current. In contrast to the insulating material, the vacuum suppresses spin-flips meaning that the assumption of spin conservation is even better suited for STM than for magnetic planar junctions. Therefore, an SP-STM can exploit TMR to investigate the magnetism of surfaces down to the atomic scale. This was first demonstrated by R. Wiesendanger [82]. Wortmann *et al.* suggest a more general expression that is valid for non-vanishing voltages [83]. They used Bardeen's result, see equation 2.2, and extended it with two component spinors for the wave functions:

$$\boldsymbol{\Psi}^{\mathrm{s/t}}_{\mu/\nu} = \begin{pmatrix} \Psi^{\mathrm{s/t}}_{\mu/\nu,\uparrow} \\ \Psi^{\mathrm{s/t}}_{\mu/\nu,\downarrow} \end{pmatrix}$$

By introducing LDOS $\rho_{\mathrm{s/t}}$ and magnetic LDOS $\boldsymbol{M}_{\mathrm{s/t}}$ for tip and sample including the Pauli's spin ma-

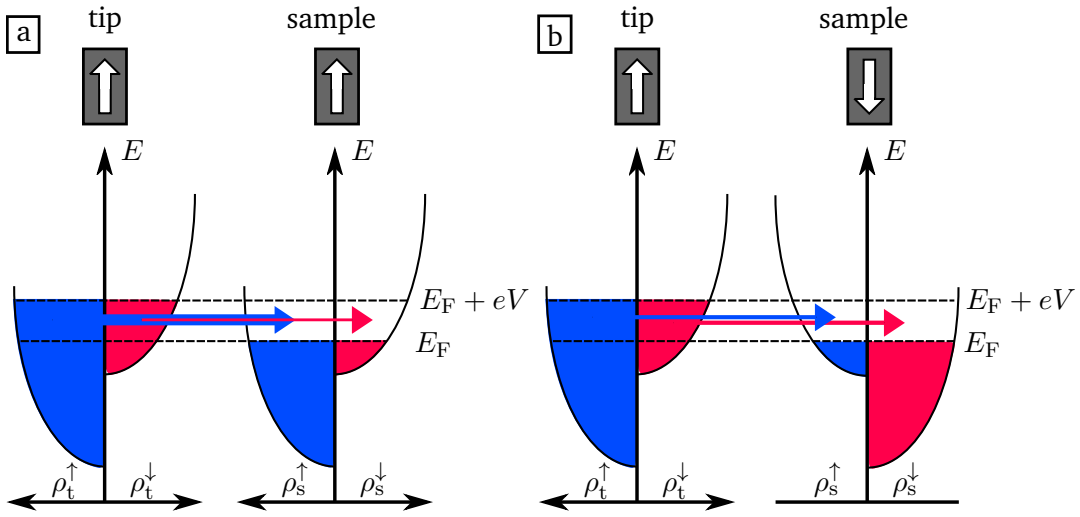

Figure 2.5: Illustration of tunneling current between two FM electrodes,i. e., tip and sample. Their electron DOS is split into majority $\rho^\uparrow$ and minority DOS $\rho^\downarrow$ with the tip magnetization defining the quantization axis. The tunneling current scales with the electrodes' DOS of same spin orientation. Consequently, the current depends on the relative magnetization orientation of the electrodes which is (a) parallel or (b) antiparallel.

trix $\boldsymbol{\sigma}$ and the position of the tip $\boldsymbol{r}$:

$$\boldsymbol{M}_\mathrm{s}(\boldsymbol{r}, E) = \sum_\mu \delta\left(E_\mu - E\right) \boldsymbol{\Psi}_\mu^{\mathrm{s}\dagger}(\boldsymbol{r}) \boldsymbol{\sigma} \boldsymbol{\Psi}_\mu^\mathrm{s}(\boldsymbol{r})$$
$$\rho_\mathrm{s}(\boldsymbol{r}, E) = \sum_\mu \delta\left(E_\mu - E\right) \boldsymbol{\Psi}_\mu^{\mathrm{s}\dagger}(\boldsymbol{r}) \mathbb{1} \boldsymbol{\Psi}_\mu^\mathrm{s}(\boldsymbol{r}),$$

an expression very similar to equation 2.3 can be derived, if spin conservation and energy independence of the tip's LDOS ρ_t and magnetic LDOS $\boldsymbol{M}_\mathrm{t}$ are assumed:

$$I(\boldsymbol{r}, V) \propto \rho_\mathrm{t} \widetilde{\rho}_\mathrm{s}\left(\boldsymbol{r}, V\right) + \boldsymbol{M}_\mathrm{t} \widetilde{\boldsymbol{M}}_\mathrm{s}\left(\boldsymbol{r}, V\right)$$

The tunneling current is again divided into a non-magnetic part and a magnetic part which scales with the projection of the sample's magnetization onto the magnetization of the tip and vanishes if either sample or tip are non-magnetic. The bias voltage dependence of the sample is accounted for by the introduction of the integrated LDOS $\widetilde{\rho}_\mathrm{s}$ and $\widetilde{\boldsymbol{M}}_\mathrm{s}$. The integrated LDOS follows from the energy integration of the energy-dependent LDOS from Fermi energy E_F to the energy of the applied voltage eV. This integration can be circumvented by measuring the differential tunneling conductance dI/dV that depends on the LDOS at the energy of the applied bias voltage:

$$\frac{dI}{dV}(\boldsymbol{r}, V) \propto \rho_\mathrm{t} \rho_\mathrm{s}\left(\boldsymbol{r}, E_\mathrm{F} + eV\right) + \boldsymbol{M}_\mathrm{t} \boldsymbol{M}_\mathrm{s}\left(\boldsymbol{r}, E_\mathrm{F} + eV\right)$$

The dI/dV can simplify imaging the magnetic structure as it allows the experimentalist to choose a bias voltage where the magnetic LDOS dominates over the non-magnetic one. This is more difficult with the current as it is determined by the LDOS integrated over a whole energy range.
In summary, the tunneling current depends on the distance between the tip and the sample, the chemical composition and the magnetic state. All three properties influence the same physical value which is the tunneling current. Therefore, the challenge in evaluation of STM data is to disentangle all of these three components. Especially for the unambiguous identification of non-collinear magnetic structures carefully planned experiments are necessary as it requires not only a tip with adequate resolution but also the knowledge of the tip's magnetization, which is in general unknown. In section 3.1 I will explain the consequences for the experimental setup and approach.

2.3.3 Mode of operation

The STM tip is scanned over a certain area by a tube scanner while the tunneling current is measured in order to record complete maps of surfaces. This can be achieved in different ways.
From the technical point of view the easiest way to scan is with a fixed height of the STM tip which results in a map of the tunneling current $I\left(x,y\right)$. However, in this mode the tip can easily collide with the sample during the scan as the tip is only few Å away from the sample and the sample height usually changes. For this reason the **constant-current mode** is usually used which employs a feedback loop that adjusts the tip's height to keep the tunneling current at a set value. This continuous height adjustment keeps the tip safe from collisions and offers a map of the relative heights on the surface, $z\left(x,y\right)$, which conveys the same information as the tunneling current map.
Besides a current and height map I also recorded maps of the differential tunneling conductance with the help of a lock-in amplifier. A lock-in amplifier extracts the amplitude of a sine modulation with a certain frequency ω from a current signal. In order to yield the differential tunneling conductance the applied constant bias voltage V_0 is modulated by $V_1 sin(\omega t)$. For low modulation voltages a Taylor expansion of the tunneling current in V_0 shows that the amplitude measured by the lock-in amplifier will consist of the modulation voltage V_1 and the desired differential tunneling conductance $\frac{\mathrm{d}I}{\mathrm{d}V}$:

$$I(V) = I(V_0) + \underbrace{\left.\frac{\mathrm{d}I(V)}{\mathrm{d}V}\right|_{V=V_0}}_{\text{measured amplitude}} V_1 \; sin(\omega t) + \ldots$$

The differential tunneling conductance was measured simultaneously with the height map in the constant-current mode.

Chapter 3
3 Experimental setup

This chapter introduces the instruments that I used for all my investigations. The central component is an STM in a magnetic vector field, generated by three superconducting split-pair coil magnets, at low temperatures. The STM is embedded in an ultra-high vacuum (UHV) chamber and connected to further UHV chambers which allow the preparation and investigation of samples in vacuo. Moreover, I will present the preparation of tips and samples for my studies.

3.1 Motivation for a vector-field STM

SP-STM excels in investigations of the magnetism in electrically conducting nanostructures of sizes below 100 nm. Therefore, SP-STM is well-suited to study non-collinear magnetism in nanostructures. As mentioned in section 2.3.2, the resulting contrast in SP-STM depends on the projection of the sample's magnetic moment onto the tip's magnetization, which is in general unknown. Thus, it is either difficult or only possible to a limited degree to determine the magnetic structure. However, this problem can be solved by employing a tip with a field-dependent magnetic moment that can be arbitrarily reoriented with three orthogonally mounted magnets that have their common center at the STM. This does not only make it possible to easily take scans of the same area in different magnetic field, but also the exact orientation of the tip's magnetization is known as long as the external field is applied. Magnetic structures that respond to external magnetic fields can be investigated in a similar way. In this case the roles of sample and tip are reversed. The tip material is chosen to be magnetic but field-independent. SP-STM maps with such a tip show the change in the magnetism of the sample due to the external magnetic field. For all my experiments I used such an STM with a triple-axes vector magnet which enables me to determine the complete magnetic structure of every electrically conducting nanostructure.
In the following sections I will describe the laboratory setup and the STM, that have already been described in more detail by S. Meckler [84, 85].

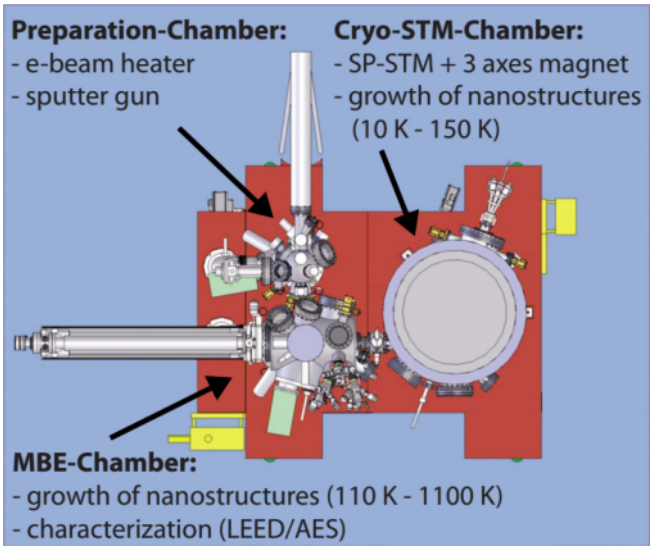

Figure 3.1: Top-view sketch of the vector-field STM and the UHV chamber system mounted on a vibration-isolation table (marked red). Reprinted from [84], with the permission of AIP Publishing.

3.2 Multi-chamber UHV system

Figure 3.1 shows a top-view sketch of the UHV chamber system used. It consists of the Cryo-STM-Chamber that houses the STM and a cryostat to operate the STM at low temperatures of down to 4.7 K. Before samples can go into the STM, they are first transferred through an airlock chamber which is mounted on the Preparation-Chamber in the UHV chamber system. Afterwards the sample's surface is cleaned in the Preparation-Chamber and then nanostructures can be grown in the MBE-Chamber. Finally, the sample is transferred into the STM. The complete UHV system is mounted on top of a table that is decoupled from the ground by pneumatic dampers that reduce mechanical noise with frequencies higher than few Hz. This table in turn stands on a block of concrete that is decoupled from the building foundation due to its large inertia. Ion getter and titanium sublimation pumps keep the system at a base pressure of 1×10^{-10} mbar and lower.

Preparation-Chamber

All sample cleaning methods lead to or require gas emission resulting in pressures between 10^{-10} and 10^{-5} mbar. For this reason, the use of a dedicated chamber for cleaning processes prevents unnecessary contamination of the other chambers. The combination of a sputter gun and a piezo-driven leak valve between the chamber and a gas bottle containing Ar allows to clean surfaces by Ar^+-ion sputtering. It is possible to heat the sample up to 1100 K with a PBN[1]-heater during the sputter process. Furthermore, a separate stage with an electron-beam heater is available that can heat up samples and

[1] pyrolytic boron nitride

tips to temperatures higher than 2200 K. Other gas inlets with leak valves allow precise dosing of process gases, for example, oxygen. Hence, samples can be annealed in special atmospheres for cleaning purposes.

MBE-Chamber

The purpose of this chamber is to grow metallic nanostructures on top of the cleaned samples. For this reason, up to seven MBE devices can be installed that evaporate and deposit different metals on samples and tips from crucibles or rods by electron-beam evaporation with a variable deposition rate. Throughout the metal deposition the sample stays on a modified manipulator head from Omicron which has two separate stages for either heating or cooling the sample. The same PBN-heater as in the Preparation-Chamber is used for heating, which allows precise control of the temperature up to 1100 K. In contrast, the cooling stage uses liquid nitrogen that cycles through a copper block on the stages backside and manages temperatures down to 110 K. The temperatures of both stages can be checked via type-K thermocouples. Furthermore, a standard instrument for low energy electron diffraction (LEED) and Auger electron spectroscopy (AES) is installed in this chamber. AES is used to identify the chemical elements on a sample surface. I used it to quickly detect carbon contamination on Ir(111). Moreover, LEED is useful for analyzing the surface structure of samples by visualizing their inverse periodicity.

3.3 The STM and its UHV chamber

The main part of the Cryo-STM-Chamber is a two-stage bath cryostat that hangs from the chamber's top and is decoupled from the the rest of the chamber by additional pneumatic dampers. The inner stage of the bath cryostat is filled with liquefied ^{4}He which is shielded from radiation by a surrounding second stage, i. e. a chamber filled with liquid nitrogen, to decrease heat dissipation. Furthermore, an additional pump is used on the second stage to reduce the pressure below 5 mbar and hence freeze the nitrogen which avoids vibrations due to nitrogen boiling. Additionally, the temperature of the frozen nitrogen is decreased to 63 K which further reduces heat dissipation to the helium stage. The actual STM is mounted on the cryostat from below. It is always rigidly connected to the inner stage of the cryostat and thus reaches a temperature of about 4.7 K. The superconducting coil magnets are placed within the inner cryostat and have to be covered by liquefied ^{4}He throughout their whole operation time. This limits the available time for experiments using magnetic fields to about 22 h, which is the time after the recommendable maximum volume of 105 l has reduced to 56 l, which is the minimal volume necessary for operating the superconducting coils. For measurements that do not include external fields the maximum time the cryostat keeps its low temperature increases to roughly 48 h. Due to its low temperature and the large surface the cryostat acts as a cryo-pump decreasing the base pressure to the lower 10^{-11} mbar range. If the cryostat warms up the cryo-pump will set all of its

bound contaminants free over a short period of time. For this reason, a non-evaporable getter (NEG) pump is installed to avoid the otherwise extreme pressure increase in the chamber.
The magnet consists of three split-coil pairs that are orthogonally oriented with their common center being the STM, see figure 3.2. This allows direct access to the STM through a vertically retractable double shutter and thus a quick and safe insertion and removal of the STM tip and samples. The shutters are thermally decoupled from each other but coupled via copper braids to their corresponding cryostat stages. If only one of the split-coil pairs is used, the magnets allow the application of up to $\pm 5\,\mathrm{T}$ out-of-plane and $\pm 1.3\,\mathrm{T}$ in every in-plane direction of the sample. If the magnets are used at the same time, their highest allowed fields are $\pm 3\,\mathrm{T}$ and $\pm 1\,\mathrm{T}$, respectively.

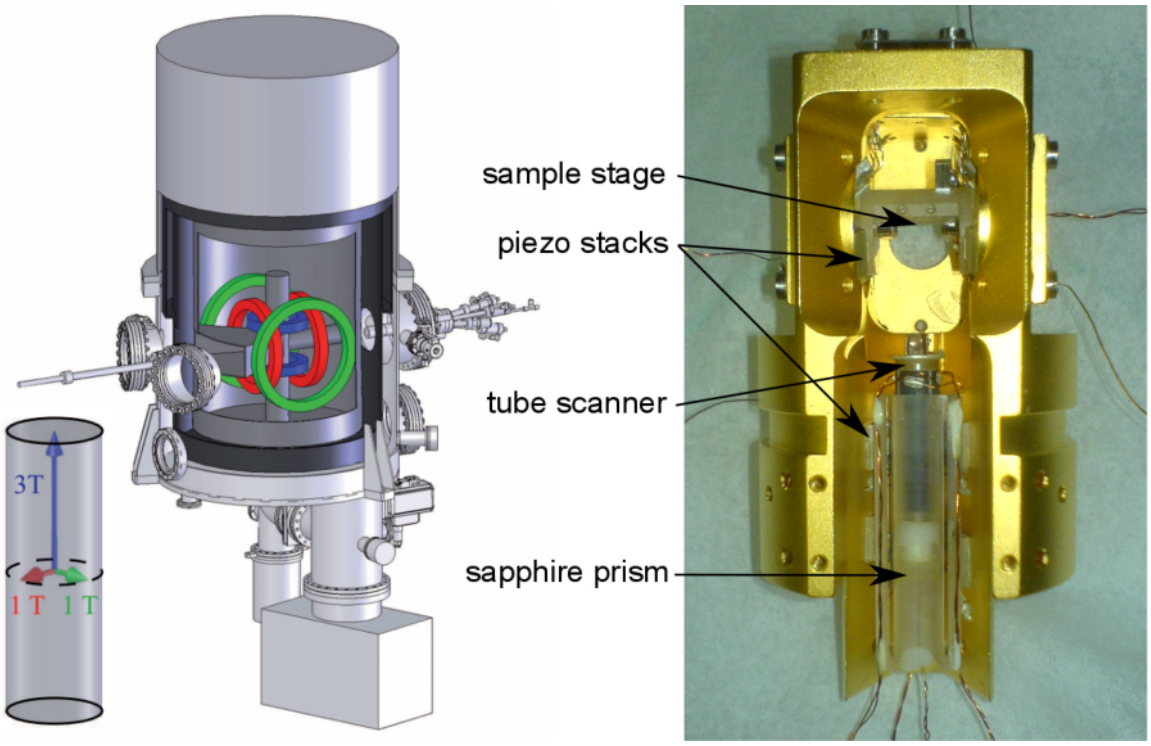

Figure 3.2: Cutaway view of the vector-field Cryo-STM-chamber with the split-pair coils highlighted by colors and their respective highest applicable fields if used together. Reprinted from [84], with the permission of AIP Publishing. Image of STM upper body including all parts except tip, sample and last part enclosing the sapphire prism.

The construction of the STM is based upon a previous work described in [86]. The STM body is made of gold-plated phosphor bronze ($CuSn_8P$) which is fixed on top of a column made from oxygen-free highly conductive (OFHC) copper that is screwed to the bottom of the inner stage of the cryostat. In the STM body a sapphire prism is held by six shear piezo stacks. In the sapphire prism a scanner tube with the STM tip is mounted pointing upwards. The scanner tube enables the tip to scan within a range of $1.76\,\mu\mathrm{m}\times 1.76\,\mu\mathrm{m}$ at 4.7 K and $2.9\,\mu\mathrm{m}\times 2.9\,\mu\mathrm{m}$ at room temperature for maximum applied

voltages of $\pm 100\,\mathrm{V}$[2]. The coarse motion is realized by application of an asymmetric sawtooth voltage on the shear piezos which leads to a slip-stick motion of the sapphire prism. The sample is sitting top-down in a sapphire half-cylinder that is also held by piezo stacks which enable a rotation of the sample around an axis perpendicular to the tip axis. The intent is to rotate the sample in a position that allows the deposition of metal atoms *in situ* through a bore in the STM body, see image of the STM upper body in figure 3.2. Hence, a second vertically retractable double shield is installed to allow the deposition of single atoms via MBE. All electronic signals are transmitted by Kapton covered stainless steel twisted-pair cables that are pressed into ridges of the copper body to reduce their temperature difference at the STM side to less than 1 mK. Outside of the Cryo-STM-Chamber the tunneling current is amplified by a transimpedance amplifier manufactured by Femto [87] and then managed by Nanonis SPM control electronics [88] including all other electronic signals concerning the STM.

3.4 Tip & sample preparation

As tip base material I used tungsten and chromium. Throughout all SP-STM measurements with a field-independent tip I used a Cr bulk tip that was manufactured by my coworker Dr. C. Hanneken as described in [89, 90]. Chromium is antiferromagnetic with a Néel temperature of 311 K and thus can be used for SP-STM as a field-independent tip [78, 79, 91, 92] with a stray field several times smaller than FM tips [89] at typical measurement distances of 6 Å. Therefore, this kind of tip is a good choice for samples that are very sensitive to magnetic fields. The Cr bulk tip is glued into the holder and was used in the STM without any further treatment. I produced several W tips via electrochemical etching similar to [93]. Thanks to the mechanical properties of W they could be fixed without glue enabling me to clean the tips via annealing to about 1500 K for 12 s. Since W is non-magnetic it is usually used for conventional STM, but it can also be applied to study the magnetism via certain effects that change the sample's electronic properties depending on the magnetism, e. g. NCMR, see section 4.3.1. However, by coating this cleaned W tip with a magnetic material it can be used for SP-STM. Within my studies I covered W tips with amounts of Fe that correspond to a layer thickness of roughly 10 nm or 40 ML. Afterwards they were annealed at about 700 K for 8 min to smooth the tip's surface. This leads to a strong magnetic moment of the tip that prefers an in-plane orientation [78, 79, 94–96]. The FM nature of the Fe coating means that the tip will exhibit a significant stray field but also that its magnetic moment can be reoriented by an external magnetic field. For this reason, the Fe-coated W tip can be used to study the non-collinear magnetism of samples that are insensitive to external fields below several Tesla.

The basis of all samples were several Ir(111) single crystals [97] which are bound via tungsten wires on tungsten plates. At first the surface of the single crystal has to be cleaned which is achieved by sputtering the surface with Ar^+ ions that are accelerated with a voltage of 800 V and an Ar partial pressure

[2] Applications of up to 150 V were tested which would correspond to a higher scan range but a lower resolution

of about 6×10^{-5} mbar. Subsequently, the sample is annealed at a temperature of roughly 1200 K for 3 min in order to let the atoms form smooth atomic layers. Since Ir crystals exhibit a non-negligible contamination with carbon that disturbs the growth of nanostructures, the carbon concentration on the surface has to be depleted by repeated annealing in an oxygen atmosphere. Therefore, I subjected every Ir crystal at the beginning and then every few weeks to several cycles of annealing in partial pressures of oxygen ranging from 1×10^{-6} to 1×10^{-7} mbar. An annealing cycle consisted in an increase of the heating power from 0 to 40 W by 10 W steps over 10 min until about 1200 K were reached and a subsequent cooling phase of also 10 min. I repeated this between three and six times for each of three different decreasing partial pressures. Afterwards, another cycle of sputtering and annealing in UHV was necessary to have a clean surface.

The next step for all sample preparations consisted in the deposition of Fe via electron-beam evaporation from a 2 mm thick Fe rod of highest available purity (99.99%) [97]. Despite its high purity the Fe rod still exhibits a significant amount of carbon impurities. However, the increase of the diffusion coefficient of carbon with temperature can be exploited to move the carbon away from the part that is used for evaporation. I heated the Fe rod locally which leads to the accumulation of the carbon in the colder part due to the difference in diffusion coefficients. By moving the rod every 45 min by 2 mm into the chamber the heating zone is moved through the rod and thus the carbon accumulates at the rod's end. The Fe rod has to be subjected to this procedure only once. I deposited amounts of Fe equivalent to coverages between 0.7 and 3.3 ML with a deposition time of about 3 min per ML and at a pressure of around 2×10^{-10} mbar in the chamber. Before and during the Fe deposition the sample was kept at an elevated temperature to make the Fe form continuous films. In the case of single Fe layers I used a constant temperature of about 200 °C and for the growth of higher layers I increased the temperature linearly throughout the deposition from 170 to 220 °C. A subsequent Pd deposition from an electron-beam evaporated 99.99% pure Pd rod of 2 mm diameter [98] needed a lower deposition temperature to avoid alloying with the Fe. In the case of the Pd/Fe bilayer I kept the sample temperature between 110 and 130 °C while for the Pd deposition on higher layers of Fe, I waited until the sample reached room temperature. At elevated temperatures the Pd grows predominantly at the lower part of the step edge which can be a problem for samples with several Fe layers since higher layers begin to grow before the previous once are closed. In this case the topmost Fe layer will exhibit no Pd islands and thus a deposition at room temperature is necessary to have Pd islands on all Fe layers. In all cases I deposited between 0.3 and 0.5 ML of Pd at a pressure of about 2×10^{-10} mbar.

Chapter 4

4 Previous studies

This chapter summarizes the knowledge of the systems used in this thesis, i.e. different multilayers of Fe on Ir(111) and the monolayer (ML) of Pd on different layers of Fe on Ir(111), gathered by previous experiments.

4.1 Double layer (DL) of Fe on Ir(111)

The following section is based on the results from [99]. This study investigated the structure and magnetism of the second atomic layer of Fe on Ir(111) via STM and SP-STM at low temperatures. While the first atomic layer of Fe grows pseudomorphic on the Ir(111) [100], the second atomic layer of Fe grows as either reconstructed or pseudomorphic and strained areas.

Reconstructed area

STM constant-current maps at 8 K show that the characteristic feature of the reconstructed areas are the dislocation lines which grow perpendicular to the close-packed rows of the substrate. Here, the distance between two dislocation lines is roughly 5.2 nm, see figure 4.1 a. Moreover, these dislocation lines appear in three rotational domains due to the hexagonal symmetry of the substrate. Figures 4.1 b and c demonstrate that the contrast of the dislocation lines depends on the bias voltage used. Therefore, reconstructed areas always have to be compared at the same bias voltage. With the assumption that the first layer stays pseudomorphic the resulting contrast in figures 4.1 a-c can be explained by the structure model shown in figure 4.1 d. It consists of two alternating lines of hcp- and fcc-like stackings which are hollow site dislocation lines h_1 and h_2, see figures 4.1 b-d. Between these dislocation lines the other Fe atoms are stacked in a bcc-like way. These Fe atoms between the dislocation lines are laterally shifted because of the lattice mismatch between Fe and Ir. The reconstructed areas experience a uniaxial compression of about 5 % perpendicular to the dislocation lines. Furthermore, the alternating stackings of the dislocation lines lead to a periodic change of the bcc-like areas' growth directions after every dislocation line, see the blue rectangles and the dotted arrows in figure 4.1 d. This alternation of the growth directions results in a characteristic zigzag-like structure.
The magnetism of the reconstructed areas was investigated by SP-STM in different magnetic fields at low temperatures. Figure 4.2 a reveals a magnetic structure with a period length between 1.6 and 1.9 nm that is guided by the dislocation lines. Again, the appearance depends on the applied bias

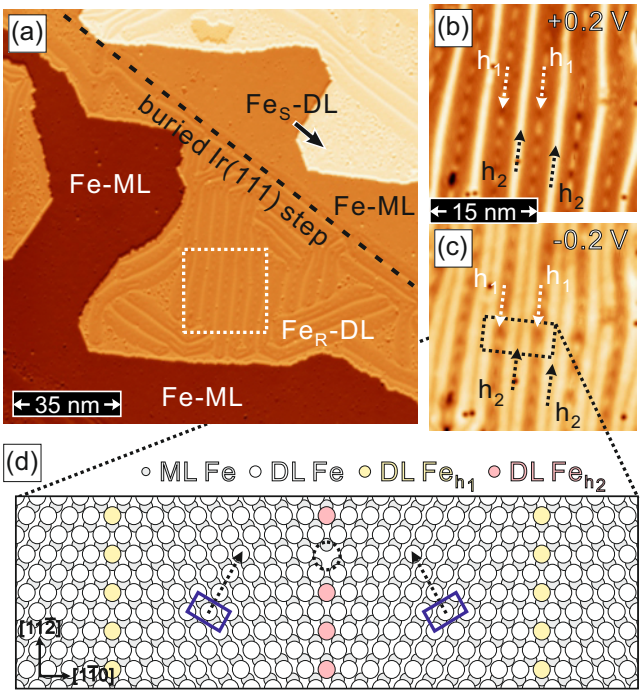

Figure 4.1: (a) STM topography of about 1.6 atomic layers of Fe on Ir(111) (Measurement parameters: $U = 0.2$ V, $I = 1$,nA, $T = 4.8$ K). The Fe-DL consists of reconstructed (R) and strained (S) areas. (b),(c) Magnified topography images (see box in (a)) of a reconstructed area with periodic dislocation lines due to uniaxial strain relief taken at $U = +0.2$ and $U =$ -0.2 V, respectively. (d) Atomic structure model of the reconstructed Fe-DL with a 5 % horizontally compressed Fe top layer on a pseudomorphic hexagonal Fe bottom layer; this locally leads to bcc(110)-like areas (blue rectangles) separated by hollow site dislocation lines (yellow, pink). Reprinted figure with permission from [99]. Copyright (2016) by the American Physical Society.

voltage; compare figures 4.2 a and b. Further measurements with different in-plane fields and a tip with a field-dependent magnetic moment proved that the magnetic ground state is a cycloidal spin spiral. The wavefronts exhibit a zigzag structure with its kinks at the dislocation lines. This zigzag pattern suggests that the spin spiral propagates along the bcc[001]-direction of the patches in between the dislocation lines. A comparison of the measured angle between the wavefronts and the dislocation lines with the angle expected from the proposed structure model reveals that the actual angles are larger leading to an overall straighter wavefront, see figure 4.2 c. This deviation is attributed to the kinks and thus to the impact on the system's energy by a change of the propagation direction. Moreover, the Fe-DL has been exposed to magnetic out-of-plane fields up to 9 T which led to no observable change in the magnetic structure. Additional investigations with spin-averaging STM tips provided no evidence for contrast of magnetic origin leading to the conclusion that no contrast mechanism besides TMR plays any role for this system.

Strained area

Figures 4.2 d and e depict a reconstructed area in their top-half and the strained area in their lower-half. In contrast to the guided spin spirals in the reconstructed areas, the magnetic structure in the strained area is only of short range and arbitrary in direction. A FFT of an area that consists of a reconstructed and a strained area corroborated this conclusion and revealed that the period length of the spin spirals in the strained area is reduced from 1.9 to 1.2 nm compared to the reconstructed area. The strained area often encloses the reconstructed areas in the direction perpendicular to the dislocation lines and corresponds to one of the hollow site lines in the structure model of figure 4.1 d.

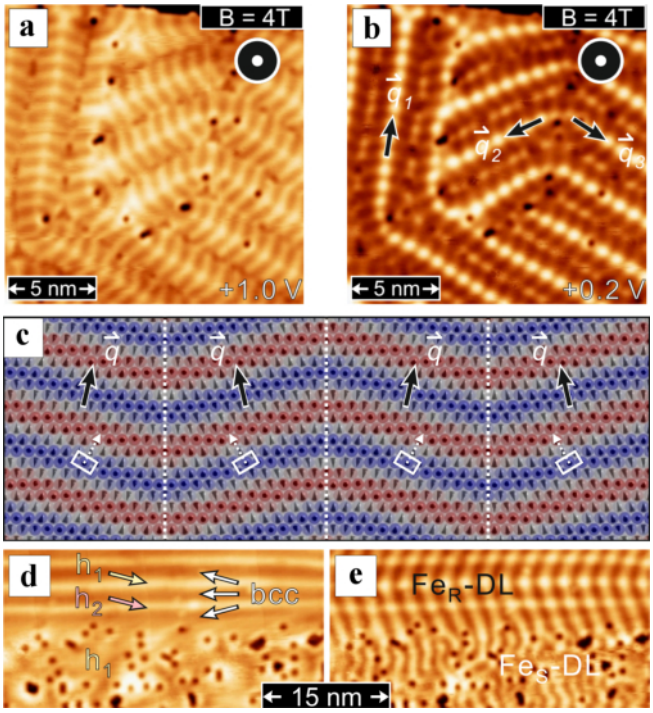

Figure 4.2: (a-b) SP-STM topography images performed in a magnetic field as marked (Measurement parameters: $I = 1\,\text{nA}$, $T = 4.8\,\text{K}$). In (b) the wavevectors $\vec{q}_1$,$\vec{q}_2$ and $\vec{q}_3$ of the spin spirals are drawn. (c) Sketch of the reconstructed Fe-DL's magnetic state including the wavevector $\vec{q}$, as deduced from the SP-STM measurements. Additionally the bcc(110)-like cell and the bcc[001] direction are drawn in white. (d) Spin-averaged topography of the Fe-DL on Ir(111) showing reconstructed (R) and strained (S) parts with the proposed hollow site dislocation lines marked, and (e) SP-STM measurement of the same area. (Measurement parameters: $U = +0.2\,\text{V}$, $I = 1\,\text{nA}$, $T = 7.8\,\text{K}$, $B_z = 0\,\text{T}$). Reprinted figure with permission from [99]. Copyright (2016) by the American Physical Society.

4.2 Triple layer (TL) of Fe on Ir(111)

Within this section I present the results of previous studies concerning the third layer of Fe on Ir(111) with STM and SP-STM. The results are based on [23, 101].

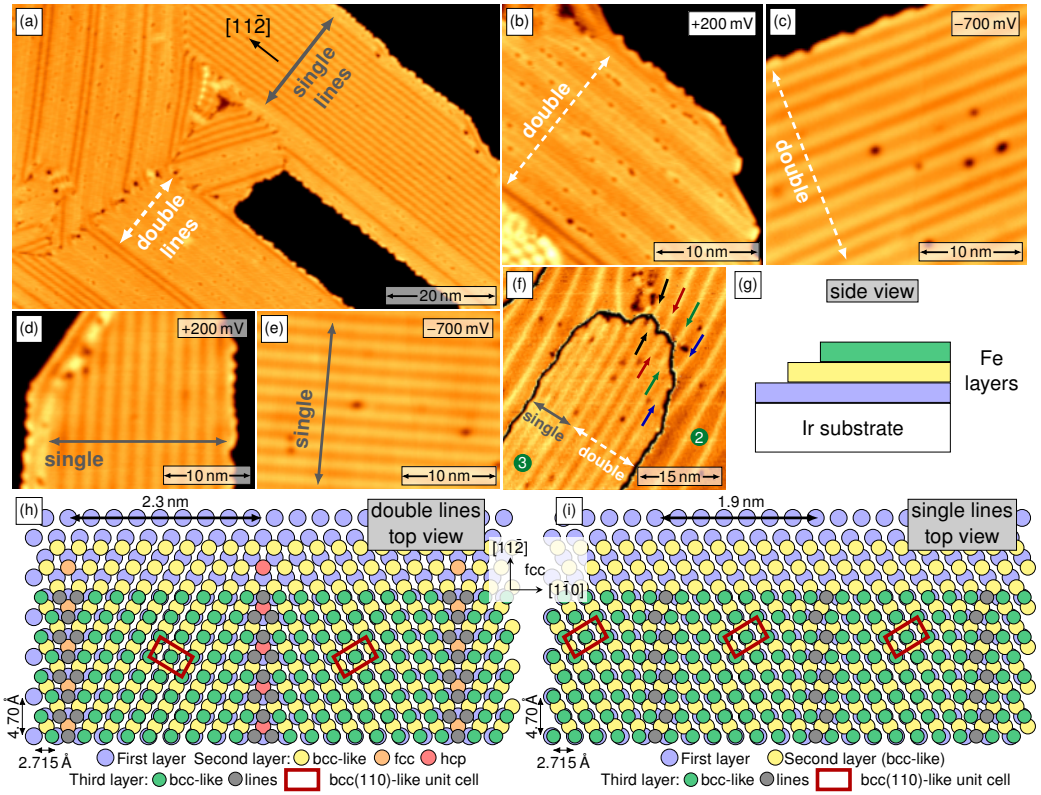

Figure 4.3: (a) Constant-current STM topography map of the Fe-TL film on Ir(111). Double and single lines are indicated by the arrows. (b),(c) Zoom-in on double line areas. At positive bias, one can see that bright and dark lines alternate and show a double line feature, whereas at negative bias, the lines look all very similar. (d),(e) STM topography of single line regions. The single lines have the same appearance at any sample bias voltage. (f) Constant-current STM topography map of a Fe-TL island on top of a DL-Fe film. The numbers in green circles indicate the local thickness of the film. The color scale was adjusted separately for the two terraces in order to highlight the matching of the dislocation lines. The areas between the bright lines on the double layer are bcc-like. (g) Side view of the triple layer Fe on Ir(111) system, indicating the color code used for the atomic structure models (h) and (i). (h),(i) Proposed atomic structure models (top view) for the Fe-TL film from the experimental observations presented in (a)-(f). Measurement parameters: I = 1 nA and (a) $U = +200$ mV, $T = 8$ K, $B = 3.5$ T; (b) $T = 5$ K, $B = 4.5$ T; (c) $T = 5$ K, $B = 3$ T; (d) $T = 8$ K, $B = 0$ T; (e) $T = 8$ K, $B = 2.5$ T; (f) $U = 700$ mV, $T = 153$ K, $B = 3$ T. Reprinted figure with permission from [101]. Copyright (2016) by the American Physical Society.

The constant-current STM topography map in figure 4.3 a reveals that the Fe-TL grows strictly in a network of dislocation lines. The Fe-TL's dislocation lines follow the direction of the Fe-DL's dislocation lines and thus orient along the $[11\bar{2}]$ direction of the Ir(111) surface. Again, three different orientations

are observed due to the hexagonal symmetry of the substrate. Two fundamentally different structures can be distinguished in the TL and are marked by two-sided arrows in figure 4.3 a. The first kind of dislocation line area consists of a strictly periodic arrangement of lines with a spacing between 1.8 nm and 2.2 nm. In contrast, the second kind of dislocation line areas exhibits two close lines followed by a larger spacing of about 2.3 nm to 3 nm between the next two lines. Hence, the first kind is called single line and the second kind double line. The appearance of the single line areas does not change qualitatively with the applied bias voltage as can be seen in figures 4.3 d and e. Contrary, the comparison of figures 4.3 b and c reveals that the characteristic structure of the double line areas can only be observed at positive bias voltages. At negative voltages they are hardly distinguishable from the single line areas. Figure 4.3 f shows double lines growing directly on the dislocation lines of the Fe-DL. The distance between the dislocation lines of the Fe-DL reduces when they approach the TL. In contrast, the single line areas grow on the pseudomorphic area of the Fe-DL. Starting from the proposed structure model of the Fe-DL [99] a model for each of the line structures is suggested in figures 4.3 g and h. In both structures the atoms of the TL follow the bcc-like structure of the DL. The difference in growth is that for the single line area of the TL a pseudomorphic growth of the DL is assumed while the double line areas grow on top of the DL's reconstructed area. Thus, the double line areas adapt to the zigzag-like alternation of the bcc growth directions in the Fe-DL with the TL's dislocation lines being on top of the ones from the DL. For the single line areas only the third layer is uniaxially compressed. The observed dislocation lines are caused by the lateral shift perpendicular to the dislocation lines. In contrast to the double line areas, the single line areas do not exhibit an alternating direction in the bcc-like area after every dislocation line. However, the structure of the single line areas can grow mirrored across a plane that is orthogonal to the surface and along the dislocation lines.

The magnetic structure of the Fe-TL structures was probed via SP-STM and STM. Figure 4.4 shows spin-resolved constant-current maps of (a) a double line area and (b) a single line area. Both exhibit a spin spiral phase as their ground state with propagation directions that are guided by the dislocation lines but are, for the largest part, tilted towards the dislocation lines. The spin spiral wavefronts in the double line area exhibit a zigzag pattern similar to the zigzag-structure that is already known from the reconstructed areas of the Fe-DL. Contrary, the wavefronts in the single line areas are tilted over the whole area by about 62° relative to the dislocation lines. In both cases the spin spirals propagate roughly along the bcc[001]-like atom rows of the TL. Again, like in the Fe-DL's reconstructed areas the spin spirals in both kinds of dislocation line areas do not exactly propagate along the atomic structure but at a larger angle to the dislocation lines, see figures 4.4 a and b. Additionally, both kinds of dislocation line areas differ significantly in their period lengths, which is about 3 to 4.5 nm for the double line areas and 5 to 10 nm for the single line areas. In both structures the period lengths exhibit the tendency to increase with a decreasing line spacing between the dislocation lines. A shorter line spacing corresponds to a stronger compression perpendicular to the dislocation line which is along the Ir's fcc $[1\bar{1}0]$ direction. Thus, a stronger compression leads to higher period lengths. While it is already

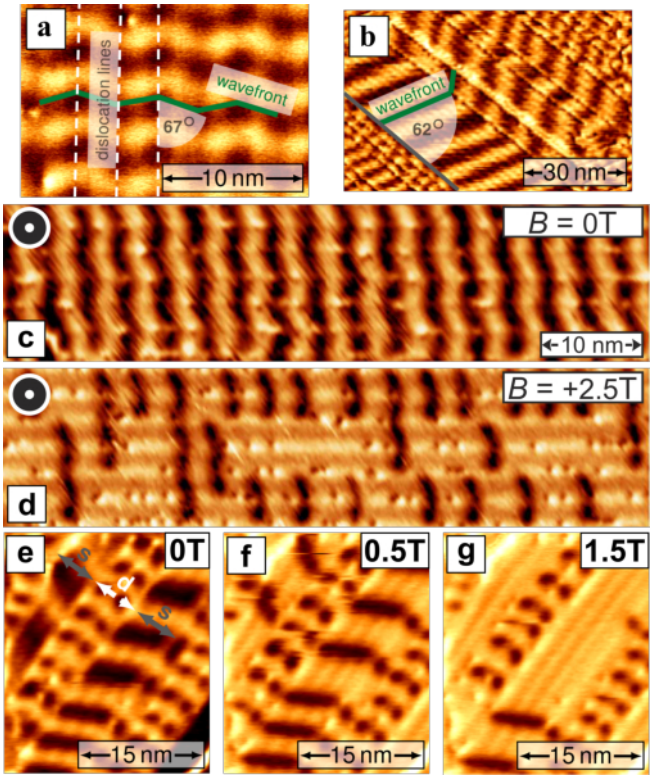

Figure 4.4: Spin-resolved differential tunneling conductance maps of (a,c-d) a double line region, (b) a single line region and (e-g) a mix of both area types as marked. In the double line areas the spin spiral propagates along the dislocation lines and its wavefront exhibits a zigzag shape as drawn with an angle to the dislocation lines of about 67°. In (b) the single line areas exhibit spin spirals of various periods. Their wavefronts are tilted by about $\pm 62°$ with respect to the dislocation lines. The application of an out-of-plane magnetic field leads to the formation of skyrmions in the double line areas (c-d) and in the single line areas to 360° walls (e-g). Measurement parameters: out-of-plane magnetic fields as marked, (a) $U = 700\,\mathrm{mV}$, $I = 750\,\mathrm{pA}$, $T = 4\,\mathrm{K}$; (b-d) $U = 700\,\mathrm{mV}$, $I = 1\,\mathrm{nA}$, $T = 8\,\mathrm{K}$; (e-g) $U = 500\,\mathrm{mV}$, $I = 1\,\mathrm{nA}$, $T = 4\,\mathrm{K}$. (a,b,e-g) Figures adapted with permission from Ref. [101]. Copyrighted by the American Physical Society. (c-d) Reprinted by permission from Macmillan Publishers Ltd: Nature Nanotechnology [23], copyright (2016).

proven that the spin spiral in the double line areas is cycloidal in nature [23], this is only expected for the single line areas due to the presence of the same interface-induced DMI [14]. Another difference between both line structures lies in their response to an external magnetic field. The spin spirals in the single line areas transform into an arrangement of single 360° domain walls which vanish one at a time for magnetic fields between 1 and 2 T. This can be observed in the spin-resolved constant-current maps of a field sweep in figures 4.4 e-g. Figures 4.4 c and d show that the spin spirals in the double line areas change into single skyrmions that can survive up to higher fields, i. e. 3 T, than the domain walls in the single line areas [23]. The skyrmions are bean-shaped and thus strongly anisotropic due to the structure of the double line area to which they are tied. Their shape is determined by the Fe

atom arrangement which changes its growth direction after every dislocation line leading to the known zigzag shape. Here, the skyrmion always reaches across three dislocation lines.

4.3 Bilayer of Pd/Fe on Ir(111)

All results shown here were already mentioned in [22, 69] and so the following section is based on these publications.

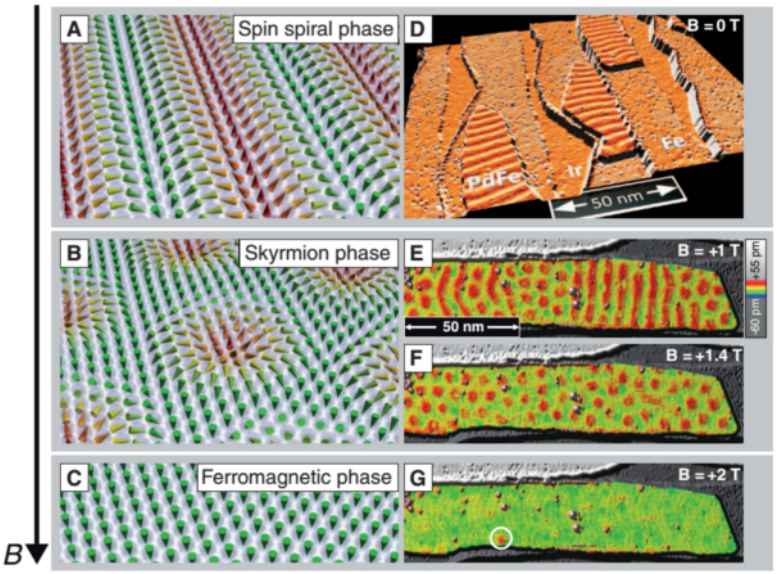

Figure 4.5: (A to C) Perspective sketches of the magnetic phases. (D) Overview SP-STM image, perspective view of constant-current image colorized with its derivative. (E to G) Pd/Fe bilayer at different magnetic fields ($U = +50\,\mathrm{mV}$, $I = 0.2\,\mathrm{nA}$, magnetically out-of-plane sensitive tip). (E) Coexistence of spin spiral and skyrmion phase. (F) Pure skyrmion phase. (G) Ferromagnetic phase. A remaining skyrmion is marked by the white circle. From [22]. Reprinted with permission from AAAS.

A Pd deposition on top of the pseudomorphically grown Fe ML on Ir(111) results in a bilayer of Pd/Fe on Ir(111). The Pd grows at the lower step edge of the Fe film, that itself grew at the lower step edge of the Ir(111), or as either hcp- or fcc-stacked islands on top of the atomic Fe layer, see figure 4.5. SP-STM measurements in figure 4.5 D revealed that the bilayer exhibits a spin spiral as ground state with period lengths of about 6 to 7 nm. This is attributed to the competition between Heisenberg exchange and DMI [22, 102, 103]. The application of a magnetic out-of-plane field leads to a phase transition from the spin spiral phase to a hexagonal, skyrmionic lattice phase, see figure 4.5 F. For higher magnetic fields another transition to the ferromagnetic phase takes place, see figure 4.5 G. However, the observed phases at different fields do not necessarily relate to the state of lowest energy as the system was kept at 4.2 K and thus the system is not able to relax into the new state of lowest

energy. For this reason, mixed phases of 360°-wall fragments and skyrmions, see figure 4.5 E, as well as single skyrmions surrounded by FM-like areas can be observed, see white circle in figure 4.5 G. The skyrmions can be written and deleted via an injected current from the SP-STM tip for fields close to the transition field between the skyrmion lattice phase and the ferromagnetic phase. The study identifies the energy of the injected electrons as the dominant factor concerning the switching rate. In STM the energy of the injected electrons is determined by the bias voltage that is used during the scan. Furthermore, the atomic defects of the Pd/Fe bilayer show a tendency to serve as pinning and nucleation centers [22].

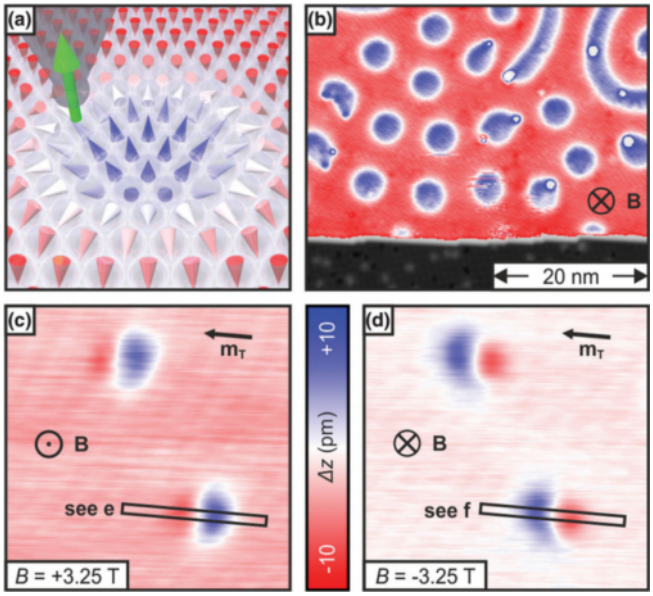

Figure 4.6: (a) Sketch of the experimental setup of a spin-polarized STM tip probing a magnetic skyrmion. (b) Topographic constant-current SP-STM image measured with out-of-plane sensitive magnetic tip; each blue circular entity is a skyrmion ($U = +200\,\mathrm{mV}$, $I = 1\,\mathrm{nA}$, $T = 2.2\,\mathrm{K}$, $B = 1.5\,\mathrm{T}$). (c) Magnetic signal of two skyrmions measured with an in-plane magnetization of the tip revealing a two-lobe structure ($U = +250\,\mathrm{mV}$, $I = 1\,\mathrm{nA}$, $T = 4.2\,\mathrm{K}$). (d) Same area as in (c) with inverted magnetic field; due to the preserved rotational sense, the contrast is inverted. Figure adapted with permission from Ref. [69]. Copyrighted by the American Physical Society.

In the second study using SP-STM [69] the skyrmions of the Pd/Fe bilayer were found to be circular in shape, see figure 4.6 b. This can be explained if the spin structure of the skyrmion is arranged as sketched in figure 4.6 a and the tip is magnetically sensitive to the out-of-plane direction. The cycloidal nature of the skyrmion in the sketch is only an assumption based on the symmetry selection rules of the DMI [10, 104]. The experimental proof for the cycloidal structure is missing. Figures 4.6 c and d reveal that an in-plane sensitive tip yields a different appearance of the skyrmion consisting of two lobes exhibiting a maximum and a minimum in the magnetic signal, respectively. The orientation and order of those two lobes is always the same which indicates a unique rotational sense of the magnetization. The result is corroborated by the response to an inversion of the magnetic field. This

leads, due to the stable tip's magnetic moment, to an inversion of the magnetic contrast including the lobes of the skyrmion; compare figures 4.6 c and d. However, the actual rotational sense cannot be determined by the reported experiment, since there is no way of determining the absolute orientation of the tip's magnetic moment.

4.3.1 NCMR in Pd/Fe/Ir(111)

This system exhibits non-collinear magnetoresistance (NCMR) which leads to a change in the LDOS and consequently in the measured dI/dV signal depending on the non-collinearity of the investigated area. For this reason, spatially resolved NCMR mapping enables STM to investigate changes of a sample's magnetic non-collinearity. All the findings presented here are taken from [105, 106].

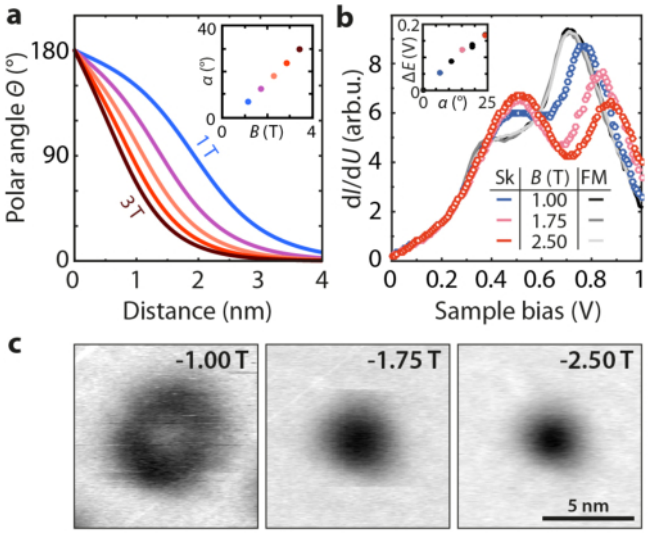

Figure 4.7: (a) Skyrmion profiles for different magnetic field values, plotted as polar angle θ from the surface normal of the magnetization versus distance from the skyrmion centre (obtained from fits to spin-polarized STM measurements [69]). Inset: evolution of the angle between a central spin of a skyrmion and its neighbours, α_c, with the external magnetic field B. (b) dI/dU tunnel spectra measured with a W tip in the centre and outside (FM) of an individual skyrmion at different magnetic field values ($T = 8$ K; stabilization parameters $U = 0.3$ V, $I = 0.2$ nA). Inset: evolution of the energy shift of the high-energy peak with respect to the FM state, ΔE, as a function of the angle between spins in the centre of the skyrmion, α_c (see the inset in a for the relation between α_c and B). (c) Corresponding laterally resolved dI/dU maps ($U = +0.7$ V, $I = 1$ nA, $T = 8$ K). Reprinted by permission from Macmillan Publishers Ltd: Nature Nanotechnology [105], copyright (2015).

C. Hanneken investigated skyrmions with spin-averaging STM in the Pd islands on Fe/Ir(111) and found that skyrmions appear as circular depressions in the dI/dV signal with different dI/dV spectra at their center and at the surrounding FM area. While tunneling anisotropic magnetoresistance (TAMR) can lead to magnetic contrast with a non-magnetic STM tip, it cannot explain the different dI/dV spectra at the skyrmion center and at the surrounding FM area as TAMR contrast has to be identical

for collinear orientations of the magnetic moments. This proved that neither TMR nor TAMR [107] can explain the observations and a new effect, i. e. NCMR, is necessary to explain the results. For increasing out-of-plane fields the skyrmions shrink in size and so does the observed circular object until it transforms into a dot-like depression, see figure 4.7 c. With the field also the non-collinearity of the skyrmion increases which means that the nearest-neighbor angles between the magnetic moments increase. In figure 4.7 a the polar angle of the skyrmion's magnetic moments relative to the external magnetic field is shown against the distance from the skyrmion center. The angle is derived from fits to SP-STM measurements [69]. The maximum change of the polar angle appears at the in-plane orientation of the magnetic moments and moves towards the center of the skyrmion with increasing magnetic fields. Thus, the observed shrink of the circular object is not only due to the actual size shrink but also caused by the lateral shift of the maximum in change of the polar angle. Without the lateral shift of the polar angle change maximum and the dependence of the contrast on the local non-collinearity of the magnetic moments, the skyrmions would appear as circles with decreasing diameters. The inset of figure 4.7 a shows the polar angle between the central magnetic moment and its neighbors α_c versus the applied out-of-plane field, which demonstrates that the nearest-neighbor angles and so the non-collinearity of the skyrmion increases linearly with the field. At the same time the steep peak in the dI/dV spectra taken at the skyrmion center in figure 4.7 b shifts in voltage roughly linearly with α_c (see inset). In contrast, the same peak that the FM surroundings exhibit stays unaltered. All these experimental results suggest that the observed contrast scales roughly with the nearest-neighbor angle between magnetic moments of the investigated area. This is not only the case for the skyrmions but also for the spin spirals (see supplement of [105]). Figure 4.8 a shows a spin-averaged differential conductance map of the Pd/Fe bilayer in zero field. A stripe pattern is visible as expected for a spin spiral but it exhibits half the period length (about 3 nm) compared to the contrast with SP-STM. The dI/dV spectra of figure 4.8 c were taken in the ferromagnetic phase, at a maximum and at a minimum of the dI/dV signal in the spin spiral. The spectra show the same trend as was observed for the skyrmion center in increasing external magnetic fields in figure 4.7 b. Therefore, the transition from the FM phase to the minimum of the spin spiral corresponds to an increase of non-collinearity. In zero field an increase of the non-collinearity cannot arise from an external magnetic field but is induced by the magnetocrystalline anisotropy of the bilayer [102, 103]. The uniaxial out-of-plane anisotropy leads to a preference of the magnetic moments for the out-of-plane orientation and so to a periodic oscillation of the nearest-neighbor angle along the propagation direction of the spin spiral. In summary, the observed NCMR contrast of spin spirals in a system with uniaxial anisotropy consists in stripe patterns with half the magnetic period length.

All changes of non-collinearity in the Pd/Fe bilayer can be investigated with non-magnetic STM and magnetic fields. Moreover, Hanneken's experiments showed that for the bilayer of Pd/Fe an increasing local non-collinearity leads to a reduction of the dI/dV signal in STM on the same order as observed for TMR. Thus, the reduction of the dI/dV signal observed by a non-magnetic STM tip can be attributed to an increase of the sample's magnetic non-collinearity, which will be exploited in this thesis.

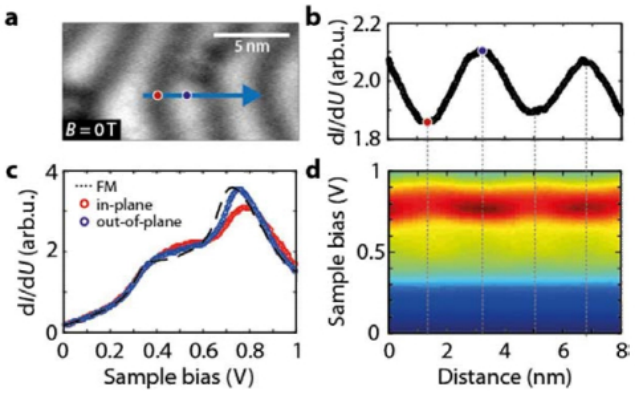

Figure 4.8: (a) Map of differential conductance (B = 0 T, U = +0.7 V, I = 1 nA, T = 4 K, Cr bulk tip found to be non-polarized. (b) Profile along the blue arrow shown in (a), the period corresponds to half of the magnetic period. (c) dI/dU tunnel spectra at a maximal (blue, out-of-plane magnetization) and minimal (red, in-plane magnetization) dI/dU signal of the spin spiral, in comparison to the FM spectrum taken at B = -2.5 T (black) (T = 4 K, stabilization parameters U = -1 V, I = 1 nA). (d) Spatially and energy resolved dI/dU signal. Reprinted by permission from Macmillan Publishers Ltd: Nature Nanotechnology [105], copyright (2015).

Chapter 5
5 Experimental results

Within this chapter I present all the conducted experiments and their results. These were all done in the described STM system and were therefore taken at 4.7 K unless stated otherwise. The experiments can be divided into two parts. The aim of the first part was to find the sense of magnetization rotation of already known systems, whereas the second part deals with new systems for which the results are more general.

5.1 Double layer of Fe on Ir(111)

5.1.1 Sense of magnetization rotation

Previous studies proved that the reconstructed parts of the Fe-DL do not change their magnetic phase for out-of-plane fields up to 9 T [99]. Therefore, I expect a negligible response of the magnetic moments in the Fe-DL to external fields. Hence, a field-dependent tip magnetization is necessary for an investigation of the magnetization rotation in the reconstructed areas of the Fe-DL via SP-STM. Here, I used an Fe-coated W-tip. The magnetic moment of this tip can be reoriented by external magnetic fields. This will result in images of the same magnetic structure but different magnetic contrast revealing all components of the magnetization in the sample, similar to the results in [32, 33]. In the following experiment I scanned two separate areas of the Fe-DL with the same tip in three different magnetic fields.

Figures 5.1 a and b show a sample that exhibits the DL and TL of Fe on Ir(111) in two different magnetic fields as marked in the figure. In both Fe layers the known magnetic contrast of spin spirals is visible as a periodic change in the dI/dV signal resulting in a wave pattern. In an out-of-plane field of 0.6 T the amplitude in the dI/dV signal is similarly large for all spin spiral propagation directions. In contrast, the amplitude of spin spirals that propagate non-collinear to the in-plane field is strongly reduced in the in-plane field of 1 T. For an example, see the area in figure 5.1 b marked by a blue, dotted rectangle. This indicates that the magnetic moment of the tip follows the external field. As a consequence, the SP-STM tip sensitivity changes to different components of the sample's magnetization depending on the orientation of the external magnetic field.

In figure 5.1 I show detailed maps of (c-e) the differential tunneling conductance, (f) the topography and (g) the current for the reconstructed area of the Fe-DL highlighted in (b) by a red rectangle in magnetic fields as marked. The maps of the dI/dV signal reveal a zigzag-like wavefront pattern of the spin spirals with a period length of 1.8 nm. Furthermore, the topography exhibits one of the two kinds

of dislocation lines. Neither the period length nor the propagation direction of the spin spiral changes in different fields. However, the position of the wave pattern relative to stationary defects changes for a reorientation of the external magnetic field. To identify the positions relative to the defects I mapped the exact position of the defects from the respective current map, see figure 5.1 g, onto the corresponding dI/dV map. A comparison of the dI/dV maps in different fields reveals that the contrast inverts for the inversion of the magnetic field and field rotations by $\frac{\pi}{2}$ lead to translations in the SP-STM contrast pattern of about $\frac{\lambda}{4}$.

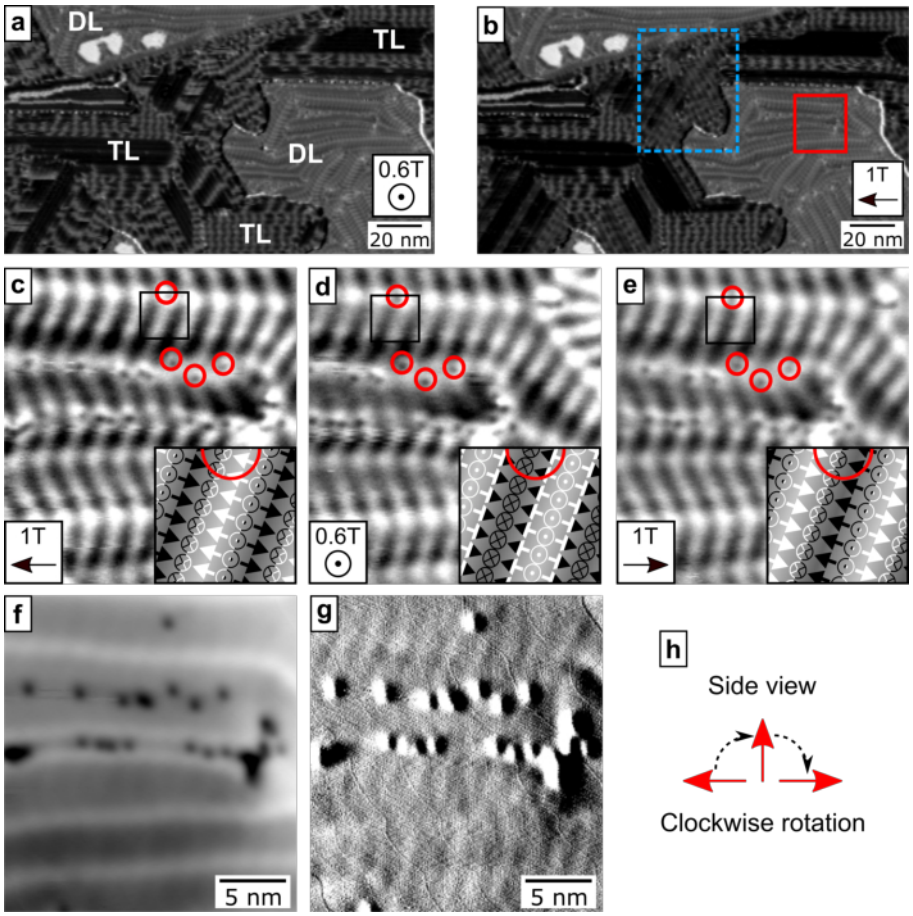

Figure 5.1: (a,b) Maps of the differential tunneling conductance showing the DL and TL of Fe on Ir(111) in a magnetic field as marked taken with an Fe-coated W-tip. (c-g) are detailed dI/dV (c-e), topography (f) and current (g) maps of the area marked by a red rectangle in (b) in magnetic fields as marked. The insets in (c-e) illustrate the sample's magnetic structure relative to a defect in the marked areas with the colors matching the contrast. The orientation of the spin spiral to the defect for (d,e) was taken from (c) and thus corresponds to the expected contrast for (d,e). (h) Illustration of the experimentally determined sense of magnetization rotation. (Measurement parameters: V = -0.7 V, I = 1 nA, T = 4.7 K)

The observed translations in SP-STM contrast result from the reorientation of the tip's magnetic moment by the external magnetic field. Hence, an inversion of the magnetic field leads to an inversion of

the tip's magnetization orientation and consequently to the observed inversion of the SP-STM contrast. The tip's magnetic moment also follows the field rotations by $\frac{\pi}{2}$ resulting in the measured translations in SP-STM contrast by about $\frac{\lambda}{4}$. For the purpose of clarity, I highlighted a small area around a defect in figures 5.1 c-e and illustrated the corresponding spin spiral configuration as well as the defect in the inset. I oriented the spin spiral relative to the defect based on the map in figure 5.1 c. Hence, the insets in figures 5.1 d and e correspond to the expected contrast. Since Fe-coated W-tips have an in-plane anisotropy their magnetic moment will not completely align with the external out-of-plane field. As a consequence, the corresponding translation in contrast does not exactly match $\frac{\lambda}{4}$, compare figure 5.1 d and its inset. The association of the dI/dV signal maxima with a collinear orientation of the tip's and the sample's magnetic moment leads to the conclusion that the system exhibits a clockwise sense of magnetization if seen from left to right, see figure 5.1 h. Whether the magnetic signal exhibits a maximum or a minimum for the parallel relative orientation of the sample's and tip's magnetic moments is irrelevant since both possibilities lead to the same rotational sense. A scan in an in-plane and an out-of-plane field would already be sufficient for the determination of the magnetization rotation. The map in the third field orientation only corroborates the results of the other two field orientations. Furthermore, I found the same results in an independent second area, see figure 5.2.

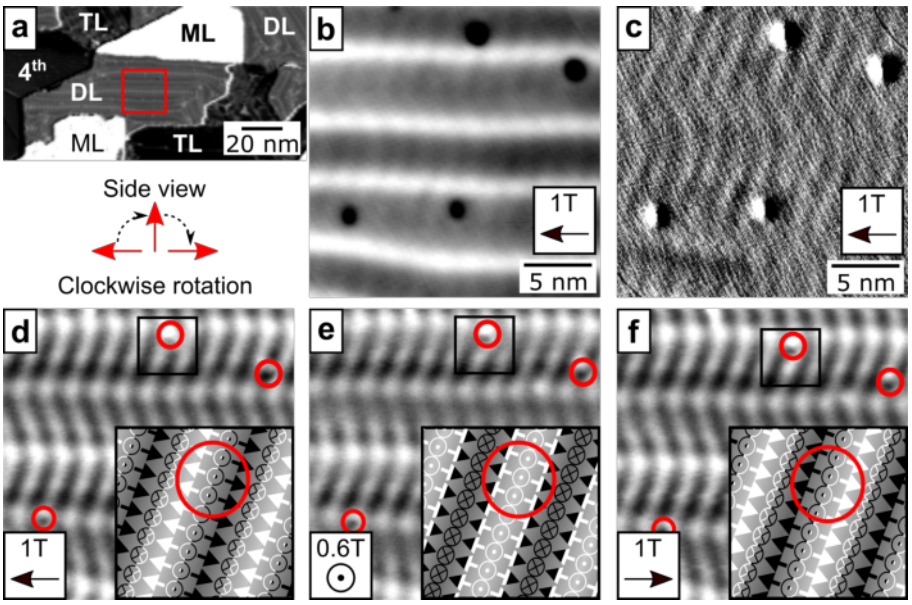

Figure 5.2: (a) Map of the differential tunneling conductance taken with an Fe-coated W-tip showing the first four layers of Fe on Ir(111) in a magnetic field as marked in (d); and an illustration of the experimentally determined sense of magnetization rotation. (b-f) are detailed topography (b), current (c) and dI/dV (d-f) maps of the area marked by a red rectangle in (a) in magnetic fields as marked. The insets in (d-f) illustrate the sample's magnetic structure relative to a defect in the marked areas with the colors matching the contrast. The orientation of the spin spiral to the defect for (e,f) was taken from (d) and thus corresponds to the expected contrast for (e,f). (Measurement parameters: V = -0.7 V, I = 1 nA, T = 4.7 K)

While the Fe-DL itself does not respond to external magnetic fields, its magnetism can be influenced by defects and surrounding higher Fe layers that change their magnetism in the applied magnetic fields. Spin spirals in the Fe-DL areas next to Fe-TL exhibit translations after field changes corresponding to sudden jumps of the zigzag-pattern during scanning. Large defects distort the surrounding spin spirals. Both effects can lead to a wrong interpretation of the observed spin spiral contrast. Hence, I took care to only use Fe-DL areas that are not influenced by neighboring Fe-TL and lack large defects to determine the sense of magnetization rotation. I can rule out that the observed translations in contrast are actual changes in the magnetism of the sample caused by a coupling to the change in magnetism of neighboring higher Fe layers with the following consideration. If the magnetic moments in the spin spirals significantly change their orientation, the corresponding translation in SP-STM contrast will be different compared to the case for magnetic moments with an effectively fixed orientation. For the case of coupling to the higher Fe layer I expect random changes of the spin spiral's position relative to defects. Therefore, the probability that the observed result is a coincidence can be estimated by attributing the same probability to shifts by $\frac{\lambda}{4}$ in an arbitrary direction, a contrast inversion or no change for every field rotation by $\frac{\pi}{2}$. The likelihood to coincidentally observe the change in contrast that corresponds to the change expected for a fixed magnetization for two subsequent field rotations by $\frac{\pi}{2}$ in the same direction is $\frac{1}{16}$. For two areas the likelihood that the observed changes in contrast are a coincidence reduces to about 0.4 %. Hence, the observed change in contrast is a systematic change caused by the reorientation of the tip's magnetic moment and a fixed magnetism in the sample.
In summary, I determined the sense of magnetization rotation in the reconstructed areas of the Fe-DL in two independent areas. To do so I exploited the negligible response of the magnetic moments in the Fe-DL to external magnetic fields by scanning it with a field-dependent SP-STM tip in differently oriented fields. The tip's magnetic moment followed the external field resulting in scans with different contrast of the same magnetic structure. These changes of the spin spirals' contrast relative to stationary defects allowed me to determine the clockwise sense of magnetization rotation.

5.2 Triple layer of Fe on Ir(111)

5.2.1 Response to magnetic in-plane fields

As a first step in my investigations of the Fe-TL I subjected a sample that exhibits both kinds of Fe-TL dislocation line areas to a magnetic in-plane field of 1 T. For this purpose, I used a Cr-bulk tip, which is field-independent, to exclusively measure the change of the sample's magnetization.
Figure 5.3 a shows a differential tunneling conductance map of an area exhibiting the DL, TL and the fourth layer of Fe. In the DL and the TL the characteristic magnetic structures are visible. In case of the TL, both kinds of dislocation line areas with various period lengths and different dI/dV signal strengths can be seen in the dI/dV map. The application of a magnetic in-plane field of 1 T as marked in figure 5.3 b leads to a change of the magnetism in all Fe-TL areas. Some of the spin spirals in the

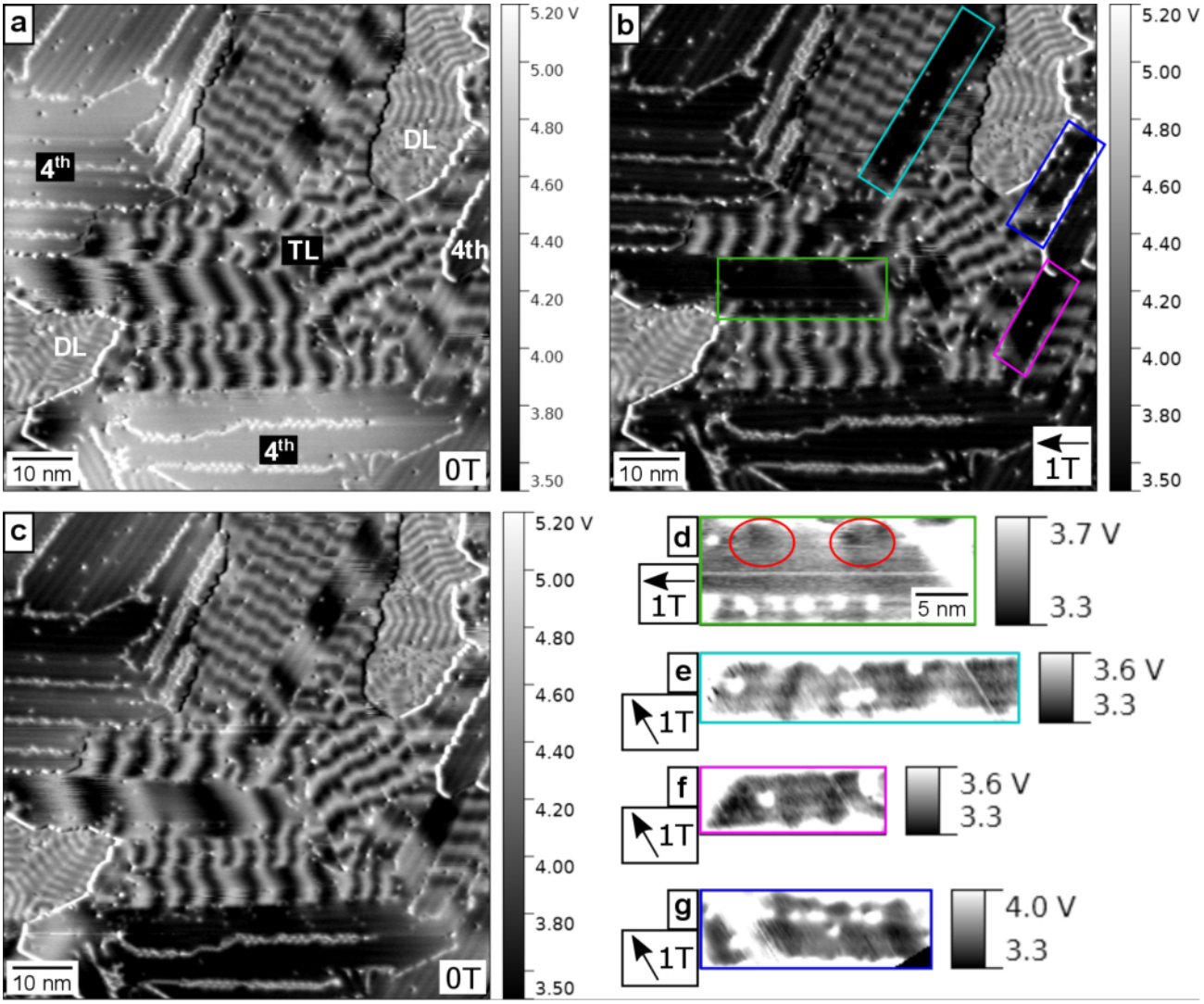

Figure 5.3: (a-c) Maps of the differential tunneling conductance showing spin spirals of various period lengths in the DL and the TL of Fe on Ir(111) taken with a Cr tip. (a) shows the ground state, (b) the sample after application of 1 T as marked and (c) shows the sample after the field has been reduced to zero again. (d-g) present areas marked in (b) by colored rectangles with individually adjusted color scales and the marked field orientations. In (d) red ellipses mark stripes, which correspond to a distorted spin spiral contrast that vanished during the scanning process. (Measurement parameters: V = -0.7 V, I = 1 nA, T = 4.7 K)

DL experienced a translation relative to local defects due to coupling to the surrounding Fe-TL. At the same time, the fourth layer shows a uniform dI/dV signal which corresponds to a complete polarization by the external field. A similar behavior is shown by some of the TL's single line areas with longer periods. The modulation of the dI/dV signal vanished in the color scale of figure 5.3 b; the dI/dV signal is reduced to the lower threshold value of the same areas in zero field. However, maps

with individually adjusted color scales show that distorted spin spirals, see figures 5.2 (e-g), still exist or (d) existed and vanished in the scanning process as marked by red ellipses. Single line areas with shorter periods and the double line areas show only small or negligible changes of the dI/dV signal but contrast changes that correspond to translations as in section 5.1.1. The double line area at the top of figure 5.3 b shows a decreased dI/dV signal in one half of its zigzag-structure. A closer look at the structure reveals that the zig- and zag-parts exhibit a different width which leads to different magnetic parameters and thus explains the difference in dI/dV signal. After the field reduction to zero most of the changes to the magnetic structure are reversed, see figure 5.3 c. The fourth layer of Fe does not exhibit a uniform dI/dV signal anymore but it does not return to the virgin state. Furthermore, the spin spirals in the single line areas with long periods reappear within the color scale of figure 5.3 a and the dI/dV signal levels in the double line areas return to the virgin state level.
These observations can be explained by taking into account that the magnetic moments of the TL tilt towards the external field in varying degrees. This tilting depends on the parameters of the respective structure and the angle of the spin spiral propagation direction relative to the field. In later measurements I will exploit the DL's lack of response to external fields to determine the orientation of the tip's magnetic moment. The amplitude in the dI/dV signal of identical spin spirals with different propagation direction can be compared to learn about the orientation of the tip's magnetic moment, as the amplitude depends on the projection of the magnetic moments in the sample onto the tip's magnetic moment. See Appendix A for more details. Such a determination is here not possible as the necessary amount of three different orientations with the same dislocation line spacing and thus magnetic parameters are not available. Moreover, I cannot compare differently oriented TL areas as they all have a slightly different structure. The only safe assumption about the tip's magnetic moment is that it points roughly along the out-of-plane direction because the Fe-DL spin spiral contrast in all three possible in-plane directions exhibit a similar dI/dV signal magnitude. Therefore, I conclude that the vanishing contrast of the spin spirals in the single line areas results from the tilting of the magnetic moments into the plane and thus the transformation into strongly distorted spin spirals or a field-polarized FM state. A tilting also occurs for the other spin spirals but to a lesser extent. However, this interpretation cannot explain why only the higher threshold in the dI/dV signal changes with the field application. Instead, both a reduction of the higher and an increase of the lower threshold of the dI/dV signal is expected. This observation remains unexplained. The changes of the double line areas or the lack of it cannot be clearly explained due to the complexity of the sample. The differing behavior of the double line areas in the in-plane field can have several reasons. For example, system parameters like anisotropy or saturation magnetization can change with the different line spacing in the double line areas. Another reason for the differing behavior are the varying neighboring areas of different local coverage that exhibit different magnetization states.
To sum up, this experiment shows how the magnetic moments of the fourth and the third layer respond to a magnetic in-plane field. I found that the fourth layer and the TL single line areas with long period lengths strongly follow the external field. The fourth layer and few single line areas of the Fe-TL

become completely field-polarized. However, most of the spin spirals in the single line areas remain but distort to varying degrees. In order to find their sense of magnetization rotation I conduct scans in differently oriented magnetic fields via SP-STM with a field-independent tip in section 5.2.3. The double line areas show a mixed degree of tilting towards the external magnetic field which is small in comparison to the single line areas. Therefore, it is unclear if an STM tip with field-dependent or -independent magnetization orientation is best suited for determining the magnetization rotation of the double line areas. In the following sections I will try an approach involving a field-dependent tip like in section 5.1.1. Afterwards an investigation of the double line areas with a field-independent tip is shown in in section 5.2.3.

5.2.2 Investigations with an Fe-coated W-tip

Investigations of skyrmions in the double line areas with an Fe-coated W-tip

In the case of a significant magnetic anisotropy the magnetic moments will follow an external magnetic field only by a negligible tilting angle. Hence, different orientations of the tip's magnetic moment are necessary to image all three dimensions of the magnetic structure. Therefore, I decided to use an Fe-coated W-tip which exhibits a field-dependent orientation of its magnetic moment for an investigation of skyrmions in the Fe-TL's double line areas and canted magnetic fields.
Figure 5.4 shows topography maps of the Fe-TL double line areas with different growth directions in (a) an out-of-plane field of 1.5 T and (b) a field of 1.82 T that is canted by 31.7° relative to the surface normal. Single skyrmions that emerged from the zigzag-patterned spin spirals are visible for three orientations of the double line areas. However, the third direction of the double line areas, see area marked by the green ellipse in figure 5.4 b, exhibit many defects and is thus not considered for evaluation. While the skyrmions of two orientations show the same contrast for the out-of-plane field, they feature a distinct difference in the canted field. In figure 5.4 b the skyrmions show a different amplitude in the measured height depending on their orientation relative to the field's in-plane component. A comparison of line profiles through several skyrmions in the same propagation direction but different field reveals that for the direction collinear to the field's in-plane component neither the amplitude nor the shape changes, see figure 5.4 c. In contrast, the line profiles of the other propagation direction, see figure 5.4 d, shows that the amplitude of the skyrmions is reduced in the canted field from roughly 15 to 10 pm. The second line profile was not taken through the center of the skyrmions as there would have been too many defects that distort the local magnetic texture.
Besides the already discussed Fe-TL I also imaged a part of the Fe-DL which can be used to roughly determine the orientation of the tip's magnetic moment, see Appendix A. I find a polar angle of 18° from the surface normal for the tip's magnetic moment in the out-of-plane field. In the canted field the polar angle changes to 70°. The lack of a perfect alignment with the external magnetic field could be attributed either to the anisotropy of the tip that prefers an in-plane orientation [108] or to the measurement error which can result in an error of the polar angle determination of up to 14°, see Ap-

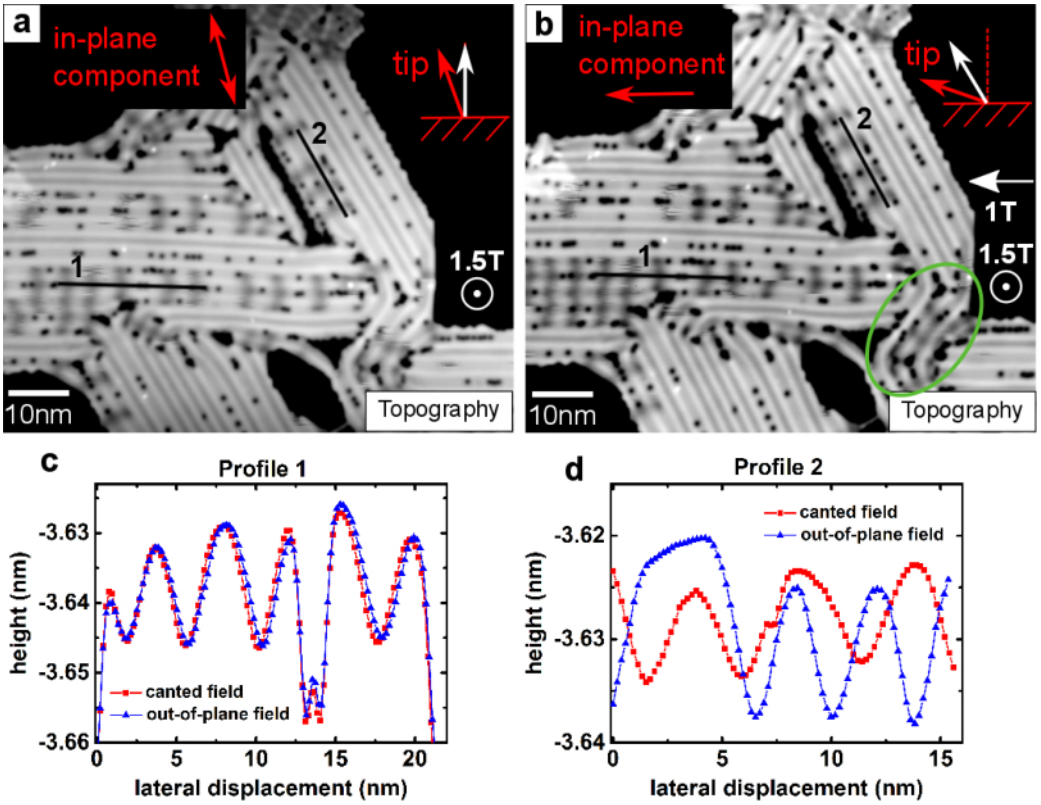

Figure 5.4: (a-b) Topography maps of double line areas in the Fe-TL taken with an Fe-coated W-tip in magnetic fields as marked in white. The in-plane and out-of-plane component orientations of the tip's magnetization are marked in red. In the illustration of the out-of-plane part the white arrows present the direction of the external field. In (b) a third propagation direction of skyrmions is marked with a green ellipse. (c-d) show line profiles along the respective direction of the double line areas at the same position in both external fields as marked in (a) and (b). (Measurement parameters: V = -0.7 V, I = 1 nA, T = 4.7 K)

pendix A. Furthermore, the in-plane component of the tip's magnetic moment aligns with the in-plane component of the canted field, as marked in figure 5.4 b. The in-plane component of the tip's magnetic moment in the out-of-plane field is irrelevant as the tip's magnetic moment points mostly in the out-of-plane direction. For this reason, the TMR contrast difference between skyrmions with different propagation directions is only a few percent. Such a small deviation is well below the measurement precision due to the defects in the sample that distort the spin texture. The reorientation of the magnetic moment proves that the tip responds to the external field even though the determined directions for the polar angle of the tip seem to deviate considerable from the applied field direction. If TMR is the dominant contrast mechanism, the contrast reduction of the skyrmions that are not aligned with the canted field's in-plane component is caused by the tilting of the tip's magnetic moment. Because of this I deduce from the absence of change in the skyrmion profile 1 in canted fields that the magnetic moments follow the external field in the same way the tip's magnetic moment does. This means that

a tilting of the sample's magnetic moments is unimpeded along the dislocation line direction but inhibited sideways to the dislocation line direction. This can be explained with a special anisotropy which consists of an in-plane hard axis that is perpendicular to the dislocation lines. If the magnetic moments of the skyrmions would not or only to a small degree follow the external field the line profile shape of a single skyrmion would change or at least move relative to defects. However, the experimental evidence excludes this alternative case. The lack of change in the profile shown in figure 5.4 c is also an indication against NCMR. For NCMR different field magnitudes are expected to result in a local increase or decrease of the skyrmion's non-collinearity and thus a changed amplitude. The only way to reconcile NCMR with this observation would be to claim that it compensates the change in TMR leading to an effectively unchanged height profile.
In summary, I found that the magnetic moments in the skyrmions can tilt freely along the dislocation lines in the double line areas of the Fe-TL. In contrast, the reduction of the SP-STM contrast for double line directions that are non-collinear to the field's in-plane component means that a tilting sideways to the dislocation lines is impeded. For this reason, the sense of magnetization rotation in the Fe-TL double line areas has to be determined either at lower fields with spin spirals, which follow the external field to a lesser extent, or by use of a field-independent tip.

Investigations of spin spirals in the double line areas with an Fe-coated W-tip

In the experiment presented in 5.1.1 I did not only investigate the Fe-DL but also the double line areas of the Fe-TL. Similar to the DL-Fe, I expected the spin spirals in the Fe-TL to respond to the external field only to a negligible extent. For this reason, the used Fe-coated W-tip is supposed to change the orientation of its magnetization resulting in translations in the SP-STM contrast depending on the angle of field rotation. Although this approach was not successful for the skyrmions it might be possible that the sample's magnetic moments respond less to the lower external field.
Figure 5.5 shows differential tunneling conductance maps of two different areas exhibiting spin spirals in the Fe-TL's double line areas in three different magnetic fields. The difference in the external fields is not only in the magnitude but also in the direction. Although I investigated six Fe-TL double line areas in total, I show only two series as they represent all the encountered responses. The top map of the first series in figure 5.5 a shows the zigzag-patterned spin spiral with several defects highlighted for the purpose of orientation. Below follows a map of the same area but in the inverted magnetic field which exhibits in most parts a contrast inversion, except on the right side which is marked by a green ellipse. Here, the contrast did not invert but shifted to a lesser extent. At the end of the up-scan, next to a step edge, a jump in the SP-STM contrast an be observed which implies a change of the actual magnetization. The result of this event is visible in the second scan in the inverted field which corresponds to the third map from the top. The contrast inverted completely indicating the same state as in the previous field, except for a small phase shift in the area marked by a green ellipse. In contrast, the spin spirals in figure 5.5 b do not expose any change after the field inversion. Only in

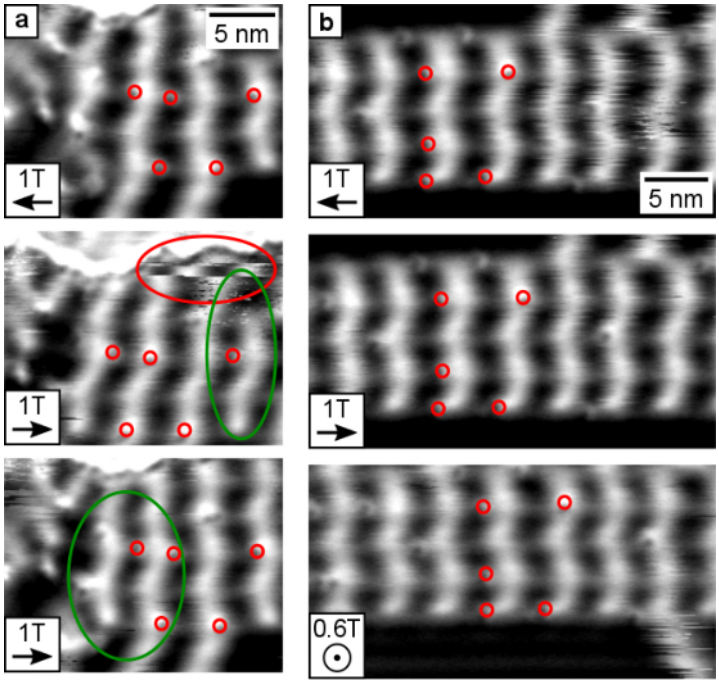

Figure 5.5: (a-b) Maps of the differential tunneling conductance in the Fe-TL's double line areas recorded with an Fe-coated W-tip in magnetic fields as marked. The red ellipse in the second image of series (a) highlights a jump in the magnetization that leads to a contrast inversion. The green ellipses mark parts with changes in contrast that deviate from the rest of the spin spiral. (Measurement parameters: V = -0.7 V, I = 1 nA, T = 4.7 K)

the out-of-plane field a small phase shift is visible in some parts of the image.
The observed non-systematic changes in SP-STM contrast and the jumps of the magnetization pattern in all six investigated areas lead to the conclusion that this approach is not suitable for finding the sense of magnetization rotation in the Fe-TL's double line areas. A determination of the magnetization rotation from these results would be misleading since I cannot know if the magnetization jumped or shifted between scans. Moreover, I cannot discern if the shifts and jumps in the magnetization are caused by a response of the magnetic moments to the external field or by the coupling to changes of the magnetization in neighboring areas. Therefore, the only remaining approach to determine the sense of magnetization rotation is an experiment involving a field-independent tip.

5.2.3 Sense of magnetization rotation

Within this section I study the Fe-TL using a field-independent tip, i. e. a Cr-bulk tip. Most of my investigations here were conducted on the Fe-TL's single line areas but I also present a single measurement on the double line structure. The idea of this experiment is to record the change of the magnetic structure that results from reorientations of the external magnetic field. Since the tip's magnetic moment is field-independent, any observed field response can be attributed to changes in the sample's magneti-

zation. The sense of the magnetization rotation can be determined by a comparison of the changes in the magnetic structures.

Determination via spin spirals

The single line areas of the Fe-TL exhibit spin spirals with a propagation direction that is tilted relative to the dislocation line direction and a period length that ranges between almost 6 nm and roughly 10 nm. For this experiment I chose the single line areas with period lengths at the upper end of the range, between 8.1 and 10.4 nm, because they revealed a strong response to external magnetic fields in section 5.2.1. I used comparably smaller fields of up to 0.5 T as they were already sufficient and larger fields might have led to a full polarization of the single line areas. In total I investigated three different single line areas with the same tip together with two Fe-DL's reconstructed areas to check for changes of the tip's magnetization. Furthermore, I performed another similar experiment which was carried out in the same way but only with one Fe-TL single line area and one reconstructed area of the Fe-DL. For the purpose of readability and brevity, the results of the second experiment are only shown in Appendix B as they lead to the same conclusion compared to the experiment discussed here.
Figure 5.6 a gives an overview of the sample via a 500 nm $\times$ 500 nm map of the differential tunneling conductance. The areas marked by red rectangles were used for the following analysis. For the determination of the tip's magnetization orientation an area of the Fe-DL had to be found that exhibits spin spirals propagating in three different directions in identically grown reconstructed areas. This is the case for three reconstructed areas that met in a single point and exhibit a star-like shape. For detailed results concerning the Fe-DL, see Appendix A. Close-up scans of the marked Fe-TL areas are displayed in the same figure. Each map shows first a spin spiral in zero field. They exhibit, from top to bottom, period lengths of 8.1, 10.4 and 8.8 nm. These spin spirals show signs of instability, e. g. small jumps of the magnetization, at an STM current of 1 nA and a bias voltage of -700 mV. The second map of each chosen Fe-TL area displays the magnetic state in a moderate out-of-plane field of 0.5 T revealing a break-down of the spin spirals into an irregular arrangement of 360° domain walls. These domain walls still show the same instabilities as the spin spirals. In figures 5.6 b and c the disappearance and appearance of single walls during scanning is observed and marked with red, dotted rectangles. This indicates that the system is metastable due to the high bias voltage applied to the sample. A comparison of the profile shapes in different fields for the TL area 3 is shown in figure 5.7 as an example. Similar presentations of the other two areas can be found in Appendix C. In this case, the line profiles were taken along the dislocation line direction instead of along the spin spiral propagation direction in order to guarantee that the profile is not distorted by topographic differences. The most striking observation is that the shape of the single domain walls in an external out-of-plane field is asymmetric, see the single domain wall profiles in figure 5.7 e marked by black rectangles. In this context, asymmetry has two meanings. On the one hand, the dI/dV signal level at the wall boundary does not start and end at either the maximum or minimum in dI/dV signal. This is a consequence of TMR contrast with

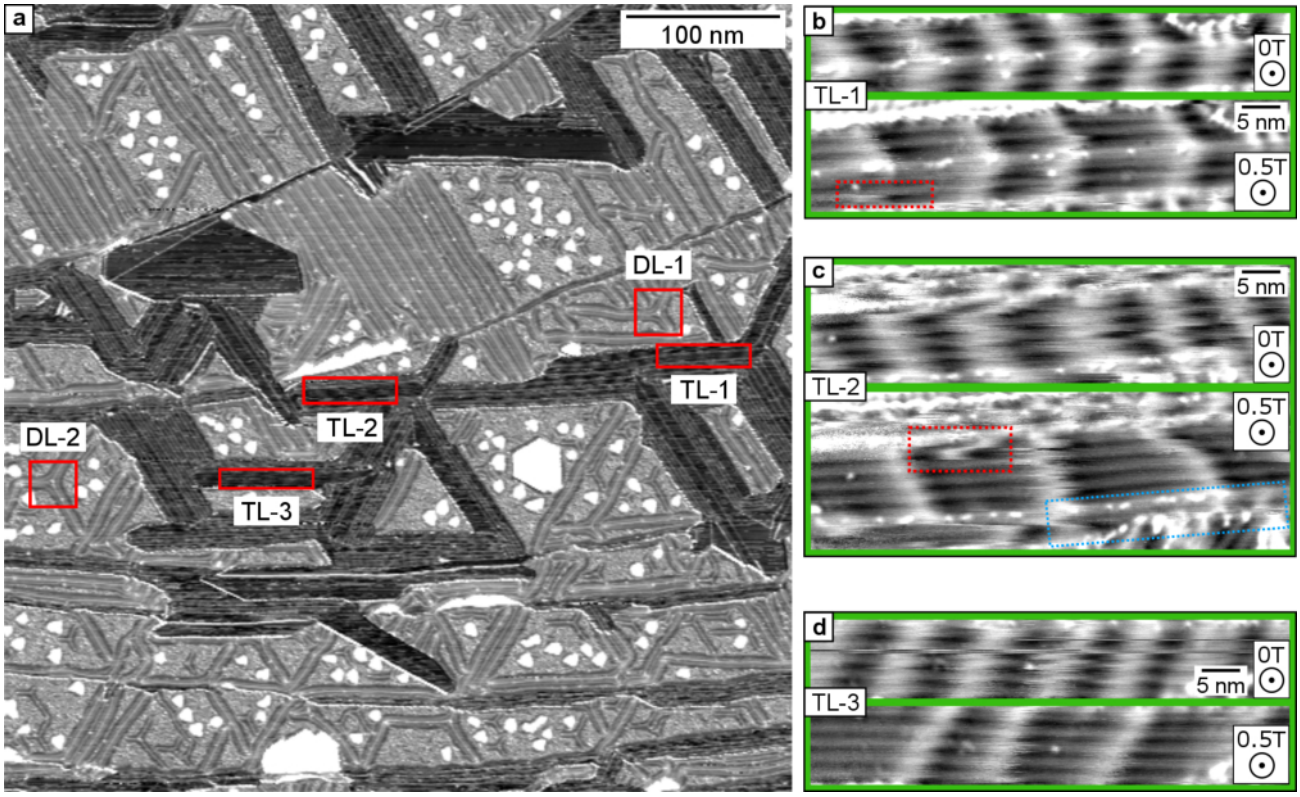

Figure 5.6: (a) Map of the differential tunneling conductance in the DL and the TL of Fe taken with a Cr-bulk tip in zero field. Each TL area marked in (a) by a red rectangle is displayed in (b-d) in a separate box consisting of a close-up scan in zero field and in an out-of-plane field of 0.5 T. Red dotted rectangles mark the appearance and vanishing of 360° domain walls during the scan in (b) and (c). The change of a neighboring structures is highlighted in (c) by a blue dotted rectangle. (Measurement parameters: V = -0.7 V, I = 1 nA, T = 4.7 K)

a canted magnetic moment of the SP-STM tip. The magnetic moments at the boundary of the 360° domain walls point parallel to the external field and thus their projection onto the canted magnetic moment of the tip lead to a an intermediate dI/dV signal level. This proves that TMR is the dominating contrast mechanism in this experiment because NCMR could not lead to such an asymmetric profile shape. On the other hand, the slopes in the dI/dV signal change due to the tilting of the magnetic moments towards the applied magnetic field and hence the shape of the profile becomes asymmetric. The shape of the profile changes with the orientation of the magnetic field and is more pronounced the larger the angle between field orientation and the tip's magnetic moment becomes, see figures 5.7 f and g. This finding proves that the magnetic moments respond to the external field as the tip state is field-independent. A single 360° domain wall is encased either by other single 360° domain walls or a plateau of an intermediate dI/dV value that corresponds to a collinear orientation of the magnetic moments. Despite the phase transformation the propagation direction and the amplitude of the walls in the dI/dV signal stay unaltered for all fields of the same magnitude but different orientation, com-

pare figure 5.7 e and g. Moreover, the line profiles show that the 360° domain walls keep the same or increase the distance between them relative to the corresponding parts in the spin spiral in zero field as expected for independent 360° domain walls. The constant amplitude in the dI/dV signal for all different field orientations proves that the magnetic structure is cycloidal in nature. In contrast, all the magnetic moments in a helical spin spiral would tilt with the same angle towards an external field along the propagation direction, see figure 2.1 c. This tilting would lead to different amplitudes in the dI/dV signal for TMR contrast depending on the angle between the tip's magnetic moment and the external field.

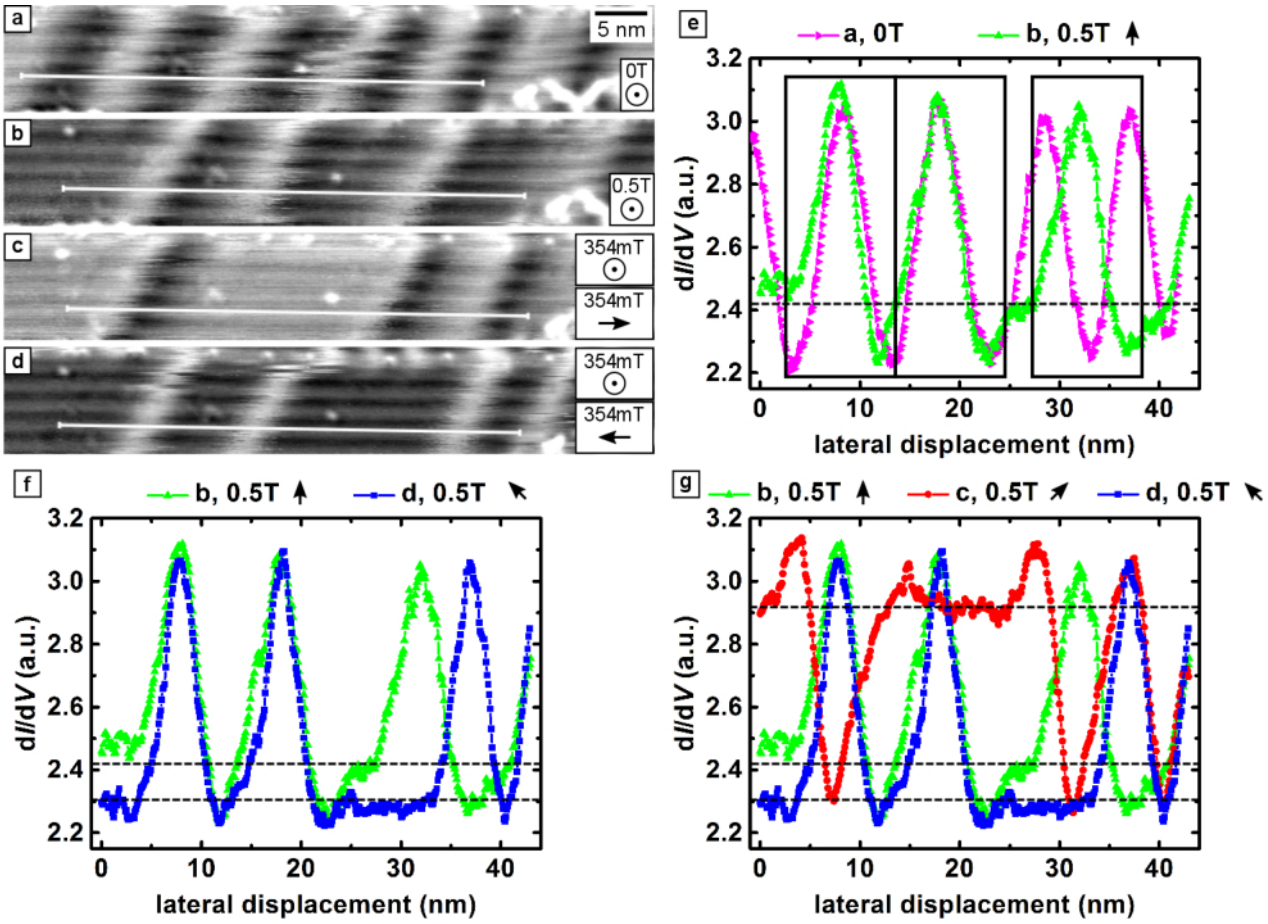

Figure 5.7: (a-d) dI/dV maps of the Fe-TL area 3 of figure 5.6 in (a) zero field, (b) an out-of-plane field of 0.5 T, (c) and (d) a field canted by 45° from the surface normal in both directions towards the double lines and a magnitude of 0.5 T. (e-g) show the line profiles of (a-d) for positions marked by white lines. The dotted horizontal lines indicate the dI/dV signal level at the boundary of the 360° domain walls for each applied external field. (Measurement parameters: V = -0.7 V, I = 1 nA, T = 4.7 K)

This kind of experiment enables me to determine the sense of magnetization rotation if the tip's magnetic moment is field-independent. An evaluation of the Fe-DL scans, that have been recorded alongside

with the Fe-TL data, leads to the conclusion that the tip's magnetic moment has a negligible field-dependence and stays, for the purpose of the experiment, unchanged. It has a polar angle of about 70° to the surface normal and the in-plane orientation is roughly collinear to the in-plane component of the rotated field. Therefore, the observed changes in the contrast are purely a result of the sample's response. For the detailed analysis of the Fe-DL maps see Appendix A. The sense of magnetization rotation can be deduced from scans of the same 360° domain walls in at least two different field orientations. In the next section I deduce the sense of magnetization rotation for one area as an example for all areas, since the data of the other areas leads to the same result.

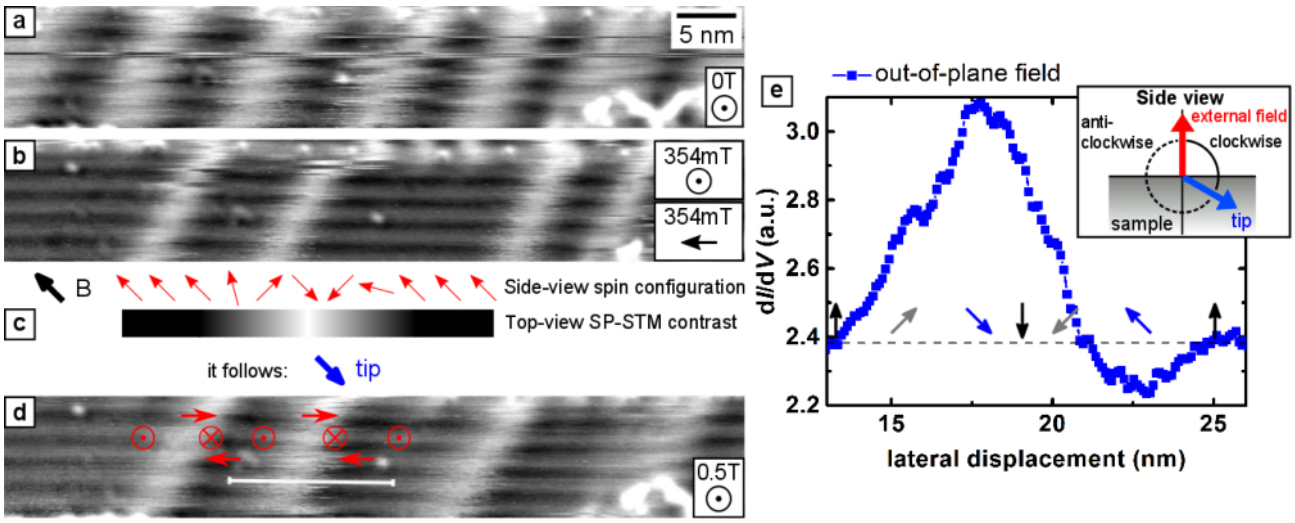

Figure 5.8: (a,b,d) Maps of the differential tunneling conductance in the Fe-TL's double line area 3 from figure 5.6 taken with a Cr-bulk tip in magnetic fields as marked. (c) An illustration showing a side view of the spin configuration of one 360° domain wall in (b) and below the corresponding contrast in the measurement based on the derived absolute orientation of the tip's magnetization marked in blue. (e) is a line profile taken from (d) with the corresponding orientation of the magnetic moments sketched into the profile. A dotted line indicates the dI/dV signal of the 360° domain wall boundaries. The white stripe in (d) marks at which position the profile shown in (e) has been taken. (Measurement parameters: V = -0.7 V, I = 1 nA, T = 4.7 K)

Figure 5.8 shows the Fe-TL area 3 from figure 5.6 but with an additional map for the second field orientation. In figure 5.8 b, I rotated the external magnetic field by 45° towards the double lines on the left side. The resulting contrast of the 360° walls looks most symmetric compared to the maps with other applied fields. In this case the tip's magnetization is most collinear to the applied field since the magnetic structure is symmetrically distorted by the field towards its direction, see sketch in figure 5.8 c. The areas surrounding the 360° domain walls exhibit a lower dI/dV signal level. Therefore, I conclude that the tip's magnetic moment is parallel to the center of the 360° walls and thereby roughly anti-parallel to the canted external field direction. The determined direction of the tip's magnetic moment can be used for interpreting the magnetic structure for the other field orientations. For this reason, I can associate the peaks and depressions of the 360° walls in figure 5.8 d with a parallel

and anti-parallel orientation of the magnetic moments in the sample relative to the tip's magnetization. Moreover, I can derive the orientation of the magnetic moments in the larger patches of intermediate dI/dV signal strength and between the peak and depression of the walls from the applied field as parallel and anti-parallel, respectively. I illustrated the deduced orientations of the magnetic moments in the sample in figure 5.8 d. For the sake of clarity, I present in figure 5.8 e a line profile taken from one of the 360° walls in figure 5.8 d which corresponds to a side view of the magnetic structure. I sketched the four derived orientations of the sample's magnetic moments at the corresponding lateral displacements in the wall. The black marked orientations are derived from the field's orientation and the blue arrows indicate the orientations concluded from the tip's magnetization. Finally, I conclude that single line areas of the Fe-TL exhibit a clockwise sense of magnetization rotation, seen from left to right. This is in line with the prediction that the rotational sense is determined by the DMI of the Fe/Ir interface [102, 103]. The other sense of magnetization rotation would manifest as reversal of the peak and depression order in all of the 360° walls. Under the assumption that the system does not have a unique sense of magnetization rotation both cases would have the same probability to occur, i. e. 0.5. In such a system, the likelihood of the coincidental observation of four areas (three areas in this experiment and a fourth area in the second experiment shown in Appendix B) with the same sense of magnetization rotation would be about 6 %.

Determination via skyrmions

The same approach I used to identify the sense of magnetization rotation in the single line areas in the previous section I also applied to skyrmions in the double line areas. Again, I exploit the change of a magnetic structure's profile in two differently oriented external magnetic fields to find the sense of magnetization rotation.

In the investigation of several double line areas I found one single skyrmion which is shown in figure 5.9. This skyrmion does not, as usual for this system, extend over three dislocation lines but only two. The sample was subjected to two different magnetic fields, an out-of-plane field of 1.64 T and a canted field of magnitude 1.92 T and a rotation of 31.4° towards the left side along the double lines. Instead of keeping the field at the same magnitude I added as much in-plane field as possible since in section 5.2.1 the skyrmions exhibited little or no change due to in-plane fields. In comparison to the previous experiment there is no change directly visible in the maps of the differential tunneling conductance. However, the profiles along the double lines through the center of the skyrmion reveal a difference both in the amplitude and the shape. While the amplitude reduced by the canting to roughly 87 % of the value in the out-of-plane field the shape transforms into an almost perfectly symmetric peak, see figure 5.9 e. Especially the current and height map reveal that not only a sharp defect is within a few nm of the skyrmion, but next to its lower part there is also a broad but flat elevation visible that might correspond to a defect in one of the deeper atomic layers.

The changes of the profile can be investigated in the same way as the changes in the double line

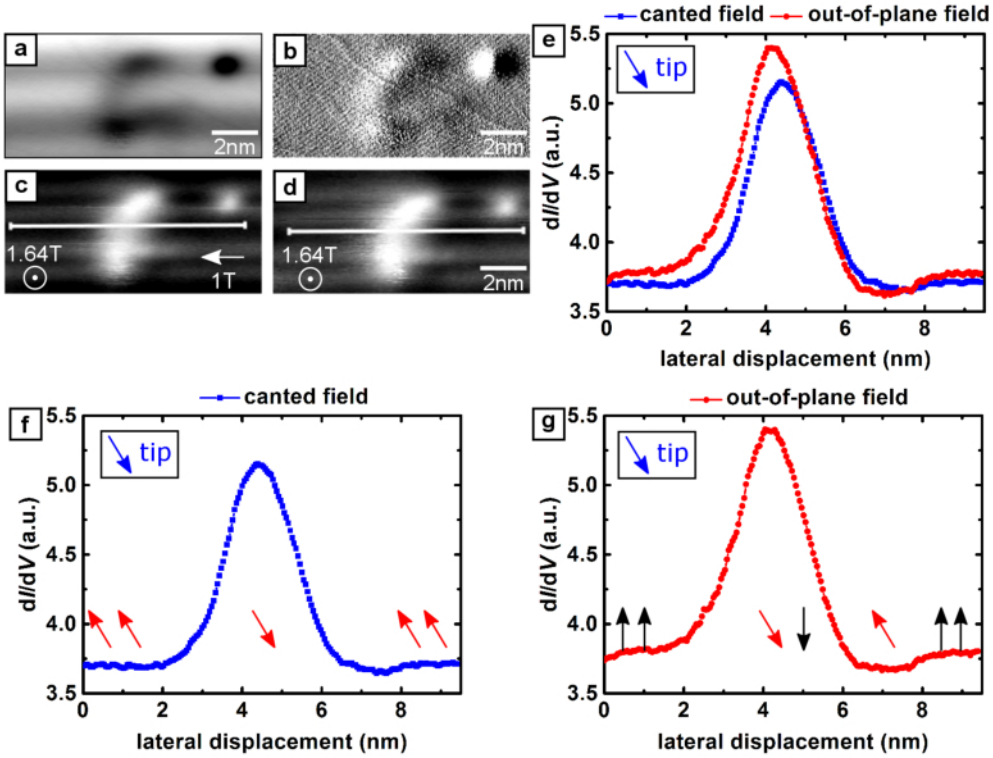

Figure 5.9: Maps of (a) height, (b) current and (c,d) differential tunneling conductance showing a single skyrmion in the Fe-TL's double line area at magnetic fields as indicated. (e-g) show line profiles through the skyrmion along the double line direction taken from (c) and (d), as marked by white lines. Within the profiles I sketched the orientation of the tip's magnetic moment and of the magnetic moments as derived from the profiles. (Measurement parameters: V = -0.7 V, I = 1 nA, T = 4.7 K)

areas with several differences to the former case which will be discussed later. Again, the symmetric profile in the canted field, see figure 5.9 f, reveals that the tip's magnetization is roughly anti-parallel to the applied field direction. This means that the peak and the depression in figure 5.9 g can be associated with the orientation of the magnetic moments in the sample that are parallel and anti-parallel to the tip's magnetic moment. Furthermore, the FM-like surrounding area has to be parallel to the out-of-plane field and the magnetic moments between the peak and the depression must be oriented anti-parallel to the external field. The concluded orientations of the magnetic moments are sketched in a side view and correspond to a clockwise sense of magnetization rotation if seen from left to right. However, there are several obstacles for such a straight-forward interpretation of the observations. At first, this interpretation assumes that TMR is the sole contrast mechanism which would fail here to explain why there is an amplitude difference for the different fields. Previous measurements established that NCMR can play a role in this system which can explain the amplitude change [23]. With increasing field the non-collinearity in the skyrmion increases which can lead to

a reduced dI/dV signal in the skyrmion. However, NCMR cannot explain the asymmetric shape of the profile in an out-of-plane field and thus cannot be the dominant contrast mechanism. Another explanation for the reduction of the amplitude with the canting of the field in figures 5.9 c and d would be a rotation of the tip's magnetization. However, the recorded Fe-DL maps do not indicate a tip change, see Appendix D. Furthermore, both defects have an unpredictable influence on the magnetic structure of the skyrmion. Thus, this single measurement is not sufficient and further measurements are necessary to conclude if this approach can yield the sense of magnetization rotation.

Summary

I determined the sense of magnetization rotation in the single line areas of the Fe-TL from the changes in the 360° wall profiles in different orientations of an external magnetic field. At first, I found the absolute orientation of the tip's magnetic moment from the comparison of the 360° wall profiles in different fields. The result was corroborated by maps of spin spirals in the Fe-DL which also assured that the tip state was field-independent. With this knowledge I was able to qualitatively deduce the full magnetic structure of the 360° wall resulting in the determination of the clockwise magnetization rotation. Furthermore, the lack of change in the amplitude of the 360° domain walls in the dI/dV signal for canted magnetic fields proves that the magnetic structure is cycloidal in nature. A similar approach to skyrmions in the double line areas revealed the same clockwise sense of magnetization rotation, seen from left to right, as in the single line areas. In the case of the double line areas the result bases on only one experiment that seems to be influenced by a crystal defect. Therefore, the results cannot be generalized unless further experiments reproduce the results.

5.2.4 Model of the magnetization in the triple layer of Fe

The profile shapes of the 360° domain walls, shown in figures 5.6 b-d and 5.7 e-g, can also be used to extract magnetic parameters. For this reason, I fit analytic expressions for 360° domain walls based on an isotropic and effectively one-dimensional model to the observed domain wall profiles. In the following paragraph I present the model and the resulting analytic expressions for independent 360° domain walls.

In order to fit the magnetization to an isotropic and effectively one-dimensional model, I neglect the anisotropic structure which leads to spatially inhomogeneous magnetic parameters and structures. An isotropic model cannot explain the tilting of the spin spiral propagation direction relative to the dislocation lines or the absence of skyrmions. Therefore, the proposed model can only be an approximation of the actual magnetic structure. A more accurate model would have to take the complex structure of the system into account. The identification and validation of a more accurate model is impossible without the help of *ab initio* calculations that are tailored for this system. I use the continuum approximation and restrict exchange interaction as well as DMI to nearest-neighbor terms. The anisotropy is covered by a uniaxial effective term that incorporates the local part of the dipolar energy while

non-local contributions are ignored [53]. As a consequence, the system's energy per unit area ϵ of the effectively one-dimensional magnetization can be described by a similar expression as in [53]:

$$\epsilon = \int_{-\infty}^{\infty} \mathrm{d}x \left(A \left(\frac{\partial \phi(x)}{\partial x} \right)^2 + D \frac{\partial \phi(x)}{\partial x} + K \sin^2(\phi(x)) - M_\mathrm{s} B \cos(\phi(x)) \right),$$

where A is the exchange stiffness, K the uniaxial effective anisotropy coefficient, D the DMI coefficient for a cycloidal spin configuration, M_s the saturation magnetization and B the external magnetic field. The orientation of the magnetic moments is described by $\phi(x)$ which is the angle of the magnetic moment to the surface normal at the position x. The magnetic structure that minimizes the energy also has to fulfill the Euler-Lagrange-equation. This leads to the following non-linear partial differential equation:

$$\frac{\partial^2 \phi(x)}{\partial x^2} = \frac{K}{A} \cos(\phi(x)) \sin(\phi(x)) + \frac{M_\mathrm{s} B}{2A} \sin(\phi(x)),$$

with the following solution for independent 360° domain walls included in [53, 54]:

$$\phi(x) = \begin{cases} 2 \arcsin \left(\tanh \left(\sqrt{\frac{M_\mathrm{s} B}{2A}} x \right) \right) + \theta, & \text{for } K = 0 \quad (5.1) \\ \arcsin \left(\tanh \left(\frac{x+c}{w} \right) \right) + \arcsin \left(\tanh \left(\frac{x-c}{w} \right) \right) + \theta, & \text{for } K \neq 0 \quad (5.2) \end{cases}$$

$$\text{with } c = \frac{w}{2} \left(\sqrt{\frac{2K}{M_\mathrm{s} B}} \right), w = \sqrt{\frac{A}{K + \frac{M_\mathrm{s} B}{2}}}$$

where θ is an offset angle that corresponds to the polar angle between external magnetic field and the tip's magnetization orientation in SP-STM. This solution describes the distribution of the magnetic moments' orientation within a 360° domain wall. If TMR is the only contrast mechanism, this expression can be fit to the profiles of the 360° domain walls in the Fe-TL's single line areas. The anisotropy-free fit ($K = 0$) reveals the ratio of M_s, B and A. In the same way the fit for $K \neq 0$ yields a ratio of M_s, B and K and a second ratio that involves M_s, B, K and A. Both fits reveal a complete set of magnetic parameters, if one of the parameters is estimated. For a pseudomorphic ML of Fe on Ir(111) *ab initio* calculations predict a magnetic moment of $2.7 \mu_\mathrm{B}$ per Fe-atom [102]. This magnetic moment corresponds to a M_s of 1.77 MA/m. For an increasing Fe layer thickness I expect M_s to approach the bulk bcc-Fe value of 1.73 MA/m [109], which is close to the ML value. Despite the possible changes of M_s caused by the non-pseudomorphic growth of the Fe-TL, I use the ML value as estimation for M_s. Combined with the period length λ_0 of the spin spiral in zero field I can derive the DMI constant D

from [7]:

$$\lambda = \begin{cases} 4\pi\frac{A}{D}, & \text{for } K = 0 \quad (5.3) \\ \frac{A}{D}\int_0^{2\pi} \mathrm{d}\theta \left(\beta \sin^2(\theta) + C\right)^{-0.5} & \text{for } K \neq 0 \quad (5.4) \end{cases}$$

$$\text{with } \frac{\pi}{2} = \int_0^{\pi} \mathrm{d}\theta \left(\beta \sin^2(\theta) + C\right)^{0.5}, \beta = \frac{AK}{D^2} \quad (5.5)$$

where C is an integration constant that can be determined with equation 5.5.

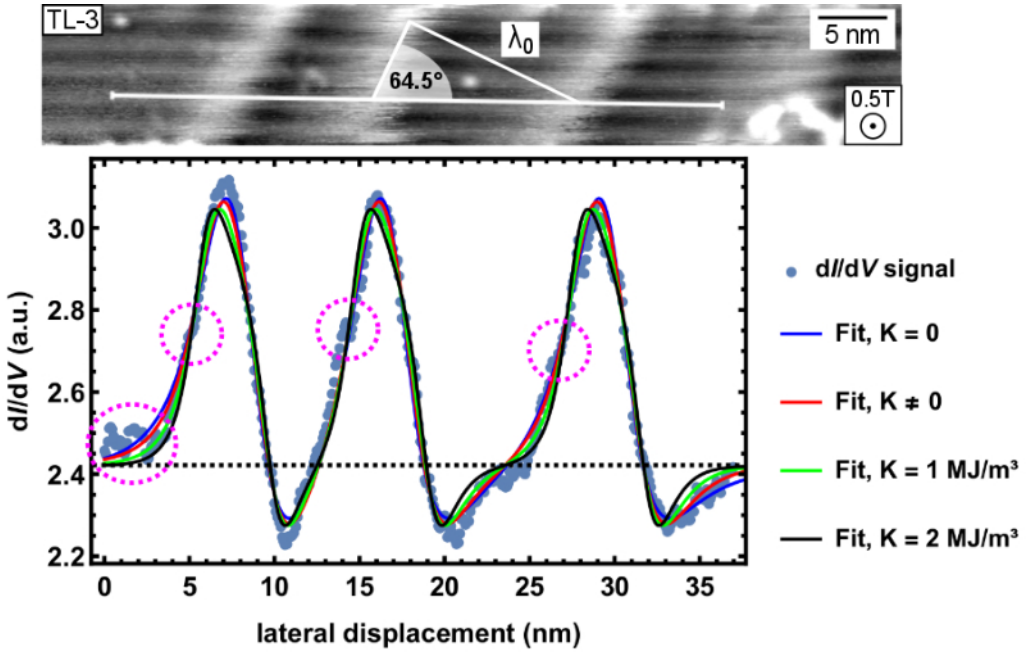

Figure 5.10: Differential tunneling conductance map of the Fe-TL area 3 in magnetic field as marked, already shown in figure 5.6. The period length λ_0 is drawn with the angle of the wavefronts relative to the dislocation lines. A white line marks the position of the following line profile in the dI/dV map. The line profile is presented, including 360°-wall-fits with varying effective uniaxial anisotropy. Magenta-colored circles indicate systematic errors in the profiles due to movement of the 360°-walls or defects.

Figure 5.10 shows the fits for $K = 0$, $K \neq 0$ and with fixed K as marked in an out-of-plane field of 0.5 T for the Fe-TL area 3. A dotted horizontal line indicates the dI/dV signal level of the surroundings which have their magnetic moments oriented parallel to the external field. The fits for the other two areas in the same magnetic field are presented in the extra figures 5.11 and 5.12. Additional fits with a fixed anisotropy are incorporated to demonstrate how larger anisotropies fit to the measured profiles. The two fits with fixed anisotropy were constrained during the fit by having the same amplitude in the

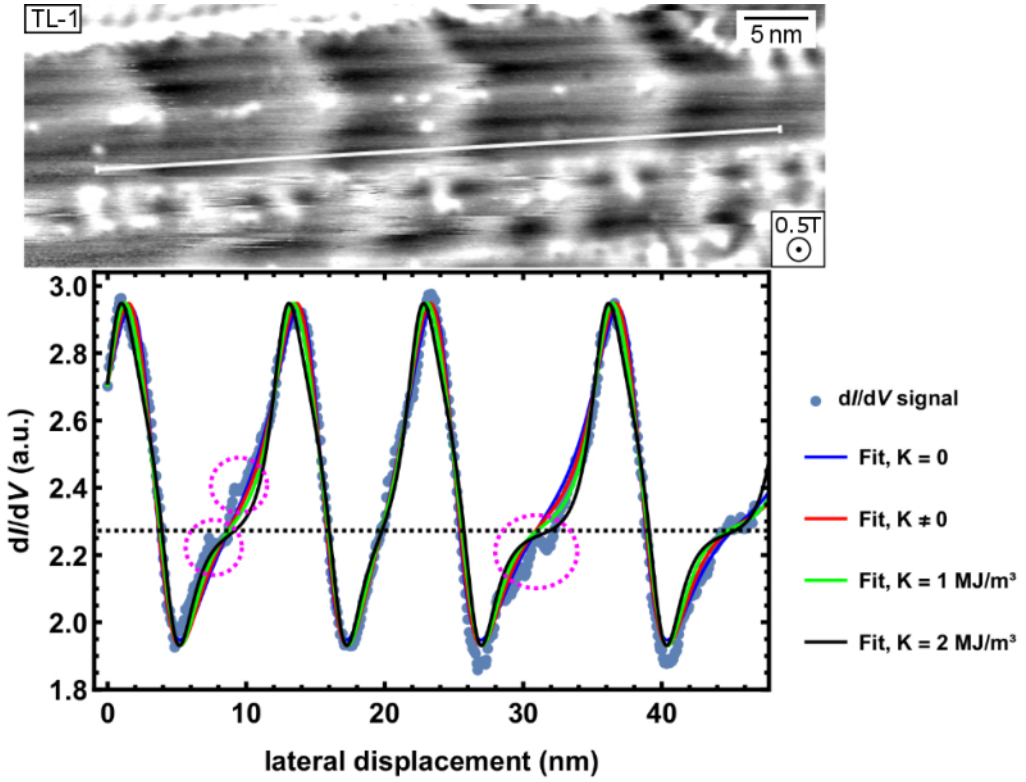

Figure 5.11: Differential tunneling conductance map of the Fe-TL area 1 in magnetic field as marked, already shown in figure 5.6. A white line marks the position of the following line profile in the dI/dV map. The line profile is presented, including 360°-wall-fits with varying effective uniaxial anisotropy. Magenta-colored circles indicate systematic errors in the profiles due to movement of the 360°-walls or defects.

dI/dV signal as the $K \neq 0$ fit to improve their comparability. To match the spin spiral period length λ_0, the line profiles taken along the dislocation lines were compressed for this fit by the sine of the angle between wavefront and dislocation line as illustrated in figure 5.10. Fits to uncompressed line profiles along the dislocation lines would yield magnetic parameters for a system with a longer period length as the propagation direction is tilted relative to the dislocation lines. The fits for $K = 0$ and $K \neq 0$ exhibit only negligible differences and agree well with the recorded data. Moreover, the fits with fixed, larger out-of-plane anisotropies show differences to the previous fits in the peaks where the magnetic moments are parallel to the one in the tip and at the boundaries of the 360° domain walls where the magnetic moments are parallel to the external field. With an increase in anisotropy the fits exhibit an increasing bending at the peaks that is not observed and a steeper slope close to the boundary of the 360° domain walls where the dI/dV signal approaches the dotted line. The latter features fit in some instances better to the observed profiles, which might be an indication for a larger uniaxial anisotropy. The profiles have large systematic errors due to the movement of the 360° domain walls during scanning and the presence of defects. Examples are marked by dotted, magenta-colored circles.

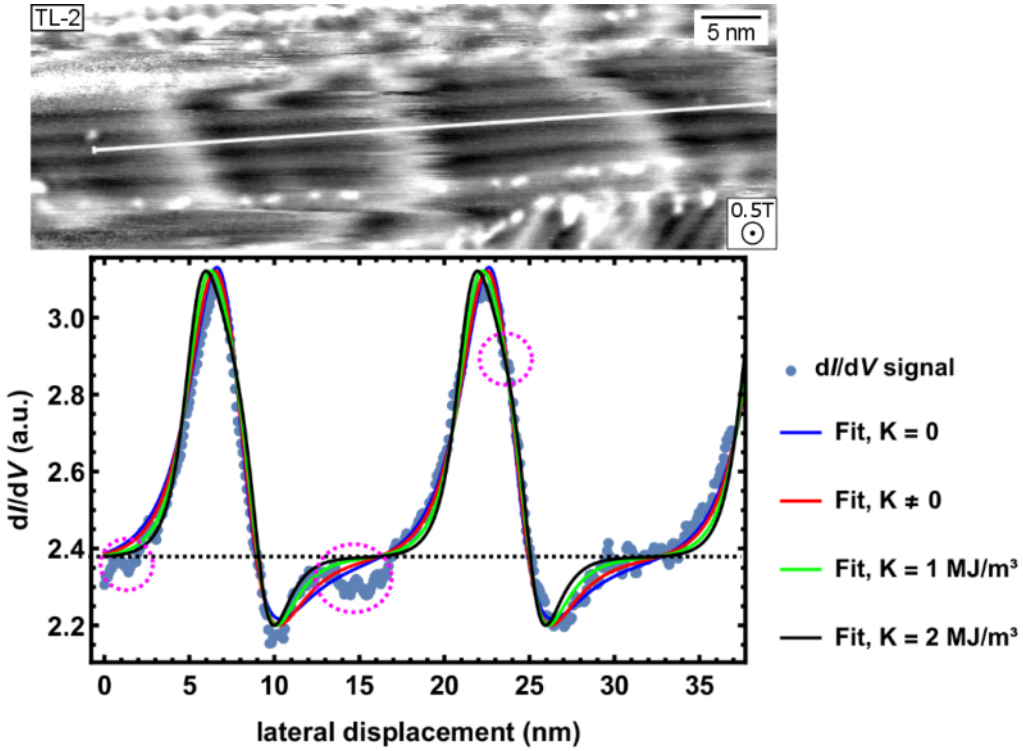

Figure 5.12: Differential tunneling conductance map of the Fe-TL area 2 in magnetic field as marked, already shown in figure 5.6. A white line marks the position of the following line profile in the dI/dV map. The line profile is presented, including 360°-wall-fits with varying effective uniaxial anisotropy. Magenta-colored circles indicate systematic errors in the profiles due to movement of the 360°-walls or defects.

Despite the differences of the fits without anisotropy and strong anisotropy, I cannot exclude larger anisotropies because of the small influence of the anisotropy on the profile shape and the systematic errors in the data. For the same reason, I cannot distinguish whether the system shows either an effective out-of-plane or in-plane anisotropy. Nonetheless, the following derived parameters give an approximation for the magnetization of the single line areas in the Fe-TL.

Table 5.1 presents the best fit parameters for $K = 0$. For comparison, I have added an estimated exchange stiffness A' for Fe-TL from [101]. A. Finco *et al.* neglected anisotropy and used the results of *ab initio* calculations for the Fe-ML on Ir(111) [14] to estimate A' for the corresponding period lengths in the Fe-TL. The estimation and my fit results share the same calculated M_s from the Fe-ML but the estimated A' is derived from the Fe-ML DMI value $D' = 2.8\,\mathrm{mJ/m^2}$. The anisotropy-free fits result in exchange stiffnesses between 1.6 and 1.9 pJ/m and DMI coefficients of 1.9 and 2.8 mJ/m². These results are in good agreement with the estimation which are based on Fe-ML values from *ab initio* calculations [14], except for the second area. Table 5.2 presents the best fit parameters for $K \neq 0$ and in the last row the magnetic parameters for the Pd(hcp)/Fe bilayer on Ir(111) [69] for comparison. The effective anisotropy coefficient K converges in all three areas to about 0.4 MJ/m³. This incorporation

Table 5.1: Parameters from an anisotropy-free fit to several 360° domain walls in an out-of-plane field of 0.5 T. An extra column shows the estimated exchange stiffness A' for the Fe-TL based on *ab initio* calculations for the Fe-ML [14, 101] and equation 5.3. The period length of the spin spiral in zero field λ_0 and the line spacing of the dislocation lines is measured in the real-space maps. For the line spacing the statistical error is given whereas the error is negligible for the spin spiral period.

Area	θ (°)	A (pJ/m)	A' (pJ/m)	D (mJ/m²)	λ_0 (nm)	line spacing (nm)
TL-Fe 1	74	1.8	1.8	2.8	8.1	1.79±0.03
TL-Fe 2	47	1.6	2.3	1.9	10.4	1.91±0.04
TL-Fe 3	46	1.9	1.8	2.8	8.8	1.86±0.04

Table 5.2: Parameters from a fit with $K \neq 0$ to several 360° domain walls in an out-of-plane field of 0.5 T. The last row presents the values of the Pd(hcp)/Fe bilayer on Ir(111) [69]. The period length of the spin spiral in zero field λ_0 and the line spacing of the dislocation lines is measured in the real-space maps. For the line spacing the statistical error is given whereas the error is negligible for the spin spiral period.

Area	θ (°)	K (MJ/m³)	A (pJ/m)	D (mJ/m²)	λ_0 (nm)	line spacing (nm)
TL-Fe 1	74	0.4	2.1	3.2	8.1	1.79±0.03
TL-Fe 2	51	0.3	1.9	2.3	10.4	1.91±0.04
TL-Fe 3	51	0.4	2.2	3.2	8.8	1.86±0.04
Pd(hcp)/Fe bilayer	-	2.5	2	3.9	6.6	-

of anisotropy leads to an increase of the exchange stiffness to values between 1.9 and 2.2 pJ/m. In turn, the DMI coefficient increases to 2.3 and 3.2 mJ/m² to keep the same period length in zero field. For larger period lengths A increases and D stays constant or decreases as expected in both, the $K = 0$ and the $K \neq 0$, fits except for area 2. In comparison to the Pd(hcp)/Fe bilayer the effective anisotropy can be considered as weak which was expected from previous studies, see [101]. Both systems exhibit similar A, but D is significantly decreased relative to the Pd(hcp)/Fe bilayer. The reduction of D is reasonable since the period length of the investigated Fe-TL is larger than that of the Pd(hcp)/Fe bilayer. Moreover, the reduction of D is expected if the DMI is dominated by the Fe/Ir interface and the Fe film becomes thicker. For the three investigated areas a larger line spacing correlates with a larger period length contrary to the claim of an inverse relation in [101]. This result suggests that the spin spiral period depends not only on the line spacing, but also on other effects that have a similar impact on the period length. I expect that the spin spiral period also varies with the proximity to step edges and the magnetism of surrounding Fe layers. Likewise, the inconsistent difference in area 2 might be related to its position close to an Ir(111) step edge and the change in the width of the neighboring

Table 5.3: Parameters from the fits with free uniaxial effective anisotropy parameter K and two fixed values to several 360° domain walls in the Fe-TL area 3 and an out-of-plane field of 0.5 T.

Area	θ (°)	K (MJ/m³)	A (pJ/m)	D (mJ/m²)
TL-Fe 3	51	0.4	2.2	3.2
TL-Fe 3	52	1	2.3	3.3
TL-Fe 3	51	2	2.4	3.7

Fe-TL marked in figure 5.6 c by a blue dotted rectangle. Furthermore, the offset angle θ indicates in all fits that the tip's magnetic moment is canted relative to the surface normal which agrees well with the expected polar angle of $(70 \pm 14)°$ derived from the Fe-DL in Appendix A. The differences in θ between the fits are of a similar magnitude than in the Fe-DL and thus can be attributed to measurement uncertainty and errors. Table 5.3 lists the derived parameters for the fits of different anisotropies in the FeTL area 3. Even a five times larger K leads to an increase in A of only about 10 % and in D of 16 %. For this reason, the results for A and D are still good approximations despite the large possible error in the effective anisotropy.
In summary, I fitted an isotropic, micromagnetic model to the 360° wall profiles in the Fe-TL single line areas that emerge by the application of magnetic out-of-plane fields. The model is based on the continuum approximation and takes nearest-neighbor terms for exchange and DMI, and uniaxial effective anisotropy into account. From the fit I derive a set of corresponding magnetic parameters after estimating the saturation magnetization by using the value for the Fe-ML from *ab initio* calculations [14]. While significant deviations in the anisotropy parameter cannot be excluded due to its small influence on the profile shape and systematic error, the variation of the anisotropy has little influence on the other parameters. For $K = 0$ the derived parameters agree well with the estimation in [101]. The derived parameters for $K \neq 0$ are similar to the known Pd/Fe bilayer on Ir(111) [69] except for a significantly lower uniaxial out-of-plane anisotropy coefficient and a decreased strength of DMI as expected for a thicker film.

5.3 Bilayer of Pd/Fe on Ir(111)

All results reported in this section are already published in [110]. In the following section I present my results concerning the application of magnetic canted and in-plane fields on the Pd/Fe bilayer on Ir(111). At first I will discuss how the propagation direction of the spin spirals is tied to the shape of the Pd island. Then I show how the application of in-plane fields leads to different distortions of the spin spiral depending on the relative orientation of the field to the propagation direction. Finally, I describe

the distortion of skyrmions that result from the application of canted fields and I will determine the sense of magnetization rotation from this induced distortion. In contrast to the previous experiments, I obtained the following results almost exclusively via NCMR contrast.

5.3.1 Spin spiral propagation direction

Bilayer islands of Pd/Fe on Ir(111) were prepared similar to previous studies [22, 69]. Here, I focus on fcc stacked Pd islands on top of fcc grown Fe layers. The orientation of the hexagonal atomic lattice of the Pd/Fe bilayer, which is pseudomorphically grown on the Ir(111) substrate, can be derived from the straight edges of the Pd islands on the Fe monolayer, see figure 5.13 a. Since SP-STM is sensitive to the projection of the local sample magnetization onto the quantization axis given by the SP-STM tip's magnetization direction, the observed stripes on top of the topographically flat island correspond to the wavefronts of the spin spiral (figures 5.13 b and c). These stripes are not strictly parallel across the island but exhibit bends and even branches. A comparison of the orientation of the hexagonal atomic lattice and the propagation direction of the spin spiral $\boldsymbol{k}_{\mathrm{SS}}$ for the area marked in figure 5.13 a indicates that in the interior of the island $\boldsymbol{k}_{\mathrm{SS}}$ preferentially aligns with the high symmetry direction $[11\bar{2}]$. A closer inspection of the spin spiral's propagation vectors $\boldsymbol{k}_{\mathrm{SS}}$ at the island edge (see white arrows in figure 5.13 a) reveals that the spin spiral prefers to propagate along the island's border.

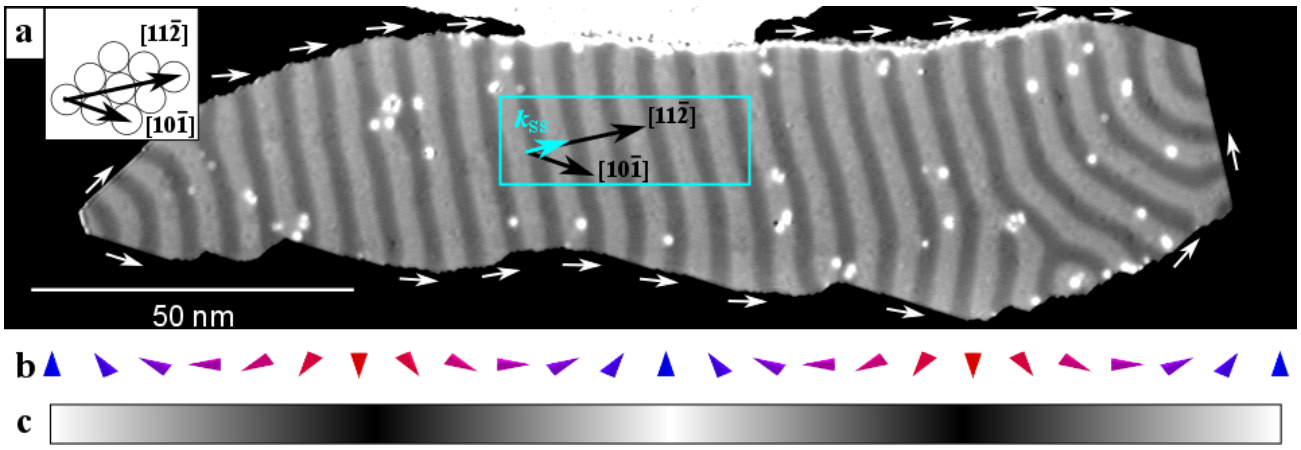

Figure 5.13: Spin structure of a Pd/Fe bilayer island on Ir(111). (a) Constant-current SP-STM map of a Pd/Fe bilayer island on Ir(111) exhibiting a spin spiral state taken by M. Menzel (Measurement parameters: $T = 8\,\mathrm{K}$, $V = 50\,\mathrm{mV}$, $I = 0.2\,\mathrm{nA}$). An out-of-plane magnetized Cr bulk tip was used. The inset shows the orientation of the hexagonal lattice with its crystallographic directions. The white arrows indicate the local spin spiral propagation direction $\boldsymbol{k}_{\mathrm{SS}}$ at the island's border. The blue arrow displays $\boldsymbol{k}_{\mathrm{SS}}$ within the area indicated by the blue rectangle. (b) Side view schematics of a cycloidal spin spiral and (c) top-view of the expected SP-STM contrast obtained with an out-of-plane sensitive probe tip.

In order to obtain deeper insight into the mechanisms of the arrangement of the spin-spirals with respect to the island's borders, my coworker J. Hagemeister performed calculations of the equilibrium

energy of a spin-spiral state on a triangular lattice. For simplicity, he took an effective nearest neighbor exchange interaction and DMI of strengths J and D per atom into consideration with a D/J ratio close to the experimental system [111]. He found that within an extended magnetic film a reorientation of $\boldsymbol{k}_{\mathrm{SS}}$ from the high symmetry direction $[11\bar{2}]$ to the $[10\bar{1}]$ direction reduces the energy by only $1.44{\cdot}10^{-5}\,J$ for each atom. In contrast, he can show that the energy of an atom at the rim along a close-packed row of a magnetic film depends much stronger on the direction of the propagation vector of the local spin spiral configuration. The orientation of $\boldsymbol{k}_{\mathrm{SS}}$ parallel to the rim reduces the energy by $9.2 \cdot 10^{-2}\,J$ for each atom at the rim compared to an alignment of $\boldsymbol{k}_{\mathrm{SS}}$ perpendicular to the rim. In both cases, the internal energy of the spin-spiral state is minimized by an alignment of $\boldsymbol{k}_{\mathrm{SS}}$ with a crystallographic direction in such a way that all bonds contribute to the reduction of both the exchange energy and the DM energy. The larger contribution of the rim is related to its symmetry breaking. In this simple analytical model he has not included the predicted edge tilt at the border [29], but he has checked that it also favors a $\boldsymbol{k}_{\mathrm{SS}}$ parallel to the island edge. A more detailed explanation including the calculations can be found in the supplement of [110] or the PhD thesis of J. Hagemeister [112]. As an example, the values can be approximated for the island shown in figure 5.13. We determined the number of atoms at the border by dividing the perimeter of 445.5 nm by the nearest-neighbor distance (2.715 Å) of the pseudomorphic film. In the same way, the absolute number of atoms in the island was estimated by dividing the island's area of about 6000 nm² by the area of a hexagonal unit cell. Finally, we estimate that within the magnetic island of figure 5.13 a reorientation of $\boldsymbol{k}_{\mathrm{SS}}$ from $[11\bar{2}]$ to $[10\bar{1}]$ can reduce the energy by 3.2 meV, whereas a change of $\boldsymbol{k}_{\mathrm{SS}}$ at the island border from perpendicular to parallel to the rim would lead to a reduction of 350 meV. Thus, we find that the influence of the border on the direction of $\boldsymbol{k}_{\mathrm{SS}}$ is about 100 times larger than that of the inner part for this particular island. This means that the details of the spin spiral in an island, such as bends and branches, are governed by the borders.

Besides SP-STM measurements the recently discovered NCMR effect [105] can be exploited to investigate changes in the non-collinearity of the sample magnetization even with a non-magnetic STM tip. The measurement of NCMR with non-magnetic probe tips avoids ambiguities in data interpretation as it is independent of the external magnetic field. In contrast, in SP-STM studies with ferromagnetic probe tips a reorientation of the tip's magnetization direction in an external magnetic field might occur. Figure 5.14 shows NCMR images of a Pd/Fe bilayer island as a function of an externally applied magnetic field, as measured with a non-magnetic STM tip. In the Pd/Fe bilayer system, the NCMR contrast can be observed in a bias voltage interval of 600 mV to 800 mV; at other bias voltages this contrast vanishes. It roughly scales with the nearest-neighbor-angle θ_{nn} and the dI/dV signal decreases with increasing θ_{nn} [105]. A homogeneous spin spiral is characterized by a constant θ_{nn} and thus would display a constant dI/dV signal, as sketched in figure 5.14 a. The Pd/Fe bilayer system is known to exhibit an out-of-plane easy axis [69, 102, 103], and thus the spin spiral is inhomogeneous which means that θ_{nn} oscillates between in-plane and out-of-plane parts of the spin spiral as illustrated in figure 5.14 a. Because of this inhomogeneity the characteristic stripe pattern of the spin spiral can be

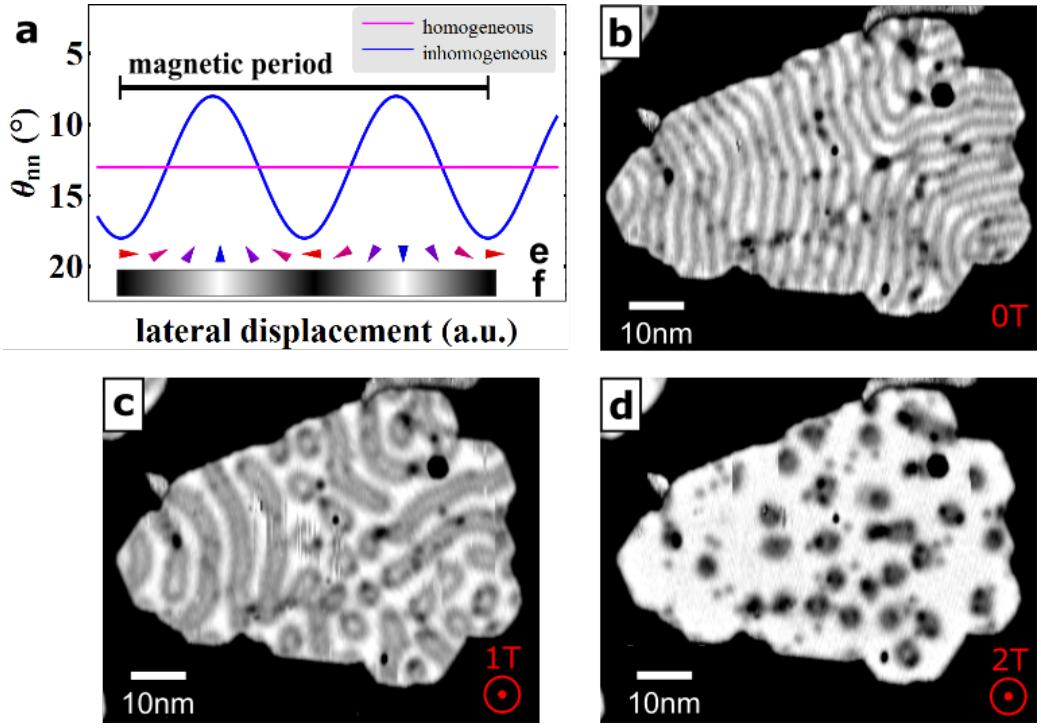

Figure 5.14: (a) Illustration of θ_{nn} along the propagation direction of a homogeneous and an inhomogeneous spin spiral with arrows indicating the corresponding magnetization orientation. (e) Side-view schematics of a cycloidal spin spiral with (f) corresponding topview of the NCMR contrast in zero field. dI/dV STM maps of a Pd/Fe bilayer island on Ir(111) revealing its spin structure via NCMR contrast: (b) without an external magnetic field applied, and with a perpendicular field of (c) $B = 1\,\mathrm{T}$ and (d) $B = 2\,\mathrm{T}$ applied (Measurement parameters: T = 4.7 K, V = -0.7 V, I = 2 nA). A non-magnetic STM tip was used.

observed by NCMR imaging, see figure 5.14 b. Furthermore, for this island I find that the direction of $\boldsymbol{k}_{\mathrm{SS}}$ is governed by the border. In figures 5.14 c and d the response to an out-of-plane magnetic field is demonstrated. In the mixed phase at $B = 1\,\mathrm{T}$ spin spirals and skyrmions coexist [22], see figure 5.14 c. The part of the spin spiral with magnetic moments aligned parallel to the external field increases in width, leading to a local decrease of θ_{nn} and thus an increased dI/dV signal due to NCMR. The area antiparallel to $\boldsymbol{B}$ shrinks, implying larger θ_{nn} and decreased dI/dV signal. The axially symmetric skyrmions in the Pd/Fe bilayer appear in NCMR images as rings at small magnetic fields, because the region of largest non-collinearity is close to the area with in-plane magnetization. The skyrmions shrink with increasing field resulting in smaller rings and eventually dots [105]. For higher fields, at about $B = 2\,\mathrm{T}$, there are only single, pinned skyrmions left, see figure 5.14 d.

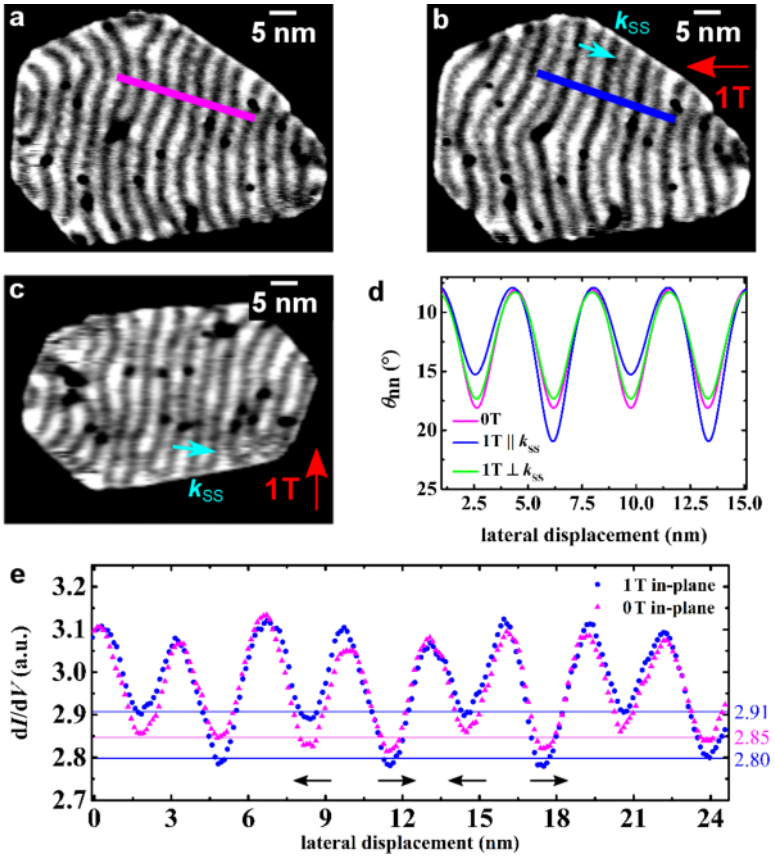

Figure 5.15: dI/dV maps of spin spirals in Pd–Fe bilayer islands on Ir(111) (a) without an applied magnetic field and in an in-plane field of $B = 1\,\mathrm{T}$ (b) collinear and (c) perpendicular to $\boldsymbol{k}_{\mathrm{SS}}$. The images of (a-c) were taken with different tips. (d) Nearest-neighbor-angles along the propagation direction of a spin spiral simulated by OOMMF [113]. (e) Averaged line profiles of the areas marked in (a) and (b) with horizontal lines indicating the mean values for the minima. The black arrows illustrate the orientation of the magnetic moments derived from the change in the dI/dV signal of (b).

5.3.2 Spin spirals in in-plane magnetic fields

Figure 5.15 a shows a Pd/Fe bilayer island in zero field while figures 5.15 b and c show an island with an in-plane field applied which is either collinear or perpendicular to $\boldsymbol{k}_{\mathrm{SS}}$, respectively. While in the latter case no change in the appearance of the spin spiral is observed, a clear difference in the measured dI/dV signal is revealed for figure 5.15 b, where $\boldsymbol{k}_{\mathrm{SS}}$ is roughly collinear to $\boldsymbol{B}$. The line profiles depicted in figure 5.15 e reveal an alternating depth of the minima in the measured dI/dV signal in case of $\boldsymbol{k}_{\mathrm{SS}}$ being parallel to $\boldsymbol{B}$, in contrast to a sine-like dI/dV signal for the zero-field case. As the change of the measured dI/dV signal due to NCMR depends on θ_{nn}, this finding demonstrates that the local non-collinearity of the spin spiral's in-plane parts changes depending on their alignment relative to the applied in-plane field. I again conclude that sample areas where θ_{nn} decreases are parallel to $\boldsymbol{B}$,

whereas an increasing θ_{nn} is observed for areas with magnetic moments antiparallel to $\boldsymbol{B}$. This behavior is in agreement with the proposed cycloidal nature of the spin spiral. For a helical spin spiral, the in-plane parts of the local magnetization are oriented perpendicular to $\boldsymbol{k}_{\mathrm{SS}}$. Therefore, such a spin spiral would exhibit the same change of contrast as the cycloidal spin spiral shows in figure 5.15 b but for a perpendicular orientation of the in-plane field to $\boldsymbol{k}_{\mathrm{SS}}$. Using similar arguments, the NCMR image for an in-plane field perpendicular to $\boldsymbol{k}_{\mathrm{SS}}$ can also be understood, see figure 5.15 c. Here, I expect that the cycloidal spin spiral changes into a transversal-conical phase in order to arrange with the external field, compare figure 2.1 d. In this case, the θ_{nn} are expected to decrease with increasing in-plane field. Micromagnetic simulations for a spin spiral in zero field and in a field collinear to $\boldsymbol{k}_{\mathrm{SS}}$ using OOMMF [113] and parameters obtained from experiments on hcp-stacked Pd/Fe bilayer islands [69] are shown in figure 5.15 d. Their results corroborate my explanation for the NCMR contrast changes as can be seen by the periodic change of θ_{nn} at the minima between the zero field and the collinear field case. The simulation has also been conducted for the case of an in-plane field perpendicular to $\boldsymbol{k}_{\mathrm{SS}}$ which reveals a significantly smaller change in θ_{nn} compared to the collinear field orientation. For this field orientation the strongest change in θ_{nn} occurs at the in-plane parts of the spin spiral since there the external field does not have to compete with the out-of-plane easy axis anisotropy. The simulation shows a tilting of the magnetic moments at the center of the simulated island towards the field direction of roughly 11° and 8° for the in-plane and the out-of-plane part of the spin spiral, respectively. Thus, I expect the difference in dI/dV between in-plane and out-of plane parts to decrease due to an in-plane field perpendicular to $\boldsymbol{k}_{\mathrm{SS}}$ which is difficult to observe experimentally.

Figure 5.16 a shows several Pd/Fe bilayer islands at 4.7 K and in an in-plane field as indicated. At this temperature the application of in-plane fields only leads to the above mentioned distortions of the spin spiral. After warming up the sample to about 30 K and cooling it down again, while the field is applied, the $\boldsymbol{k}_{\mathrm{SS}}$ of some of the islands reorient to become perpendicular to the field, see figure 5.16 b. This demonstrates that the application of in-plane fields leaves the system in a metastable state as it lacks the energy to overcome the barriers to lower energy states. In contrast, figures 5.16 c and d show several islands that were subsequently field-cooled in in-plane fields perpendicular to each other. On the highlighted island the largest part of the spin spiral switches its $\boldsymbol{k}_{\mathrm{SS}}$ to become perpendicular to the field. The other islands also show varying degrees of change in the $\boldsymbol{k}_{\mathrm{SS}}$ of the spin spirals. Hence, a reorientation of the spin spiral's propagation direction upon application of an in-plane field is possible, but the magnetic field competes with the strong coupling of $\boldsymbol{k}_{\mathrm{SS}}$ to the island's rim. These results show that a spin spiral propagation perpendicular to a magnetic in-plane field is energetically preferred.

5.3.3 Skyrmions in canted magnetic fields

Application of out-of-plane magnetic fields leads to a phase transition from the spin spiral state to the skyrmionic state [22], as shown in figure 5.14. For the out-of-plane fields used here the in-plane part of the skyrmion shows the highest non-collinearity and thus the lowest dI/dV signal [105], see

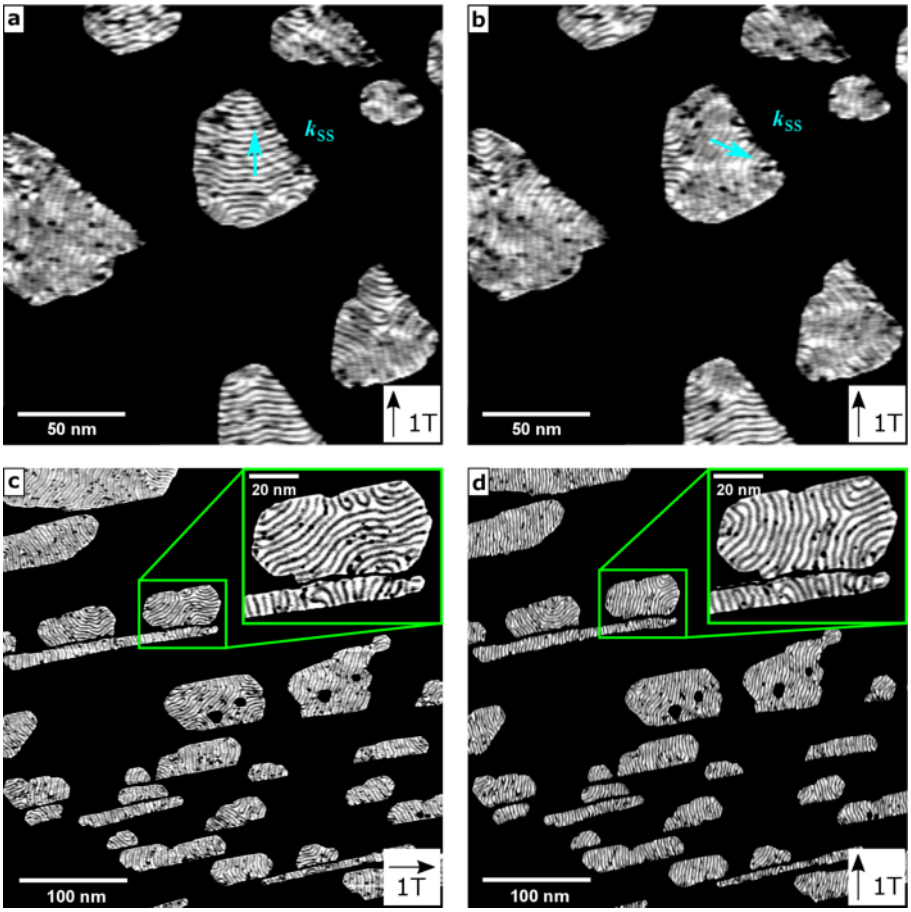

Figure 5.16: dI/dV maps of Pd/Fe bilayer islands obtained with a non-magnetic STM tip. While for the measurement in (a) the magnetic field was applied after cool-down of the sample, in (b-d) the sample was field-cooled (from 30 K to 4.7 K) in in-plane fields as indicated. The maps of the highlighted areas are high-resolution scans revealing changes in the propagation direction of the spin spirals.

figure 5.14 c. Figures 5.17 a and b show numerous skyrmions in canted fields. The STM measurement parameters that are necessary to observe the NCMR contrast can lead to annihilation and creation of skyrmions on the time-scale of the STM scan, thereby causing sudden jumps, i.e. line noise, in the STM images. While in figure 5.17 a the skyrmions have a tendency to exhibit a lower dI/dV on their left side, the skyrmions in the inverted in-plane field show likewise a tendency of a reduced dI/dV signal on their right side, see figure 5.17 b. A particularly stable skyrmion is marked and examined by high-resolution maps (figures 5.17 c and d) together with the corresponding line profiles along the direction of the applied in-plane field (figure 5.17 f). The observed change in dI/dV is similar to the one for the spin spirals: again, the dI/dV signal changes according to the orientation of the spin structure relative to the direction of the applied magnetic field, and I find the strongest change in the in-plane regions. Since the dI/dV signal in NCMR contrast images depends roughly on θ_{nn}, I conclude that θ_{nn} in the in-

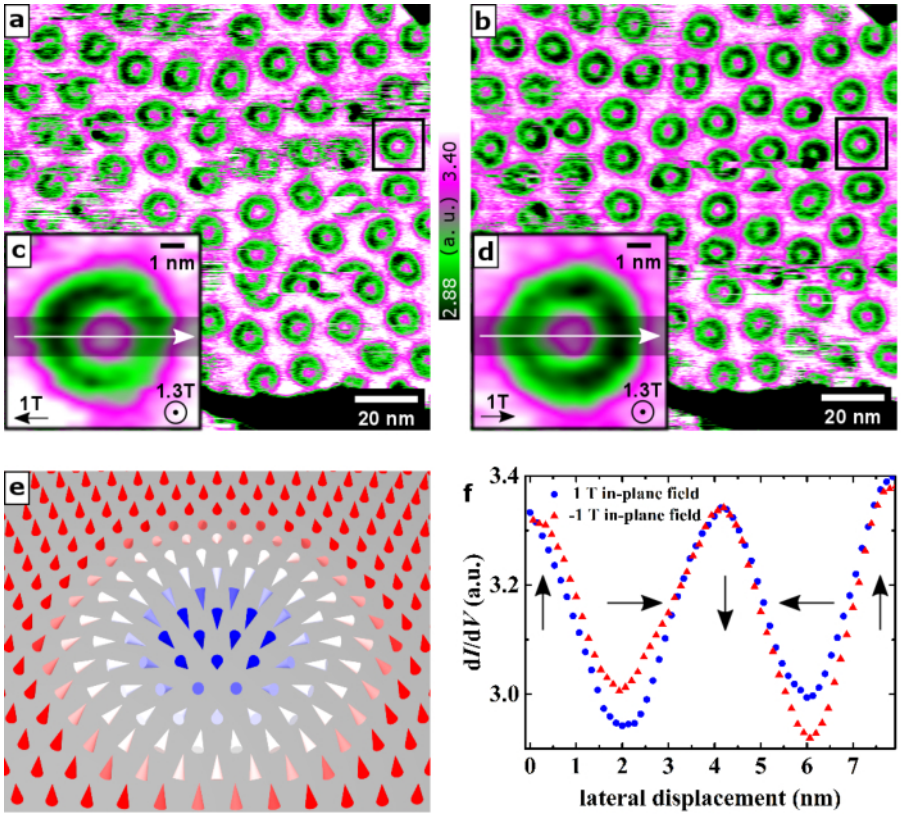

Figure 5.17: (a,b) dI/dV maps of a Pd/Fe bilayer island in a perpendicular field of $B = 1.3\,\mathrm{T}$ and in-plane fields of $|B| = 1\,\mathrm{T}$ pointing in opposite in-plane directions. (c) and (d) show higher resolution Gauss-filtered dI/dV maps of single skyrmions indicated in (a) and (b) by black squares. (e) Illustration of a cycloidal skyrmion with cones representing the magnetic moments. (f) Averaged line profiles taken from (c) and (d); the shaded areas in (c) and (d) show the regions used for averaging.

plane parts of the spin structure increases on one side of the skyrmion and decreases on the other side. Thus, the previously rotational symmetric skyrmion [22, 69] experiences a symmetry breaking and is transformed into a non-circular skyrmion with mirror plane symmetry along the direction of the in-plane field component. However, the exact shape of the skyrmion also strongly depends on the vicinity to other skyrmions or defects. Especially, the measured dI/dV signal in the area between skyrmions, which exhibits a small θ_{nn}, depends on the distance between the skyrmions or skyrmions and defects in the Pd/Fe bilayer. This explains the different dI/dV signals at the rims of the skyrmions that can be observed in the line-profiles of figure 5.17 f. The response to the canted magnetic field confirms that the observed skyrmions are cycloidal. For a helical skyrmion the asymmetry in the in-plane parts would show up on the axis perpendicular to the applied field direction. The data obtained also allows a determination of the sense of rotation as enforced by the DMI. The observed asymmetry directly reveals in which direction the in-plane parts of the skyrmion, that are collinear to the applied field, are

pointed. Therefore, in combination with the orientation of the applied field's out-of-plane component I can derive the perpendicular orientation of the magnetic moments in the center of the skyrmion and its surrounding, compare figure 5.17 e. The spatial distribution of the magnetic moments exhibits a clockwise rotation from left to right (as illustrated by black arrows in figure 5.17 f), and thereby the experimental results confirm the theoretical predictions by B. Dupé *et al.* [102] and E. Simon *et al.* [103].

Summary

I have shown that the spin spirals in Pd/Fe bilayer islands prefer to propagate along the islands' borders. A calculation by my coworker J. Hagemeister corroborated the experimental results. His calculations showed that the coupling of the spin spiral to the border is by two orders of magnitude stronger than the coupling to a particular symmetry direction of the hexagonal atomic lattice. In-plane magnetic fields change the nearest-neighbor-angles between magnetic moments of the spin spiral's in-plane parts if applied collinear to the spin spiral's propagation direction, thereby providing an experimental proof that the spin spiral is cycloidal. In contrast, for a perpendicular orientation of the in-plane field relative to the spin spiral's propagation direction, my OOMMF [113] simulations suggest a distortion towards a transversal-conical spin spiral. Field-cooling samples in differently oriented in-plane fields leads, depending on the island's shape, to a reorientation of the spin spiral propagation direction. A canted field induces an asymmetry in the skyrmion's shape along the field direction, thereby breaking its rotational symmetry. For skyrmions the induced asymmetry not only reveals their cycloidal nature, but additionally allows the determination of the sense of magnetization rotation.

5.4 Pd and hydrogen on higher layers of Fe on Ir(111)

In order to find new non-collinear magnetic structures in thicker magnetic films I deposited about 0.3 ML of Pd on several layers of Fe on Ir(111). Thicker layers of magnetic material on the Fe/Ir interface are expected to exhibit larger ratios of Heisenberg exchange to DMI [111]. Furthermore, the use of Pd as a top layer for the Fe-ML on Ir(111) leads to an increase of the magnetic period lengths and even skyrmions [22]. Therefore, the deposition of Pd as a top layer on higher layers of Fe might lead to spin spirals and skyrmions with larger period lengths. I produced samples that consist of two to five layers of Fe with Pd islands on every layer, as can be seen in figure 5.18. In an early stage of the investigation I found with my co-worker Dr. Pin-Jui Hsu that the Fe-DL exhibits a drastic change in its magnetic structure and thus we focused on its investigation. I found a similarly strong change for the double line areas of the Fe-TL and thus dedicated the last part of this section to the investigation of Pd deposition on the Fe-TL.
Figure 5.18 b shows the Pd/Fe arrangement that results from the deposition of about 0.3 ML of Pd on top of two to five layers of Fe on Ir(111). The fourth (quadruple layer - QL) and the fifth atomic layer

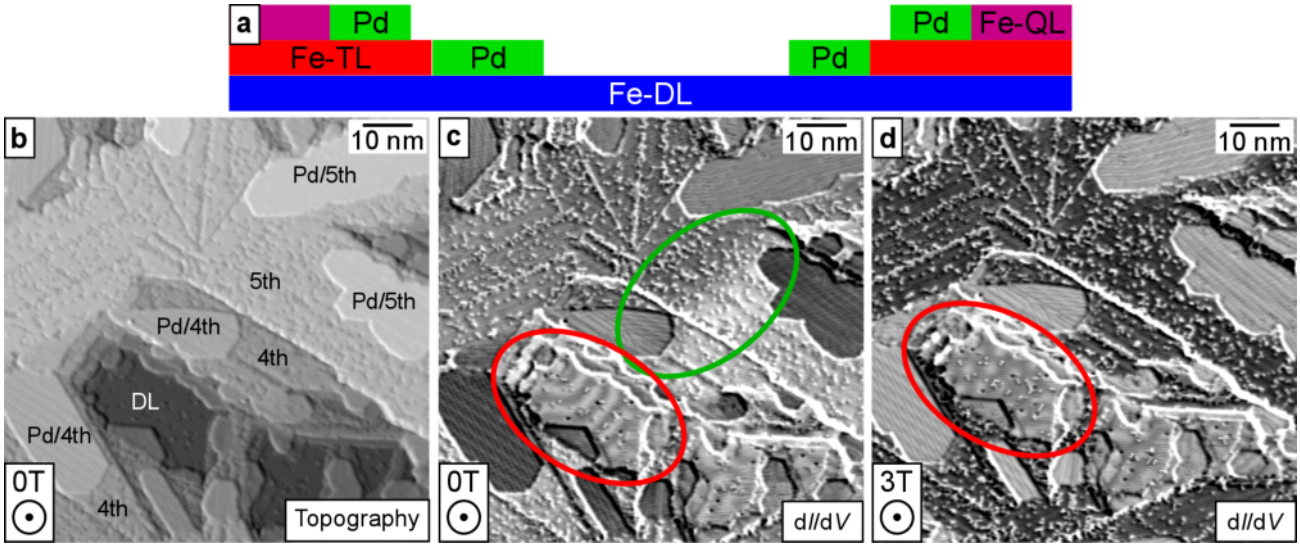

Figure 5.18: (a) Side view on a sketch of Pd growth on different Fe layers on Ir(111). (b) Topography map of Fe layers on Ir(111) with number of atomic layers as marked and covered by about 0.3 ML of Pd in zero field taken with a Cr-bulk tip. (c) and (d) show the differential tunneling conductance maps of the area from (b) in a magnetic out-of-plane field of 3 T (c) and in a field reduced to zero (d). (Measurement parameters: V = -0.7 V, I = 1 nA, T = 4.7 K)

of Fe grow epitaxially but with many defects on the Fe-TL and thus roughly resemble the structure of the Fe-TL in topography. Furthermore, the growth of the Pd islands seems to be epitaxial and with only few defects or contaminants on all layers of Fe. In figure 5.18 c the fourth and the fifth Fe layer exhibit both two different dI/dV signal levels within their layer with a clear separation along a line across both layers marked by a green ellipse. An application of a magnetic out-of-plane field of 3 T results in a uniform dI/dV signal in the fourth and fifth Fe layers, see figure 5.18 d. All of these observations prove that the fourth and the fifth Fe layers are FM. Consequently, the separation line between the two areas that exhibit different dI/dV signals in figure 5.18 c corresponds to a domain wall. The same holds for the Pd islands on top of the fourth and fifth layer of Fe. They are coupled to the magnetic state of the Fe layer below in a way that the Pd islands exhibit a larger and a smaller dI/dV signal that appears inverted relative to the dI/dV signal of the Fe layer below, see figure 5.18 c. If the Fe layer shows the smaller dI/dV signal relative to the other part of the Fe layer, then the Pd island on top of it shows the larger dI/dV signal compared to the Pd island on the Fe layer with the relatively smaller dI/dV signal. I suggest that the Pd layers hybridize with the subjacent Fe in a similar way as in the well-known Pd/Fe bilayer [102] and thus have to be considered as a single system. For the case of Pd on the double and triple layer of Fe I will present more data later in this thesis.

Already in figures 5.18 c and d a lower layer can be seen (marked by a red ellipse) that exhibits a stripe-like contrast at zero field and dot-like structures in a magnetic out-of-plane field of 3 T. A closer look at this area reveals that it is composed of a hexagonal 0.5 nm-periodic superstructure that is inde-

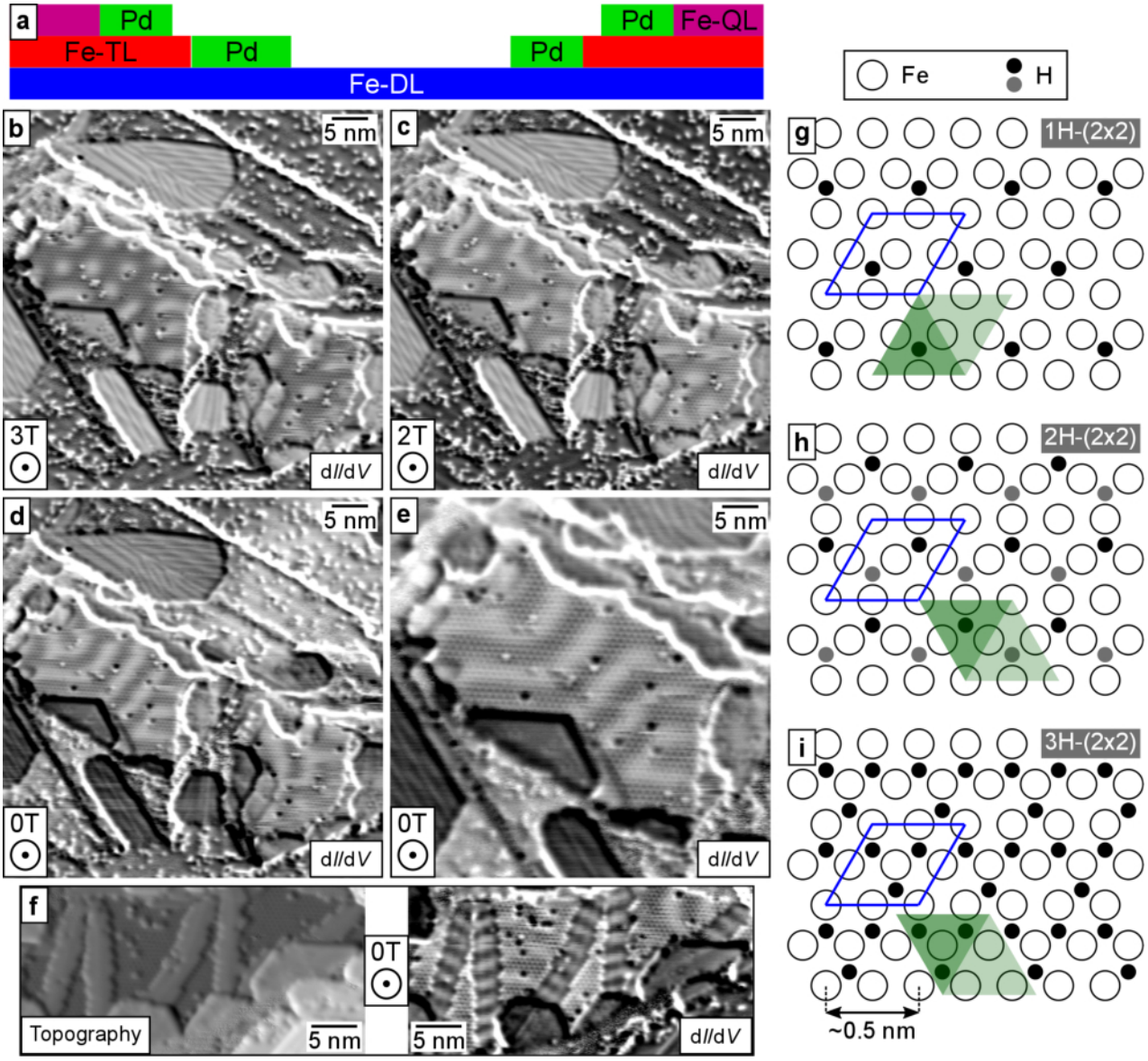

Figure 5.19: (a) Side view of a sketch of Pd growth on different Fe layers on Ir(111). (b-d) show detailed dI/dV maps of the Fe-DL area included in figure 5.18 b-d in magnetic out-of-plane fields as marked. The fields were applied in the same order as the maps are shown. (e) is a more detailed dI/dV map of the Fe-DL that clearly exhibits a hexagonal 0.5 nm-periodic superstructure. The set of topography and dI/dV maps presented in (f) exhibit both pseudomorphic and reconstructed areas of the Fe-DL taken in the same measurement series as figure 5.18 in zero field. (g-i) Top view on three proposed (2×2) structure models with different number of hydrogen atoms per blue marked unit cell. The different colors for hydrogen atoms mark if the hydrogen is located on either an fcc or hcp hollow site. The green shaded triangles illustrate how the respective structure might exhibit the superstructure's observed contrast. (Measurement parameters: V = -0.7 V, I = 1 nA, T = 4.7 K)

pendent of the applied field, see figure 5.19. The height of this area relative to the other atomic layers corresponds to a DL but the observation of the superstructure already excludes that the layer in question is the well-known Pd/Fe bilayer. Another area, see figure 5.19 f, reveals that the superstructure grows in the strained part of the Fe-DL. It even seems that the superstructure on the strained Fe-DL splits the reconstructed area along their hollow site position lines. The stripe- and dot-like structures within the superstructure are magnetic in nature as they correlate with the applied external magnetic field as can be seen in figures 5.19 b-e. I conclude that the magnetic structures are spin spirals with a period length of roughly 3.5 nm and skyrmions. However, an additional measurement with another orientation of the tip's magnetization is necessary to confirm this conclusion. My co-worker Dr. Pin-Jui Hsu has already successfully conducted such an investigation but the results are not yet published. In order to exclude that the observed structure might involve contaminants like hydrogen instead of the evaporated Pd, I repeated the sample preparation with the only difference being a closed shutter in front of the MBE device. This means that the Pd is evaporated but cannot reach the sample. The resulting sample showed a significant amount of the 0.5 nm-periodic superstructure and slightly blurred spin spirals on the reconstructed Fe-DL, see Appendix E. This experiment excludes any involvement of Pd in this superstructure. Instead, the superstructure results from hydrogen that is emitted from the heated Pd evaporant as the superstructure coverage depends on the Pd deposition time. Pd is known to be able to store large amounts of hydrogen [114] and to dissociate hydrogen molecules into atoms on its surface [115]. Indeed, depositions of atomic hydrogen by my co-worker Dr. Hsu using a dedicated hydrogen source on the Fe-DL have proven that the observed superstructure results from atomic hydrogen. Thus, the hydrogenation of the Fe-DL increases the spin spiral period from about 1.2 nm [99] to 3.5 nm.

By SP-STM measurements alone it cannot be distinguished if the hydrogen is located on top of the Fe layers or in interstitial sites between both Fe layers or the Fe and Ir interface. Nonetheless, I present in figures 5.19 g-i three possible hydrogen-overlayer structure models for the hydrogenated Fe-DL. The same structures can also form on interstitial sites but they are shown here as an overlayer for the purpose of clarity. All of them exhibit the 0.5 nm-periodic hexagonal symmetry seen in figure 5.19 e in form of dark and bright triangles illustrated in figures 5.19 g-i with shaded triangles. The structure models differ in the number of hydrogen atoms per unit cell. In the 1H-(2×2) and 3H-(2×2) structures the hydrogen atoms are positioned completely on either the fcc or hcp hollow sites while the 2H-(2×2) grows in a 1:1 ratio on hcp and fcc hollow sites. As a consequence, the 1H-(2×2) and 3H-(2×2) structures can exhibit two different contrasts in STM due to the two different stackings. However, this cannot be used to distinguish the structures as the second Fe layer itself can grow in either an fcc or hcp stacking on top of the Fe-ML. Any observed difference in contrast of two superstructure areas can be related to a different Fe stacking. It might be possible to distinguish the different structures via high-resolution STM maps showing few unit cells, similar to [116]. In such a map the 2H-(2×2) structure should exhibit three different STM spectra, one for the hydrogen free positions and two more for hydrogen on the fcc and hcp position. In contrast I expect only two different STM spectra for the

other two proposed structure models.

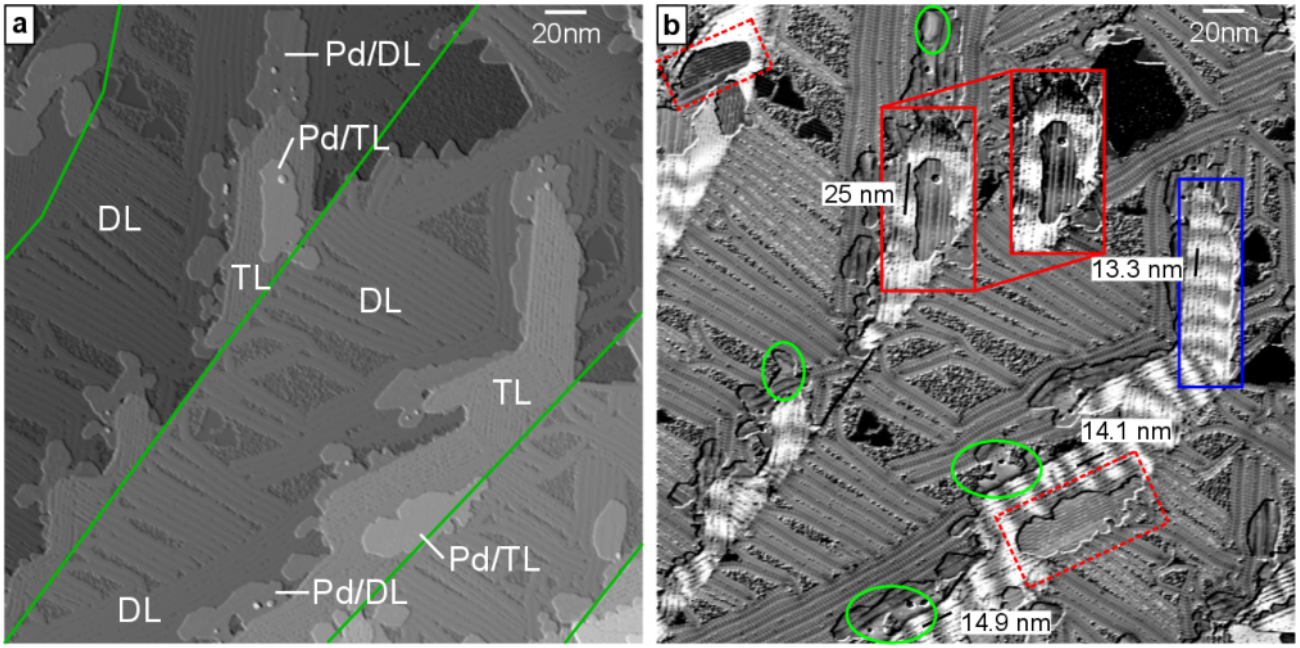

Figure 5.20: (a) Topography and (b) differential tunneling conductance maps of the DL and the TL of Fe on Ir(111) covered with about 0.3 ML of Pd as marked in zero field. Step edges of the Ir(111) are marked in (a) by green lines and some Fe layer heights are marked. In (b) a large Pd island that is magnetically coupled with the subjacent Fe-TL is marked and presented with an adapted color range. The green ellipses highlight areas that correspond to growth of Pd on the strained Fe-DL. (Measurement parameters: V = -0.7 V, I = 1 nA, T = 4.7 K)

Since both the fourth and fifth Fe layer as well as the Pd on top of these layers do not exhibit non-collinear magnetism, I decided to deposit Pd on samples exhibiting only the second and third layer of Fe on Ir(111) to find possible non-collinear magnetic structures. Therefore, I deposited an amount of Fe that corresponds to two closed ML and the same amount of Pd as on the previous sample (0.3 ML). The result can be seen in figure 5.20.

There are few patches of the first and third layer of Fe but most of the surface consists of the second layer. The Pd grows epitaxially on every Fe layer and predominantly at the lower part of the step edge. Most striking is the change of the Fe-TL, both to its topography and its magnetic structure. The surface roughness of the Fe-TL increases in the form of contaminants on top of its dislocation lines. A closer look reveals that this is only the case for the double line areas. In contrast, the areas that exhibit negligible surface contamination can be identified as single line areas because of the well-known tilting of the propagation direction relative to the dislocation lines. As an example, the area in figure 5.20 b marked by a blue rectangle shows the contaminated double line area in its left part and the pristine single line area in its right part. The period lengths of the spin spirals in the single line areas increased slightly to values between 12 and 14.5 nm compared to the former known range of 5.5

to 10 nm [101]. Moreover, the areas with the rough surface that correspond to the double line areas show a strongly increased period length of 13 to 15 nm instead of the known range of about 3 to 4 nm [101]. Additionally, the spin spirals in the double line area do not exhibit the zigzag-like shape due to the row-wise alternation of the propagation direction but the spin spiral wavefronts are blurred and form a straight line perpendicular to the dislocation lines. Since Pd MBE always deposits hydrogen at the same time, I cannot distinguish which element causes the changes in the Fe-TL double line areas from this experiment alone. The deposition of atomic hydrogen on the Fe-TL with post-annealing by my co-worker Dr. Hsu proves that the preferred contamination of the double line areas occurs due to the presence of hydrogen. For the single line areas he measured similar increases of the spin spiral periods up to 13 nm, whereas the increase of the periods in the double line areas of up to 8 nm due to pure atomic hydrogen is significantly smaller than for the case of Pd deposition. Hence, the Pd seems to be responsible for the increased period length in the double line areas. As the spin spiral period is also increased in areas without any Pd islands on top, I propose that single Pd atoms mix into vacancies of the hollow site lines of the double line area. However, changes in the double line areas due to incorporation of Pd cannot be investigated directly because the surface of the double line area is covered by hydrogen after a Pd deposition. Instead, my proposition is supported by the fact that despite about 0.3 ML of Pd were deposited only about 0.2 ML are visible in form of Pd islands. I suggest to investigate the visible coverage of Pd for samples with increased Fe-TL coverage and longer Pd deposition times. An increase of the ratio between expected Pd coverage and observed Pd coverage would corroborate my proposal concerning the Pd incorporation in the double line areas of the Fe-TL. Besides by the surface roughness, both areas of the Fe-TL can also be distinguished by the dI/dV signal of the Pd islands on top. The comparison of the Pd islands highlighted by rectangles in figure 5.20 b reveals that they exhibit the topography of the subjacent layer which results either in a single or a double line pattern. In a similar way the Pd on the Fe-DL adapts the shape and thus the surface features of the subjacent Fe-DL. Consequently, the Pd on top of the reconstructed areas closely resembles the reconstructed topography. Moreover, the Pd on the strained Fe areas has a homogeneous appearance, see green ellipses in figure 5.20 b.

One Pd island on a double line area of the Fe-TL marked by a red rectangle in figure 5.20 b shows non-collinear magnetism. This island exhibits a stripe pattern that corresponds to a spin spiral with a period of roughly 25 nm, exactly like the subjacent Fe layer but with an inverted contrast. Hence, I propose that the Pd island is intimately coupled to the Fe layers via hybridization of their d states which leads to the significant increase in period length of the spin spiral. However, *ab initio* calculations are necessary to prove such an effect on the magnetic structure of the Fe-TL by the Pd layer. In contrast, there are two similarly sized Pd islands on top of single line areas marked by dotted, red rectangles which exhibit no sign of non-collinear magnetism. Moreover, the Pd islands on the reconstructed areas of the Fe-DL show no sign of non-collinear magnetism. However, the growth of larger Pd islands than presented here is necessary to study possible non-collinear magnetism with period lengths above roughly 10 nm. In the case of Pd on top of the Fe-DL's strained areas the island sizes presented here

are too small to draw a conclusion concerning the resulting magnetism. Again, the growth of larger Pd islands is necessary.

Summary

In my experiments I investigated the growth and magnetism of Pd islands on higher layers of Fe and found an influence of hydrogen on the DL and TL of Fe. The origin of the atomic hydrogen is the Pd evaporant which makes a deposition of Pd without hydrogen difficult.
The higher Fe layers as well as all first atomic layers of Pd grow epitaxially. All observations indicate that the fourth and fifth layer of Fe and the Pd islands on top are FM.
After a Pd deposition the Fe-DL exhibits a hexagonal 0.5-nm-periodic superstructure due to the emitted hydrogen. I demonstrated by a fake Pd deposition that the superstructure grows without Pd. Subsequently, my co-worker Dr. Hsu proved with a deposition of atomic hydrogen from a dedicated hydrogen source that the superstructure consists of hydrogen and Fe. This superstructure shows non-collinear magnetic structures corresponding to spin spirals at zero field and skyrmions in out-of-plane fields of 3 T. Compared to the strained areas of the pristine Fe-DL the spin spiral period increased from 1.2 to 3.5 nm. I expect that such a large increase in spin spiral period is dominated by a change in exchange or DM interaction. This result is surprising since the investigation of similar systems revealed only a change of magnetic anisotropy and suppression of magnetism [117–119].
The surfaces of the Fe-TL's double line areas are in contrast to the single line areas strongly contaminated after the Pd deposition. Additionally, the known zigzag pattern of spin spirals wavefronts in the double line areas blurred into broad lines with a roughly four times larger period length. In contrast, the period in the single line areas increased only by a factor of about 1.5 and is similar to increases by deposition of pure atomic hydrogen by my co-worker Dr. Hsu. The atomic hydrogen can only account for half of the period increase in the Fe-TL double line areas that was observed after the Pd deposition. Hence, I expect that the Pd is responsible for this larger increase of the period length.
While the Pd islands on top of the Fe-TL single line areas exhibit no non-collinear magnetic texture, the single Pd island on the Fe-TL double line area shows the same but inverted contrast compared to the subjacent Fe layer. More intriguingly, the period of the latter corresponds to an increase by the factor six compared to the pristine double line areas. I expect this large increase to be caused by a hybridization of d-states between the Pd on top and Fe similar to the Pd/Fe bilayer [102].

Chapter 6
6 Summary and outlook

This chapter summarizes the conducted experiments, their results and remaining questions. Based on the summary I give an outlook on further research possibilities.

I investigated different ultra-thin films consisting of few atomic layers of Fe, Pd and hydrogen on Ir(111) single crystals that exhibit non-collinear magnetic structures at low temperatures. All results were obtained with STM or SP-STM in a magnetic vector-field that allowed the application of up to 1 T in an arbitrary direction. Contrary to previous STM investigations, the use of a magnetic vector field makes it possible to resolve the complete three-dimensional magnetic structure.
I found the sense of magnetization rotation in the reconstructed areas of the Fe-DL in two independent areas. For this purpose, I exploited the negligible response of the magnetic moments in the Fe-DL to external magnetic field by scanning it with a field-dependent SP-STM tip in magnetic out-of-plane and in-plane fields. The magnetic moment of the tip followed the external field resulting in scans with different contrast of the same magnetic structure. As a consequence, the change of the spin spiral contrast relative to defects allowed me to find a clockwise sense of magnetization rotation.
For the Fe-TL the same approach could not be used as the magnetic moments follow the external field to varying degree depending on the period length and the field orientation relative to the dislocation lines. The single line areas with longer period tilt strongly towards the external field. In contrast, the double line areas show a weaker response, especially an in-plane tilting perpendicular to the dislocation lines is impeded. In this experiment a field-independent tip was used as its magnetic moment does not follow the external field and thus all changes in the magnetic contrast can be attributed to tilting of the magnetic moments in the sample. In out-of-plane fields of 0.5 T the single line areas of the Fe-TL exhibit 360° domain walls with an asymmetric profile due to TMR contrast with a tip that exhibits a canted magnetic moment. The lack of change in the dI/dV signal amplitude of the 360° domain walls for canted magnetic fields proves that the magnetic structure is cycloidal in nature. A comparison of the 360° domain wall profiles in different orientations of the external magnetic field revealed the sense of magnetization rotation. I found a clockwise sense of magnetization rotation in four independent areas which has a likelihood of about 6% to occur as a coincidental observation in a system without unique sense of magnetization rotation. In the case of the double line areas the sense of magnetization rotation can be found with the same procedure. However, I investigated only one skyrmion that seems to be influenced by a crystal defect. Thus, the single experiment serves as a scheme for further experiments that might lead to more reliable results.

I propose an isotropic, micromagnetic model as an approximation for the anisotropic magnetism in the single line areas of the FeTL. A full set of micromagnetic parameters can be derived from this model and the shape of the 360° domain wall profiles after estimating the saturation magnetization. While significant deviations in the anisotropy parameter cannot be excluded due to its small influence on the profile shape and systematic error, the variation of the anisotropy has little influence on the other parameters. For $K = 0$ the derived parameters agree well with the estimation in [101]. The derived parameters for $K \neq 0$ are similar to the known Pd/Fe bilayer on Ir(111) [69] except for a significantly lower uniaxial out-of-plane anisotropy coefficient and a decreased strength of DMI as expected for a thicker film.

I have shown that the spin spirals in Pd/Fe bilayer islands prefer to propagate along the islands' borders. A calculation by my coworker J. Hagemeister corroborated the experimental results showing that the coupling of the spin spiral to the border is by two orders of magnitude stronger than the coupling to a particular symmetry direction of the hexagonal atomic lattice. In-plane magnetic fields change the nearest-neighbor-angles between magnetic moments of the spin spiral's in-plane parts, if applied collinear to the spin spiral's propagation direction, thereby providing an experimental proof that the spin spiral is cycloidal. In contrast, for a perpendicular orientation of the in-plane field relative to the spin spiral's propagation direction, my OOMMF [113] simulations suggest a distortion towards a transversal-conical spin spiral. Field-cooling samples in differently oriented in-plane fields leads to a reorientation of the spin spiral propagation direction. A canted field induces an asymmetry in the skyrmion's shape along the field direction which reveals their cycloidal nature and their clockwise sense of magnetization rotation.

I investigated the growth and magnetism of Pd islands on higher layers of Fe and found an influence of hydrogen on the DL and TL of Fe. The higher layers of Fe and all first atomic layers of Pd grow epitaxially. All observations indicate that the fourth and fifth layer of Fe and the Pd islands on top are FM. After the Pd deposition my coworker Dr. Hsu and I found a hexagonal 0.5-nm-periodic superstructure in the Fe-DL. I showed by a fake Pd deposition that the superstructure grows without Pd and my coworker Dr. Hsu later proved with a deposition of atomic hydrogen from a dedicated source that the superstructure consists only of hydrogen and Fe. This superstructure shows non-collinear magnetic structures corresponding to spin spirals at zero field and skyrmions in out-of-plane fields of 3 T. Compared to the strained areas of the pristine Fe-DL the spin spiral period increased from 1.2 to 3.5 nm. I expect that such an increase in spin spiral period is dominated by a change in exchange or DM interaction. This is a surprising finding as investigations of similar systems revealed only a change of anisotropy and suppression of magnetism [117–120]. The surface of the TL's double line areas is in contrast to the single line areas strongly contaminated after the Pd deposition. Additionally, the known zigzag pattern of spin spirals wavefronts in the double line areas blurred into broad lines with a roughly four times larger period length. The periods in the single line areas increased only by a factor of about 1.5 and are similar to increases by deposition of pure atomic hydrogen by my coworker Dr. Hsu. In contrast, the atomic hydrogen can only account for half of the period increase in the Fe-TL

double line areas that was observed after the Pd deposition. Hence, I expect that Pd is responsible for the larger increase of the period length in the double line areas. The Pd islands on the Fe-TL's single line areas show no indication for non-collinear magnetism, whereas a Pd island on the Fe-TL double line area exhibits an inverted contrast relative to the subjacent Fe layer which corresponds to a spin spiral. More intriguingly, the period of the latter corresponds to an increase by a factor of six compared to the pristine double line areas. I expect this large increase to be caused by a hybridization of d-states between the Pd on top and Fe similar to the Pd/Fe bilayer [102].

The experimentally found sense of magnetization rotation in the Pd/Fe bilayer agrees with the theoretical prediction by B. Dupé *et al.* [102] and E. Simon *et al.* [103]. The results on the DL and TL of Fe indicate the same unique sense of magnetization rotation and the micromagnetic parameters for the Fe-TL point to a reduction of the DMI with increasing film thickness. Hence, my experimental results corroborate the claim by B. Dupé *et al.* that the DMI is dominated by the Fe/Ir interface since all the investigated systems share an Fe/Ir interface. An investigation of more independent areas in the DL and TL of Fe would decrease the likelihood for a coincidental observation of the same sense of magnetization rotation and thus make sure that these systems have a unique sense of magnetization rotation.
The proposed isotropic model for the anisotropic magnetism in the single line areas of the Fe-TL is only an approximation. More accurate models have to be based on first principle calculations. However, another experimental study could determine if a uniaxial anisotropy is either in-plane or out-of-plane. If the system exhibits NCMR contrast, the magnetic structure should show a different distortion in in-plane or out-of-plane fields depending on the orientation of the uniaxial anisotropy.
The deposition of Pd on Fe leads to several systems that exhibit non-collinear structures and the investigations in this thesis leave some open questions. High-resolution STM images of the hydrogen superstructure might help to exclude some of the proposed structure models, similar to [116]. Also an investigation of different Pd coverages on the Fe-TL is of interest to study the spin spiral period change in detail and to verify if only the Pd on the double line areas exhibit non-collinear magnetism. In addition, such an investigation could also corroborate my proposal concerning the Pd incorporation in the double line areas of the Fe-TL. Moreover, I suggest to investigate if the application of magnetic out-of-plane fields leads to the formation of skyrmions. Such a system might exhibit skyrmions at higher temperatures as the stability of magnetic long-range order versus temperature was proved to increase with magnetic film thickness [37–39]. Only a deposition of pure Pd on the Fe-TL could clarify how the combined deposition of Pd and hydrogen leads to the larger period increase in the double line area. Such an experiment would need a specialized setup in which not only the Pd evaporant has to be hydrogen-free from the beginning but also the UHV chamber needs to be free of hydrogen.

Bibliography

1. W. Lowrie, *Fundamentals of Geophysics*, p.281 (Cambridge University Press, London, 2007).
2. S. Parkin, *Shiftable magnetic shift register and method of using the same*, US Patent 6,834,005, 2004.
3. M. Hayashi, L. Thomas, R. Moriya, C. Rettner, S. S. P. Parkin, *Science* **320**, 209–211 (2008).
4. S. Parkin, S.-H. Yang, *Nature Nanotechnology* **10**, 195–198 (2015).
5. A. Fert, V. Cros, J. Sampaio, *Nature Nanotechnology* **8**, 152–156 (2013).
6. A. N. Bogdanov, D. A. Yablonsky, *Zhurnal Eksperimentalnoi I Teoreticheskoi Fiziki* **95**, 172–182 (1989).
7. A. Bogdanov, A. Hubert, *Journal of Magnetism and Magnetic Materials* **138**, 255–269 (1994).
8. N. Nagaosa, Y. Tokura, *Nature Nanotechnology* **8**, 899–911 (2013).
9. I. Dzyaloshinsky, *Journal of Physics and Chemistry of Solids* **4**, 241–255 (1958).
10. T. Moriya, *Physical Review* **120**, 91–98 (1960).
11. P. Bak, M. H. Jensen, *Journal of Physics C: Solid State Physics* **13**, L881–L885 (1980).
12. S. Muhlbauer *et al.*, *Science* **323**, 915–919 (2009).
13. A. Fert, P. M. Levy, *Physical Review Letters* **44**, 1538–1541 (1980).
14. S. Heinze *et al.*, *Nature Physics* **7**, 713–718 (2011).
15. N. S. Kiselev, A. N. Bogdanov, R. Schäfer, U. K. Rößler, *Journal of Physics D: Applied Physics* **44**, 392001 (2011).
16. T. Schulz *et al.*, *Nature Physics* **8**, 301–304 (2012).
17. R. Tomasello, E. Martinez, R. Zivieri, L. Torres, M. Carpentieri, G. Finocchio, *Scientific Reports* **4**, 6784 (2014).
18. X. Zhang *et al.*, *Scientific Reports* **5**, 7643 (2015).
19. X. Zhang, M. Ezawa, Y. Zhou, *Scientific Reports* **5**, 9400 (2015).
20. R. Ritz, *Nature Nanotechnology* **10**, 573–574 (2015).
21. G. Finocchio *et al.*, *Applied Physics Letters* **107**, 262401 (2015).

22. N. Romming *et al.*, *Science* **341**, 636–639 (2013).

23. P.-J. Hsu, A. Kubetzka, A. Finco, N. Romming, K. von Bergmann, R. Wiesendanger, *Nature Nanotechnology*, 123–126 (2016).

24. G. Chen, A. Mascaraque, A. T. N'Diaye, A. K. Schmid, *Applied Physics Letters* **106**, 242404 (2015).

25. S. Woo *et al.*, *Nature Materials*, 501–506 (2016).

26. C. Moreau-Luchaire *et al.*, *Nature Nanotechnology* **11**, 444–448 (2016).

27. S. Krause, R. Wiesendanger, *Nature Materials* **15**, 493–494 (2016).

28. A. B. Butenko, A. A. Leonov, A. N. Bogdanov, U. K. Rößler, *Physical Review B* **80**, 134410 (2009).

29. S. Rohart, A. Thiaville, *Physical Review B* **88**, 184422 (2013).

30. A. Siemens, Y. Zhang, J. Hagemeister, E. Y. Vedmedenko, R. Wiesendanger, *New Journal of Physics* **18**, 045021 (2016).

31. J. Sampaio, V. Cros, S. Rohart, A. Thiaville, A. Fert, *Nature Nanotechnology* **8**, 839–844 (2013).

32. M. Bode *et al.*, *Nature* **447**, 190–193 (2007).

33. S. Meckler, N. Mikuszeit, A. Preßler, E. Y. Vedmedenko, O. Pietzsch, R. Wiesendanger, *Physical Review Letters* **103**, 157201 (2009).

34. S.-G. Je, D.-H. Kim, S.-C. Yoo, B.-C. Min, K.-J. Lee, S.-B. Choe, *Physical Review B* **88**, 214401 (2013).

35. G. Chen *et al.*, *Nature Communications* **4**, 2671 (2013).

36. J. J. Chess, S. A. Montoya, E. E. Fullerton, B. J. McMorran, *AIP Advances* **7**, 056807 (2017).

37. C. M. Schneider, P. Bressler, P. Schuster, J. Kirschner, J. J. de Miguel, R. Miranda, *Physical Review Letters* **64**, 1059–1062 (1990).

38. P. J. Jensen, H. Dreyssé, K. H. Bennemann, *Europhysics Letters (EPL)* **18**, 463–468 (1992).

39. H. J. Elmers, J. Hauschild, H. Fritzsche, G. Liu, U. Gradmann, U. Köhler, *Physical Review Letters* **75**, 2031–2034 (1995).

40. C. A. F. Vaz, J. A. C. Bland, G. Lauhoff, *Reports on Progress in Physics* **71**, 056501 (2008).

41. A. Fert, *Materials Science Forum* **59-60**, 439–480 (1990).

42. B. Heinrich, J. Cochran, *Advances in Physics* **42**, 523–639 (1993).

43. R. Skomski, *Simple Models of Magnetism* (Oxford University Press, New York, 2008).

44. A. Crépieux, C. Lacroix, *Journal of Magnetism and Magnetic Materials* **182**, 341–349 (1998).

45. A. Arrott, *Journal of Applied Physics* **34**, 1108–1109 (1963).

46. P. M. Levy, A. Fert, *Physical Review B* **23**, 4667–4690 (1981).

47. P. Ferriani *et al.*, *Physical Review Letters* **101**, 027201 (2008).
48. Y. A. Izyumov, *Soviet Physics Uspekhi* **27**, 845–867 (1984).
49. S. Di Napoli, A. M. Llois, G. Bihlmayer, S. Blügel, M. Alouani, H. Dreyssé, *Physical Review B* **70**, 174418 (2004).
50. Y. Yoshida *et al.*, *Physical Review Letters* **108**, 087205 (2012).
51. M. Heide, G. Bihlmayer, P. Mavropoulos, A. Bringer, S. Blügel, *Psi-k Network, Highlight of the Month* **78** (2006).
52. M. J. Benitez *et al.*, *Nature Communications* **6**, 8957 (2015).
53. H.-B. Braun, *Physical Review B* **50**, 16485–16500 (1994).
54. A. Kubetzka, O. Pietzsch, M. Bode, R. Wiesendanger, *Physical Review B* **67**, 020401 (2003).
55. L. Heyderman, H. Niedoba, H. Gupta, I. Puchalska, *Journal of Magnetism and Magnetic Materials* **96**, 125–136 (1991).
56. J. Ping Liu, Z. Zhang, G. Zhao, *Skyrmions: Topological Structures, Properties, and Applications* (Taylor & Francis Group, Abingdon, UK, 2016).
57. T. Skyrme, *Nuclear Physics* **31**, 556–569 (1962).
58. K. Everschor-Sitte, M. Sitte, *Journal of Applied Physics* **115**, 172602 (2014).
59. H.-B. Braun, *Advances in Physics* **61**, 1–116 (2012).
60. U. K. Rößler, A. N. Bogdanov, C. Pfleiderer, *Nature* **442**, 797–801 (2006).
61. C. Pappas *et al.*, *Physical Review Letters* **102**, 197202 (2009).
62. W. Münzer *et al.*, *Physical Review B* **81**, 041203 (2010).
63. J. M. Higgins, R. Ding, J. P. DeGrave, S. Jin, *Nano Letters* **10**, 1605–1610 (2010).
64. X. Z. Yu *et al.*, *Nature* **465**, 901–904 (2010).
65. X. Z. Yu *et al.*, *Nature Materials* **10**, 106–109 (2011).
66. S. Seki, X. Z. Yu, S. Ishiwata, Y. Tokura, *Science* **336**, 198–201 (2012).
67. A. Tonomura *et al.*, *Nano Letters* **12**, 1673–1677 (2012).
68. Y. Tokunaga *et al.*, *Nature Communications* **6**, 7638 (2015).
69. N. Romming, A. Kubetzka, C. Hanneken, K. von Bergmann, R. Wiesendanger, *Physical Review Letters* **114**, 177203 (2015).
70. G. Binnig, H. Rohrer, C. Gerber, E. Weibel, *Physical Review Letters* **49**, 57–61 (1982).
71. G. Binnig, H. Rohrer, *Reviews of Modern Physics* **59**, 615–625 (1987).
72. J. Chen, *Introduction to Scanning Tunneling Microscopy* (Cambridge University Press, Cambridge, UK, 1993).

73. R. Wiesendanger, *Scanning Probe Microscopy and Spectroscopy: Methods and Applications* (Cambridge University Press, Cambridge, UK, 1994).
74. J. Bardeen, *Phys. Rev. Lett.* **6**, 57–59 (1961).
75. J. Tersoff, D. R. Hamann, *Physical Review B* **31**, 805–813 (1985).
76. C. J. Chen, *Physical Review B* **42**, 8841–8857 (1990).
77. C. J. Chen, *Journal of Vacuum Science & Technology A: Vacuum, Surfaces, and Films* **9**, 44–50 (1991).
78. M. Bode, *Reports on Progress in Physics* **66**, 523–582 (2003).
79. R. Wiesendanger, *Reviews of Modern Physics* **81**, 1495–1550 (2009).
80. M. Julliere, *Physics Letters A* **54**, 225–226 (1975).
81. J. C. Slonczewski, *Physical Review B* **39**, 6995–7002 (1989).
82. R. Wiesendanger, H.-J. Güntherodt, G. Güntherodt, R. J. Gambino, R. Ruf, *Physical Review Letters* **65**, 247–250 (1990).
83. D. Wortmann, S. Heinze, P. Kurz, G. Bihlmayer, S. Blügel, *Physical Review Letters* **86**, 4132–4135 (2001).
84. S. Meckler, M. Gyamfi, O. Pietzsch, R. Wiesendanger, *Review of Scientific Instruments* **80**, 023708 (2009).
85. S. Meckler, PhD thesis, Universität Hamburg, 2010.
86. O. Pietzsch, A. Kubetzka, D. Haude, M. Bode, R. Wiesendanger, *Review of Scientific Instruments* **71**, 424–430 (2000).
87. FEMTO Messtechnik GmbH, Berlin, Germany.
88. SPECS Zurich GmbH, Zurich, Switzerland.
89. C. Hanneken, Diploma thesis, Universität Hamburg, 2011.
90. S. Ceballos, G. Mariotto, S. Murphy, I. Shvets, *Surface Science* **523**, 131–140 (2003).
91. A. Kubetzka, M. Bode, O. Pietzsch, R. Wiesendanger, *Physical Review Letters* **88**, 057201 (2002).
92. A. Li Bassi *et al.*, *Applied Physics Letters* **91**, 173120 (2007).
93. J. P. Ibe *et al.*, *J. Vac. Sci. Technol. A* **8**, 3570 (1990).
94. M. Bode, M. Getzlaff, R. Wiesendanger, *Physical Review Letters* **81**, 4256–4259 (1998).
95. A. Kubetzka *et al.*, *Physical Review Letters* **94**, 087204 (2005).
96. M. Bode *et al.*, *Nature Materials* **5**, 477–481 (2006).
97. MaTecK GmbH, Juelich, Germany.

98. Surepure Chemetals, Florham Park, NJ, USA.
99. P.-J. Hsu, A. Finco, L. Schmidt, A. Kubetzka, K. von Bergmann, R. Wiesendanger, *Physical Review Letters* **116**, 017201 (2016).
100. K. von Bergmann *et al.*, *Physical Review Letters* **96**, 167203 (2006).
101. A. Finco, P.-J. Hsu, A. Kubetzka, K. von Bergmann, R. Wiesendanger, *Physical Review B* **94**, 214402 (2016).
102. B. Dupé, M. Hoffmann, C. Paillard, S. Heinze, *Nature Communications* **5**, 4030 (2014).
103. E. Simon, K. Palotás, L. Rózsa, L. Udvardi, L. Szunyogh, *Physical Review B* **90**, 094410 (2014).
104. K. v. Bergmann, A. Kubetzka, O. Pietzsch, R. Wiesendanger, *Journal of Physics: Condensed Matter* **26**, 394002 (2014).
105. C. Hanneken *et al.*, *Nature Nanotechnology* **10**, 1039–1042 (2015).
106. C. Hanneken, PhD thesis, Universität Hamburg, 2015.
107. K. von Bergmann *et al.*, *Physical Review B* **86**, 134422 (2012).
108. H. J. Elmers, U. Gradmann, *Applied Physics A Solids and Surfaces* **51**, 255–263 (1990).
109. P. Błoński, A. Kiejna, *Surface Science* **601**, 123–133 (2007).
110. L. Schmidt, J. Hagemeister, P.-J. Hsu, A. Kubetzka, K. von Bergmann, R. Wiesendanger, *New Journal of Physics* **18**, 075007 (2016).
111. B. Dupé, G. Bihlmayer, M. Böttcher, S. Blügel, S. Heinze, *Nature Communications* **7**, 11779 (2016).
112. J. C. Hagemeister, PhD thesis, Universität Hamburg, 2016.
113. The OOMMF code is available at http://math.nist.gov/oommf.
114. A. R. Ubbelohde, A. Egerton, *Transactions of the Faraday Society* **28**, 284 (1932).
115. T. Mitsui, M. K. Rose, E. Fomin, D. F. Ogletree, M. Salmeron, *Nature* **422**, 705–707 (2003).
116. E. A. Lewis *et al.*, *The Journal of Physical Chemistry C* **116**, 25868–25873 (2012).
117. D. Sander *et al.*, *Physical Review Letters* **93**, 247203 (2004).
118. F. Máca, A. B. Shick, G. Schneider, J. Redinger, *Journal of Magnetism and Magnetic Materials* **272-276**, 1194–1195 (2004).
119. J. Park, C. Park, M. Yoon, A.-P. Li, *Nano Letters* **17**, 292–298 (2017).
120. B. Santos *et al.*, *Physical Review B* **85**, 134409 (2012).

Publications

Publications

Symmetry breaking in spin spirals and skyrmions by in-plane and canted magnetic fields
L. Schmidt, J. Hagemeister, P.-J. Hsu, A. Kubetzka, K. von Bergmann, and R. Wiesendanger
New Journ. Phys. **18** 075007 (2016)

Guiding Spin Spirals by Local Uniaxial Strain Relief
P.-J. Hsu, A. Finco, L. Schmidt, A. Kubetzka, K. von Bergmann, and R. Wiesendanger
Phys. Rev. Lett. **116** 017201 (2016)

Talks and Posters

Skyrmions and spin spirals in canted and in-plane magnetic fields investigated by STM
L. Schmidt, J. Hagemeister, P.-J. Hsu, A. Kubetzka, K. von Bergmann, and R. Wiesendanger
Poster, **JEMS** 2016, Glasgow, UK
Awarded with best PhD student poster prize

Skyrmions and spin spirals in canted and in-plane magnetic fields investigated by STM
L. Schmidt, J. Hagemeister, P.-J. Hsu, A. Kubetzka, K. von Bergmann, and R. Wiesendanger
Poster, **DPG** Regensburg 2016

Spin spirals and skyrmions in ultrathin films and in-plane magnetic fields investigated by SP-STM
L. Schmidt, P.-J. Hsu, A. Kubetzka, K. von Bergmann, and R. Wiesendanger
Talk, **DPG** Berlin 2015

Spin spirals and skyrmions in in-plane magnetic fields investigated by scanning tunneling microscopy
L. Schmidt
Talk, GrK 1286 Workshop Mölln 2014

Spin-polarized scanning tunneling microscopy
L. Schmidt
Talk, SFB668 PhD students Workshop Wittenbeck 2014

Appendices

Appendix A

In section 5.2.3 I scanned the same areas of reconstructed Fe-DL at the beginning and the end of every measurement series at a certain magnetic field. See figures 6.1 a and c for an example for both reconstructed areas. These reconstructed areas are grown together and thus I expect them to have the same structure, which ensures that they share the same magnetic system parameters. A previous study showed that TMR is the dominant contrast mechanism in the Fe-DL [99]. Consequently, the magnetic signal of the spin spiral depends only on the projection of the magnetic moments onto the tip's magnetic moment. Hence, the maps allow me to determine the orientation of the tip's magnetization by comparing the amplitudes in the magnetic signal of spin spirals with different propagation directions. Here, the magnetic signal corresponds to the variation in the dI/dV signals, see figures 6.1 b and d. A comparison of three spin spirals' amplitudes that have the same magnetization magnitude yields four possible orientations of the tip's magnetic moment that lie in a plane perpendicular to the sample. Two values are revealed for the in-plane and out-of-plane angle, respectively. An exception are the special cases of a perfect out-of- or in-plane orientation of the tip's magnetic moment. In this case the orientation is limited to the two values of the respective axis. In order to distinguish between these four possibilities I use two SP-STM maps of the Fe-TL involving magnetic fields with different orientation. The tilting of the propagation direction relative to the dislocation lines in the bcc-like areas keeps the distance over which the spin spiral can be evaluated short and increases the error in the determination of the propagation direction. Instead, I used the spin spiral at the interface of two bcc-like areas where the growth and spin spiral propagation direction coincide, see black lines in figures 6.1 a and c. The calculated tip orientations for all field values and recorded Fe-DL areas result in an average polar angle of 70° from the surface normal and a maximum error of 14°. The azimuth orientation turns out to be in average 6° off the in-plane field component direction, as drawn in figures 6.1 a and c as black arrows, with a maximum error of 28°.

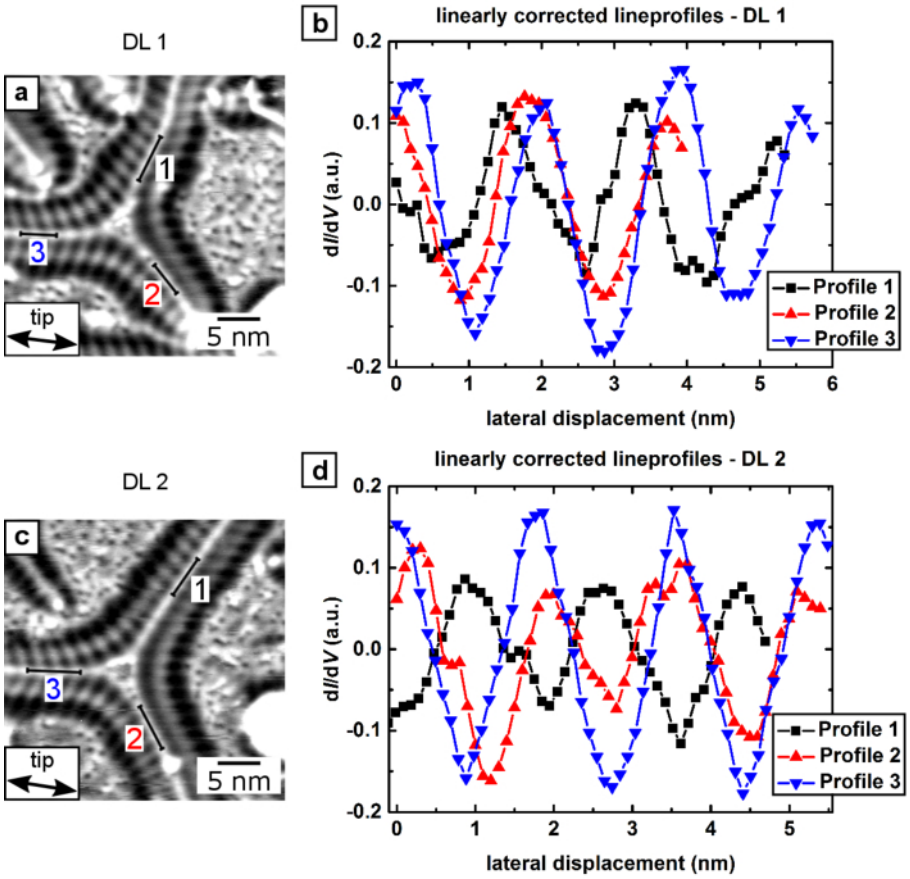

Figure 6.1: Differential tunneling conductance maps of reconstructed areas in the Fe-DL on Ir(111) are shown in (a) and (c). Black stripes indicate the areas which were used to take line profiles shown in (b) and (d). The in-plane direction of the tip's magnetization is marked by an arrow as derived from the spin spiral amplitudes. (Measurement parameters: T = 4.7 K, V = -0.7 V, I = 1 nA)

Appendix B

Here I present the results of the first study on Fe-TL single line areas in canted fields which convinced me to conduct the more elaborate study presented in section 5.2.3. In contrast to the more detailed study I investigated only one Fe-TL area and took only scans of one reconstructed area in the Fe-DL for each field orientation. Furthermore, I did not scan the corresponding Fe-TL area in zero field. Nevertheless, this experiment enables me to determine the sense of magnetization rotation in the same way as in section 5.2.3. Even the fitting with the same models as done in section 5.2.4 is possible which would lead to an almost complete set of magnetic parameters. However, without a map in zero field I do not know the spin spiral period and thus cannot derive the DMI coefficient. Figure 6.2 shows the Fe-TL single line area in two differently oriented magnetic fields. The sense of magnetization rotation

can be identified in the same way as demonstrated in figure 5.8. Since the domain wall profiles in figure 6.2 a appear as symmetric dips in the dI/dV signal, I deduce that the tip's magnetization is roughly parallel to the currently applied field. I conclude a clockwise sense of magnetization rotation, seen from left to right, from the dip-peak order of the domain wall profile in the out-of-plane field, see the illustrated orientation of magnetic moments in figure 6.2 b. It is the same sense as derived for the same system in section 5.2.3.

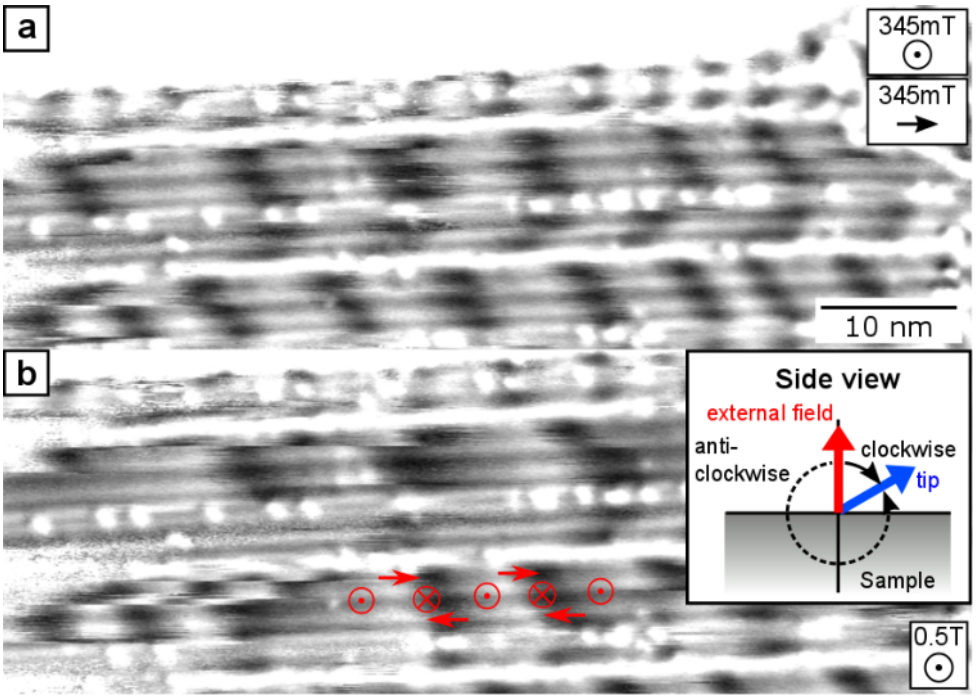

Figure 6.2: (a-b) show dI/dV maps of an Fe-TL single line area on Ir(111) taken with a Cr-bulk tip in fields as marked. Inset: side view of the sample that illustrates the orientation of field in (b) and the rough orientation of the tip's magnetic moment derived from (a). The curved arrows indicate the two senses of magnetization rotation. The orientation of some magnetic moments in (b) is illustrated in red. (Measurement parameters: T = 4.7 K, V = -0.7 V, I = 1 nA)

Appendix C

A comparison of the profile shapes in different fields for area 1 and 2 are shown in figures 6.3 and 6.4. The conclusions here are the same as in section 5.2.3 from figure 5.7. Apart from the amplitude in the dI/dV signal and the propagation direction, the shape of the profiles changes strongly with the reorientation of the external magnetic field. An exception can be found in one of the canted fields in area 2 which shows a significant change in amplitude, see figure 6.4. However, this is a single event and thus can be discarded for the interpretation of this experiment.

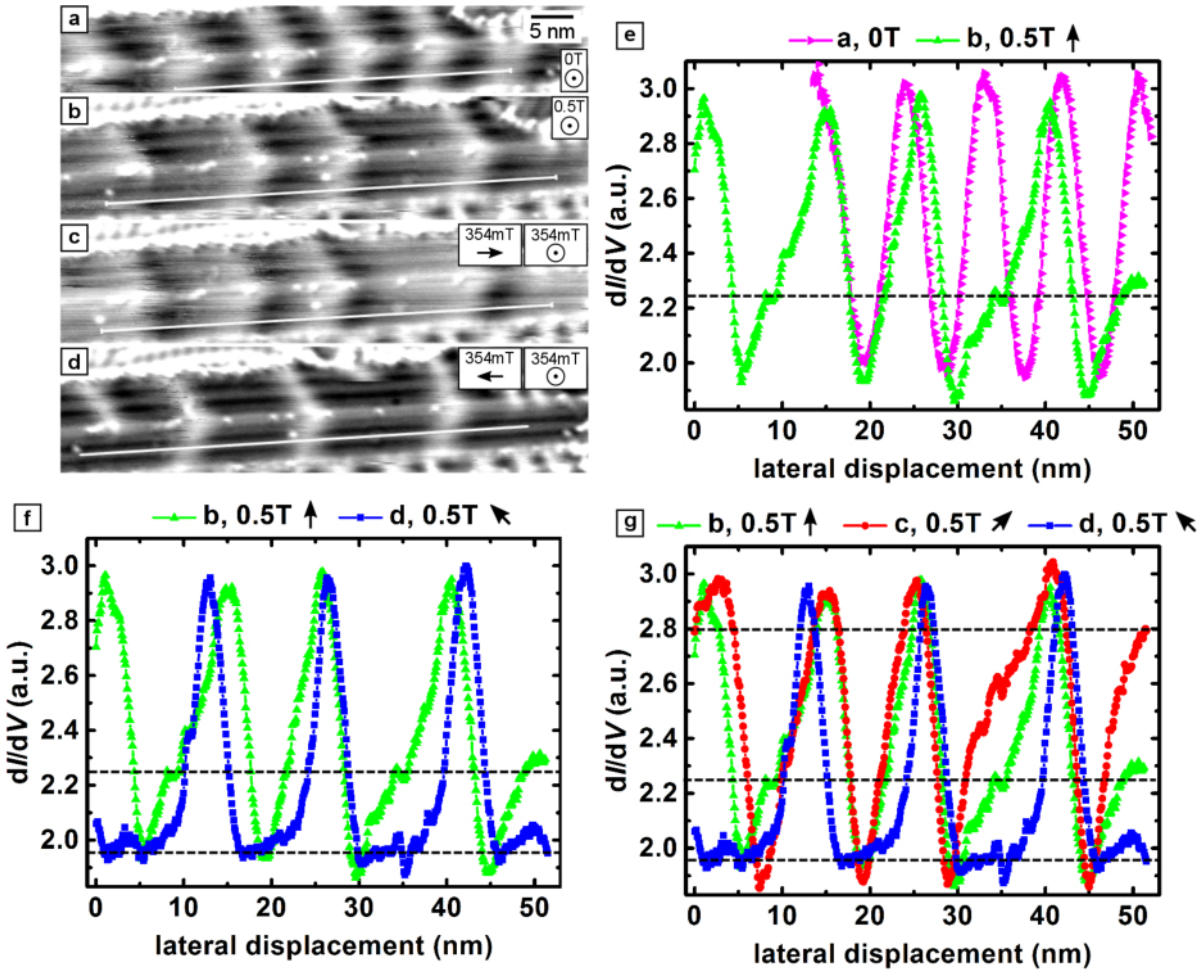

Figure 6.3: (a-d) dI/dV maps of the Fe-TL area 1 of figure 5.6 in (a) zero field, (b) an out-of-plane field of 0.5 T, (c) and (d) a field canted by 45° from the surface normal in both directions towards the double lines and a magnitude of 0.5 T. (e-g) show the line profiles of (a-d) for positions marked by white lines. The dotted horizontal lines indicate the dI/dV signal level at the boundary of the 360° domain walls for each applied external field. (Measurement parameters: V = -0.7 V, I = 1 nA, T = 4.7 K)

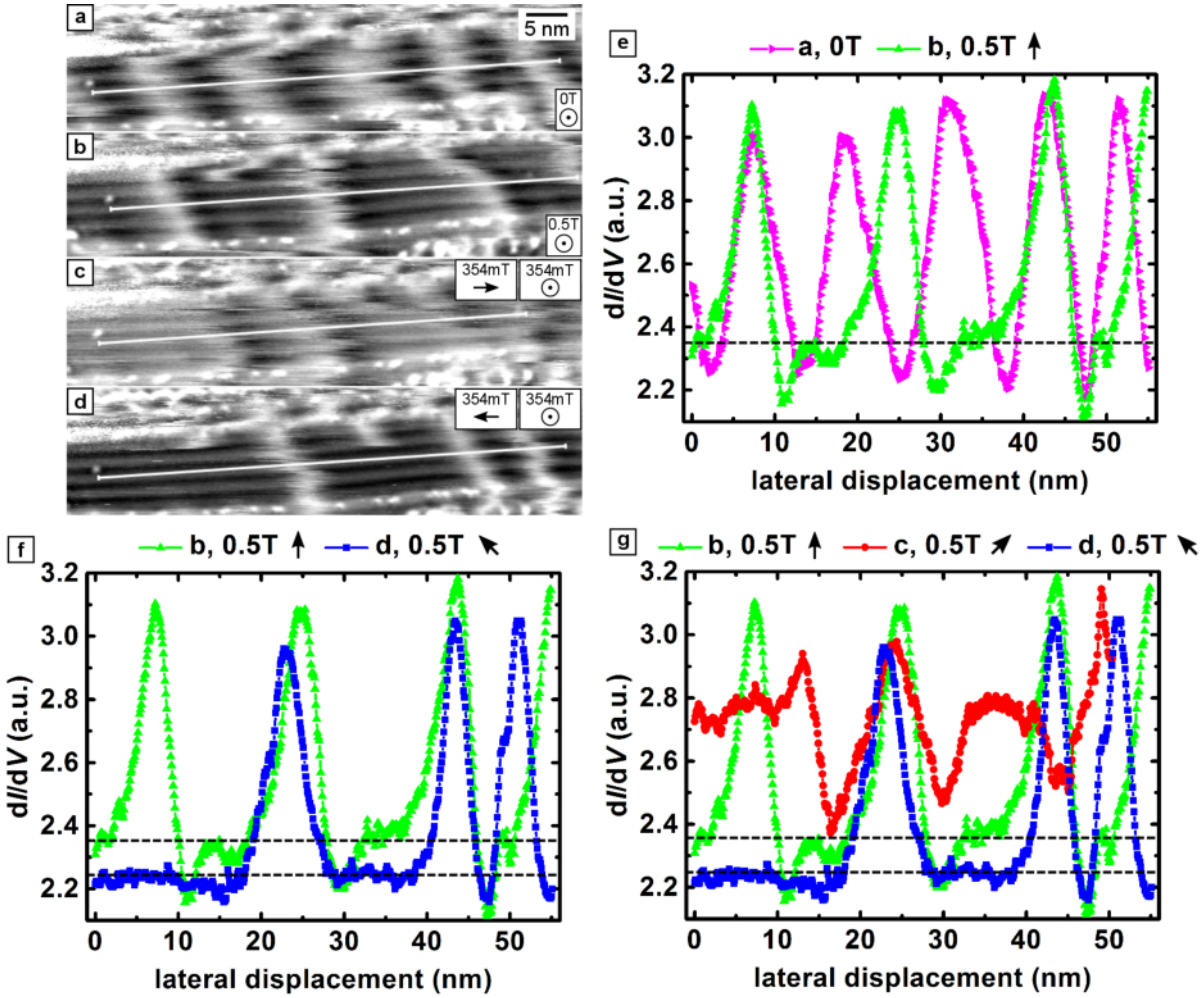

Figure 6.4: (a-d) dI/dV maps of the Fe-TL area 2 of figure 5.6 in (a) zero field, (b) an out-of-plane field of 0.5 T, (c) and (d) a field canted by 45° from the surface normal in both directions towards the double lines and a magnitude of 0.5 T. (e-g) show the line profiles of (a-d) for positions marked by white lines. The dotted horizontal lines indicate the dI/dV signal level at the boundary of the 360° domain walls for each applied external field. (Measurement parameters: V = -0.7 V, I = 1 nA, T = 4.7 K)

Appendix D

Figure 6.5 shows the Fe-DL exhibiting three reconstructed areas joining in a common center in fields as marked. These areas were recorded in the same experiment as the skyrmion in section 5.2.3. I cannot use the hollow site dislocation line in the center of the reconstructed areas as in Appendix A due to the distortion of the magnetic structure in one of the reconstructed areas marked by a blue dotted rectangle. Unlike the other parts of the reconstructed area, the neighboring bcc-like areas here are not in phase and thus the dI/dV signal at the hollow site dislocation line is distorted. Therefore, I used the tilted spin spirals in the bcc-like areas. The comparison of their amplitudes does not indicate a tip change. However, this method has a large uncertainty in the propagation direction of the spin spirals compared to the method used in Appendix A. Both maps reveal that the tip's magnetization is oriented about 60° from the surface normal and has an in-plane angle as marked in figure 6.5.

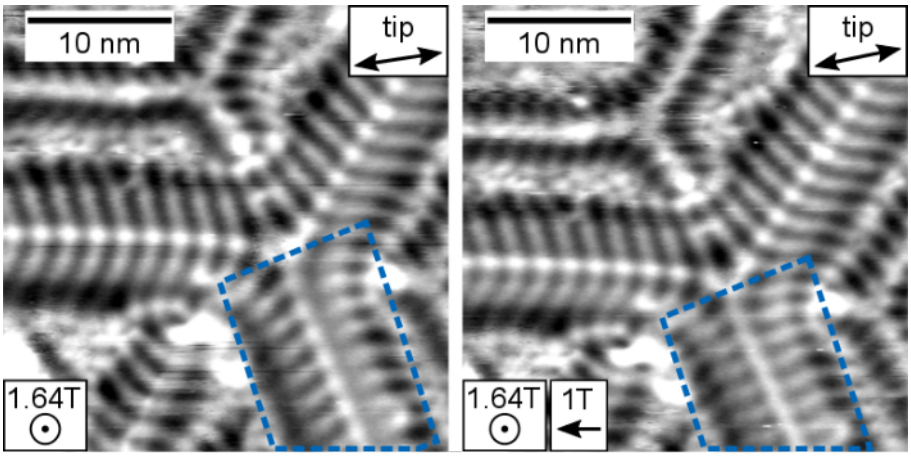

Figure 6.5: Differential tunneling conductance maps of reconstructed areas in the Fe-DL on Ir(111) are shown in fields as marked. The in-plane orientation of the tip's magnetic moment is marked for both field orientations according to the spin spiral amplitudes. (Measurement parameters: T = 4.7 K, V = -0.7 V, I = 1 nA)

Appendix E

I prepared a sample similar as in section 5.4 but with a faked Pd deposition. At first, I deposited about two ML of Fe on the clean Ir(111) crystal while the sample's temperature was increased from about 160 °C to 210 °C. After the sample cooled down to room temperature I faked a Pd evaporation by using the corresponding MBE device with the usual parameters leading to evaporation of Pd. This time I closed the shutter in front of the device making it impossible for the Pd to reach the sample. The result can be seen in figures 6.6 b and c. The sample with the faked Pd evaporation proves that the observed 0.5 nm-periodic superstructure on the Fe-DL does not involve Pd. However, the surface

coverage does increase with the Pd deposition time which indicates that the superstructure forms due to atoms or molecules emitted from the heated Pd rod. As Pd is known to store large amounts of hydrogen the result of the faked Pd evaporation suggests that the 0.5 nm-periodic superstructure is a hydrogenated Fe-DL. This was later confirmed by my coworker Dr. Hsu via atomic hydrogen deposition on the pristine Fe-DL.

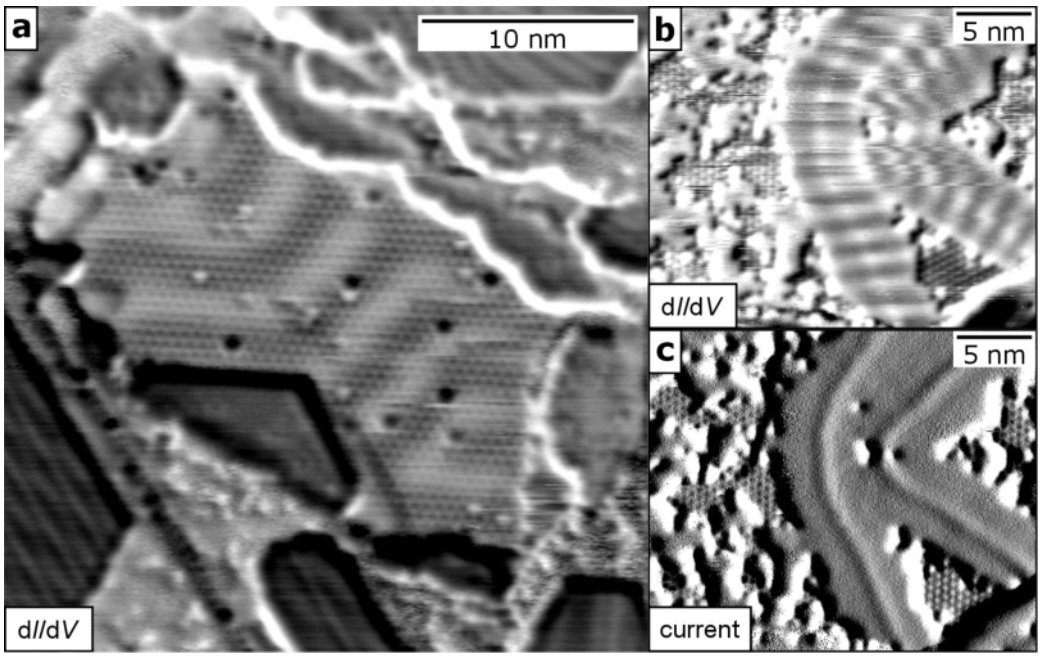

Figure 6.6: (a) shows a dI/dV map of Fe/Ir(111) after deposition of less than half a ML of Pd. A 0.5 nm-periodic superstructure can be observed on the Fe-DL in zero magnetic field as already shown in figure 5.19. (b) dI/dV and (c) current maps of a similar sample with a faked Pd deposition exhibit the same 0.5 nm-periodic superstructure on the strained Fe-DL. (Measurement parameters: T = 4.7 K, V = -0.7 V, I = 1 nA)

Acknowledgments

This doctoral thesis would not have been possible without the help of many colleagues and friends. Therefore, I'm most grateful to:

- Prof. Dr. Roland Wiesendanger for giving me the opportunity to work in one of the world-leading groups in nanomagnetism and scanning probe microscopy, the possibility to present my research results at international conferences as well as for the supervision of this thesis,
- Dr. Kirsten von Bergmann and Dr. André Kubetzka for their constructive criticism and many helpful discussions,
- Dr. Thomas Eelbo for introducing me to the vector-field STM in lab004 of building 9a and Dr. Pin-Jui Hsu for the brief but fruitful cooperation in lab004,
- the whole lab013 team for the great atmosphere, the helpful discussions, and the help in the lab,
- the GrK 1286 for funding and Prof. Dr. Ulrich Merkt and Dr. Katrin Buth for the support and supervision concerning the Graduiertenkolleg,
- Andrea Beese, Ute Brenger, Sigrid Schmidtke, Norbert Dix, Michael Langer and Heiko Fuchs for their administrative and technical support,
- Jörg Völkel and Dieter Klatt for the reliable supply with liquid helium and the whole crew of the mechanical and electronic workshops for quick and uncomplicated fixes,
- everyone in the group of Prof. Wiesendanger for the friendly and welcoming atmosphere as well as the occasional help and hints,
- my dear Joanna Szczepanowska for proofreading and her moral support,
- my parents, Irmgard Metz-Schmidt and Günter Schmidt, as well as my brother Moritz Schmidt for all their support throughout my life,
- all friends who accompanied me in my studies.

Eidesstattliche Versicherung
Declaration on oath

Ich erkläre hiermit, dass ich die vorliegende Arbeit selbständig verfasst und keine anderen als die angegebenen Quellen und Hilfsmittel verwendet habe.
I hereby declare, on oath, that I have written the present dissertation by my own and have not used other than the acknowledged resources and aids.

Ort, Datum	Unterschrift
Place, Date	Signature